DEVELOPMENT OF BIOSENSOR AND ELECTROCHEMICAL STUDIES OF CARBON-BASED MATERIALS

CHONG KWOK FENG

NATIONAL UNIVERSITY OF SINGAPORE
2009

DEVELOPMENT OF BIOSENSOR AND ELECTROCHEMICAL STUDIES OF CARBON-BASED MATERIALS

CHONG KWOK FENG

(B.Sc. Universiti Teknologi Malaysia)

A THESIS SUBMITTED

FOR THE DEGREE OF DOCTOR OF PHILOSOPHY

DEPARTMENT OF CHEMISTRY

NATIONAL UNIVERSITY OF SINGAPORE

2009

Acknowledgements

First, I would like to take this opportunity to thank my supervisor Associate Professor Loh Kian Ping for his encouragement, guidance and support as well as understanding for my weaknesses during the course of my graduate studies. I have benefited and learnt a lot from his kind and modest nature, his passion in pursuing science, and his attitude toward career and life.

I would like to express my gratitude to my co-supervisor Associate Professor Sheu Fwu-Shan for his guidance and cooperation for the biological experiments in my thesis.

I would like to extend my gratitude to Associate Professor Ting Yen Peng and his group for the support in microalgae experiment; Associate Professor Lim Chwee Teck and Dr. Vedula for the support and assistance in AFM studies. My gratefulness also goes to Dr. Chen Wei for useful discussion and cooperation on graphene studies.

I would also like to thank my coworkers in Lab under LT23: Dr Wang Junzhong, Dr Wang Shuai, Dr Bao Qiaoliang, Mr Zhong Yu Lin, Ms Hoh Hui Ying, Mr. Lu Jiong, Mr. Anupam Midya, Ms Deng Su Zi, Ms Ng Zhao Yue, Ms Priscilla Ang Kailian and many more. Without their daily help and support, this thesis would not be possible.

Last but not least, I would express my deepest gratitude to my parents for the support throughout these years.

My sincere appreciation is dedicated to those who are involved directly or indirectly in the completion of this thesis.

Publications

1. Whole Cell Environmental Biosensor on Diamond Platform

   Chong, K. F.; Loh, K. P.; Ang, K.; Ting, Y. P. *Analysts*, 2008, 133(6), 739-743.

2. Cell Adhesion Properties on Photochemically Functionalized Diamond

   Chong, K. F.; Loh, K. P.; Vedula, S. R. K.; Lim, C. T.; Sternschulte, H.; Steinmüller, D.; Sheu, F-S.; Zhong, Y. L. *Langmuir*, 23(10), 5615-21.

3. Optimizing Biosensing Properties on Undecylenic Acid-Functionalized Diamond

   Zhong, Y. L.; **Chong, K. F.**; May, P. W.; Chen, Z-K.; Loh, K. P. *Langmuir*, 23(10), 5824-30.

Summary

This thesis consists of three sections of research results. The first results section of the thesis (Chapter 3) outlines the surface functionalization of microcrystalline diamond and ultrananocrystalline diamond surfaces. The biocompatibility of diamond was investigated with a view towards correlating surface chemistry and topography with cellular adhesion and growth. An atomic force microscope in force mode was used to measure the adhesion force of normal human dermal fibroblast (NHDF) cells on microcrystalline and ultrananocrystalline diamond with different surface chemistry. A direct correlation between initial cell adhesion forces and the subsequent cell growth was observed. Surface carboxylic acid groups on the functionalized diamond provide tethering sites for protein to support neuron cells growth, and a surface gradient of polyethylene glycol was assembled on a diamond surface for the construction of a cell gradient. This section is motivated by a desire to discover the biocompatibility of diamond in terms of its surface chemistry and topography as well as the construction of a surface concentration gradient on diamond to support neuron cells growth for combinatorial chemistry studies.

In the second results section of this thesis (Chapter 4 and Chapter 5), whole cell biosensors were constructed on a diamond electrode for the heavy-metal ion sensing. Different biological entities were used, namely *Chlorella vulgaris* and *Acidithiobacillus ferrooxidans*. Detection linearity, sensitivity and long-term stability for the diamond-based biosensor were studied in this section. The ability of diamond to resist biofouling is the focus in this section. This section is motivated by a desire to incorporate the extraordinary electrochemical properties of diamond for the construction of a robust and sensitive biosensor.

In the third results section of this thesis (Chapter 6), standard electrochemical properties for epitaxial graphene were studied. Two types of graphene samples were electrochemically studied: namely as-synthesized graphene and mild-oxidized graphene. Different redox species were used to elucidate the background current, heterogeneous electron-transfer rate constant, charge-transfer resistance and activation enthalpy for the graphene sample. An extremely low background current for graphene is the focus in this section. This section is motivated by the desire to investigate the electrochemical properties of novel material graphene.

List of Figures

List of Tables

Chapter 1. Introduction

In 1965, Intel co-founder Gordon Moore predicted that the number of transistors on a chip will double about every two years[1]. This prediction is better known as Moore's law. For decades this law has been widely used in the semiconductor industry to guide long-term planning and to set targets for research and development[2]. Almost every measure of the capabilities of digital electronic devices is strongly linked to Moore's law: processing speed, memory capacity, sensors and even the number and size of pixels in digital cameras[3]. The popular perception of Moore's law is that computer chips are compounding in their complexity at near constant per unit cost, which relates to the compounding of transistor density in two dimensions. As more transistors can be put on a chip, the cost of making each transistor is decreased[4]. Moore's law drives chips, communications and computers in the scientific discovery and development. Over time, bioinformatics and computer modeling have attracted more attention than experiment trial and error. On 13 April 2005, Gordon Moore stated in an interview that the law cannot be sustained indefinitely and he also noted that transistors would eventually reach the limits of miniaturization at atomic levels:

"In terms of transistor size you can see that we're approaching the size of atoms which is a fundamental barrier, but it'll be two or three generation before we get that far-but that's as far out as we've ever been able to see. We have another 10 to 20 years before we reach a fundamental limit. By then they'll be able to make bigger chips and have transistor budgets in the billions."[5]

This shows that continuous scaling of the chip dimensions has faced its bottleneck. According to the Moore's law projection, a device physical gate length will be in the region of 10 nm in year 2015. Scaling devices to these dimensions is very difficult as the metal-oxide-semiconductor field effect transistor (MOSFET) technology is approaching its physical limits at these dimensions. Moreover, the chips are getting very hot due to the increasing transistor density in a computer chip[6].

"Within 10 years, the entire semiconductor industry will rely on nanotechnology," said Dr. M. Roco from US National Nanotechnology Initiative in 2003. He is one of the many who predicted Moore's law will be preserved by nanotechnology and nanomaterials. Dimensional nanomaterials present fundamentally different physical concepts to conventional bulk materials because of their unique density-of-states as well as vibrational and electronic confinement. This implies that nanomaterials may exhibit some interesting properties which are not known to the bulk materials.

This thesis is motivated by the desire to study two carbon-based nanomaterials, namely diamond and graphene. Basically, this thesis can be divided into three parts according to the nature and direction of the research. The first part of the thesis will outline the biocompatibility studies of diamond with different surface chemistry and topography. Microcrystalline and ultrananocrystalline diamond surfaces will be characterized by using chemistry characterization methods, and their biology properties will be studied by using atomic force microscopy in force mode and some biology characterization techniques. A sound understanding of the surface-biocompatibility relationship allows scientists to further develop whole-cell biosensors based on a diamond platform. The surface-functionalized diamond is further developed to construct a surface functional group gradient, and a cell gradient is successfully achieved on a diamond surface. This opens up the potential for diamond to be an experimental platform for combinatorial discovery and analysis.

The second part of the thesis will discuss the construction of a whole-cell biosensor based on a diamond platform by using two different biological entities, namely a unicellular microalgae (*Chlorella vulgaris*) and a bacteria cell (*Acidithiobacillus ferrooxidans*). These two diamond-based biosensors are constructed for heavy metal detection. The biosensor sensitivity and long-term stability will be discussed and correlated with the unique properties of the diamond surface.

The third part of the thesis will discuss another carbon-based nanomaterial, graphene. The novel electrochemical properties of epitaxial graphene before and after surface treatment will be discussed. Low background current and charge-transfer resistance enable graphene to be an excellent candidate for biosensing purposes. The biofouling problem of nicotinamide adenine dinucleotide (NADH) is solved by surface treatment of graphene, and a low detection limit (10 nM) can be achieved on a graphene electrode. The electrochemical and kinetic data can serve as a benchmark for evaluating the electrochemical properties of graphene.

1.1 Diamond

1.1.1 Diamond General Properties

Diamond is an allotrope of carbon where the carbon atoms are arranged in the face-centered cubic crystal structure called a diamond lattice. It is known as the second most stable form of carbon after graphite, and the conversion rate from diamond to graphite is negligible at ambient conditions. Unlike carbon in its sp^2 hybridization, the diamond structural network is formed by sp^3-hybridized carbon atoms, each covalently bonded to three neighboring carbon atoms in a tetrahedral coordination. The diamond lattice possesses a lattice constant of *a* = 3.567 Å, while the distance between nearest neighbors is 1.545 Å[7]. The basis of this structure can be regarded as two carbon atoms commonly placed at positions [0, 0, 0] and [¼, ¼, ¼] of the cubic unit cell, as shown in Figure 1.1.

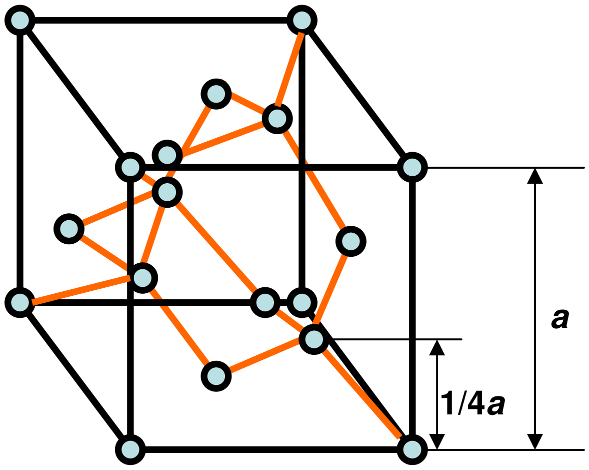

Figure 1.1 Schematic diagram of diamond unit cell.

The covalent bonding and inflexibility of the three-dimensional diamond lattice enables diamond to possess extraordinary hardness with bulk modulus of 4.4×10^{11} N/m^2, which is about four times larger than that of Si (0.98×10^{11} N/m^2)[8]. It is well known as the hardest natural material according to Mohs scale of mineral hardness[9]. It also has high thermal conductivity of 15×10^3 W/m^{-1} K^{-1} at 80 K[10] and high optical dispersion[11]. Due to its highly stable structure, diamond can only be transformed into graphite at temperatures above 1700°C in vacuum or oxygen-free atmosphere; in air, transformation starts at ~ 700°C[12]. As all four valence electrons in a carbon atom contribute to the covalent bonding, the diamond valence band is separated from the unoccupied conduction band by 5.47 eV, hence making it a wide band gap semiconductor[13, 14]. However, diamond electrical properties can be tuned by controlling p-type and n-type electrical conduction. In order to increase the electrical conductivity, diamond can be doped with boron at certain concentrations during the growing process to transform it into a p-type semiconductor. Boron atoms substitutionally insert for some of the carbon atoms into the growing diamond lattice. These boron atoms function as electron acceptors and contribute to the formation of free-charge carriers (i.e. holes or electron vacancies)[15]. Like boron doping, nitrogen doping increases diamond conductivity by turning it into an n-type semiconductor. Here, the nitrogen atoms function as electron donors and the free-charge carriers are free electrons. Band diagrams for p-type and n-type semiconductor diamond are illustrated in Figure 1.2.

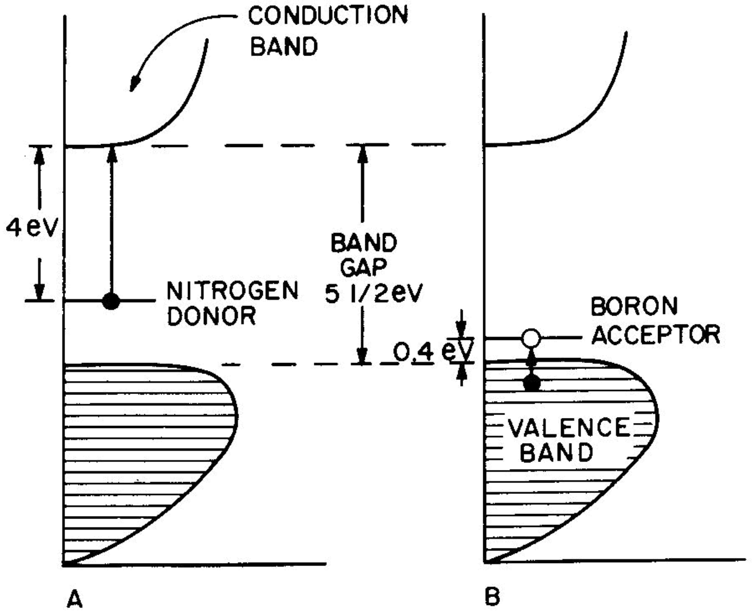

Figure 1.2 Band diagram for (A) n-type diamond and (B) p-type diamond[16].

Due to the issue of high cost, natural diamond is seldom used in the research area. Instead, synthetic diamond is widely used for its low cost and reproducible properties. There are several methods used to produce synthetic diamond. The original method uses high pressure and high temperature (HPHT) with pressures of 5 GPa and temperature of 1500°C[17]. HPHT is generally used in industrial applications. The second method is chemical vapor deposition (CVD), in which a dilute hydrocarbon-in-hydrogen plasma is excited over a substrate to produce energetic carbon and hydrogen radicals which react on a substrate to form diamond. CVD is widely used in laboratory research owing to its flexibility and simplicity. The advantages of CVD diamond as compared to HPHT diamond include the ability to grow diamond over large areas and on various substrates. Fine control over the chemical impurities allow the doping of the diamond and control of its electronic properties.[18] The CVD growth of diamond starts with the substrate preparation whereby an appropriate material with suitable crystallographic orientation is chosen and diamond powder is used to abrade the non-diamond substrate in order to increase the nucleation process. The chosen process gas mixture is introduced into the chamber after loading the substrate. The gases always include a hydrocarbon source, typically methane, and hydrogen with a typical ratio of 1:99. Hydrogen is essential because it selectively etches off non-diamond carbon. Dopant gases such as diborane or trimethylboron can also be introduced. The gases are dissociated into chemically active radicals in the growth chamber using microwave power, a hot filament, an arc discharge, a welding torch, a laser, an electron beam or other means[19].

1.1.2 Nanocrystalline and Ultrananocrystalline Diamond

Depending on growth parameters such as gas mixture, temperature and substrate seeding, CVD growth can produce different kinds of diamond films. They can be classified according to the crystal grain size as: microcrystalline (grain size about 1 μm), nanocrystalline (grain size about 100 nm), and ultrananocrystalline (grain size below 10 nm) diamond films. The diamond film morphology depends on the reactant gases, their mixing ratios and the substrate temperature. With low partial pressure methane, highly crystalline diamond films are obtained. With increasing methane concentration, the crystalline morphology disappears and an amorphous structure consisting of disordered graphite containing small clusters of diamond nanocrystals will emerge. By controlling these two extremes during CVD growth, high quality nanocrystalline and ultrananocrystalline diamond films can be obtained[20]. It should be noted that highly doped n-type conductive ultrananocrystalline diamond with conductivity as high as 250 Ω^{-1} cm^{-1} can be made *via* the addition of nitrogen gas during microwave plasma CVD[21]. The numerous grain boundaries and crystal defects in microcrystalline diamond reduce electron and hole mobilities and degrade the electronic performance of diamond. Nanocrystalline diamond has been shown to function as excellent electrodes for electrochemical applications, due to its large electrochemical potential window and low background current.[22,23] Coupled with its inherent biocompatibility, both nanocrystalline and ultrananocrystalline diamond films are excellent active electrodes for biosensor development[24].

1.1.3 Electrochemical Properties of Diamond

Boron-doped microcrystalline, nanocrystalline and ultrananocrystalline diamond films possess a number of excellent electrochemical properties, unequivocally distinguishing them from other commonly used sp^2-bonded carbon electrodes, such as glassy carbon, pyrolytic graphite, and carbon paste[25]. These properties are (i) low and stable background current, resulting in higher signal-to-noise ratio; (ii) wide electrochemical potential window in aqueous and non-aqueous media, which affords the detection of a wide range of redox species, and most importantly the detection of high overpotential redox species; (iii) superb microstructural and morphological stability at high temperature and current densities (0.1 – 10 A/cm^2, 85% H_3PO_4), resulting in operation under harsh conditions; (iv) good responsiveness to several aqueous and non-aqueous redox species without any pretreatment, resulting in direct electrochemical detection and eliminating mediated reagents; (v) long term response stability; (vi) weak adsorption of polar molecules, resulting in improved resistance to electrode deactivation and fouling; (vii) optical transparency in the UV/Vis and IR regions of the electromagnetic spectrum, useful properties for spectroelectrochemical measurements[26].

There are several factors affecting the electrochemical response of diamond electrodes, including surface cleanliness, doping level, presence of non-diamond sp^2 carbon impurities and the type of surface termination. Surface cleanliness greatly influence the response as adsorbed contaminants can either block specific surface sites, thus inhibiting surface-sensitive redox reactions, or increase the electron-tunneling distance for redox species, thereby lowering the probability of tunneling and decreasing the rate of electron transfer. The hydrogen-terminated diamond surface is not as susceptible to contamination as other electrodes are, because of its hydrophobic surface and the absence of π electrons. A hydrogen-terminated diamond surface can be effectively cleaned with chemical treatment in (i) 3:1 HNO_3/HCl (v/v) and (ii) 30% H_2O_2/H_2O (v/v) to oxidize the contaminants and non-diamond sp^2 carbon impurities. The surface is then rehydrogenated in a hydrogen microwave plasma[27]. In order to have sufficient electrical conductivity for electrochemical measurements (< 0.1 Ω cm$^-$

^{1}), the dopant concentration within diamond films must be maintained at 1×10^{19} cm^{-3} or greater.

1.1.4 Surface Functionalization of Diamond Surface

Diamond surface functionalization can be done by several routes. Generally, it can be categorized as functionalization of hydrogen-terminated diamond and oxygen terminated-diamond. For hydrogen-terminated diamond, surface functionalization can be achieved by diazonium salt reduction, photochemical reaction with functional alkenes and direct reaction with radical species in gas phase. For oxygen-terminated diamond, surface functionalization can be achieved by silanization and esterification. Diazonium salt reduction and photochemical functionalization will be further discussed as these two methods are widely used in the development of biosensor and molecular electronics on diamond.

1.1.4.1 Diazonium Functionalization on Hydrogen-terminated Diamond Surface

Electrochemical reduction of diazonium salts is a common and simple method for surface functionalization of carbon-based materials[28,29]. For diamond, a strong C-C bond is formed between diamond and a phenyl molecule thru the attack of a phenyl radical generated during an electrochemical reduction process, as illustrated in Figure 1.3.

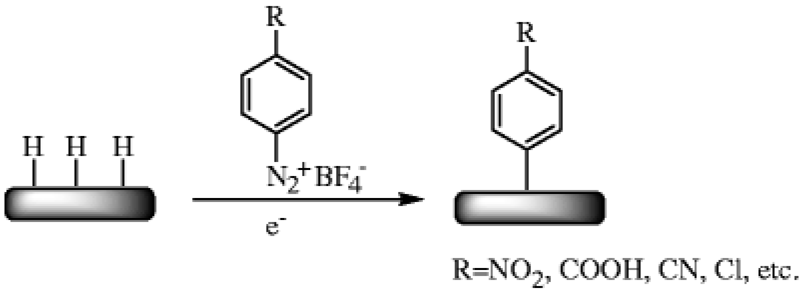

Figure 1.3 Electrochemical reduction of aryl diazonium salts on a diamond surface[30].

However, both electrochemical reduction and spontaneous binding suffer some drawbacks such as multilayer formation rather than monolayers, and that conductive diamond must be used in order for the electrochemical reduction. This can be attributed to the continuous attack of the electrochemically generated phenyl radical to the grafted aryl group (Figure 1.4).

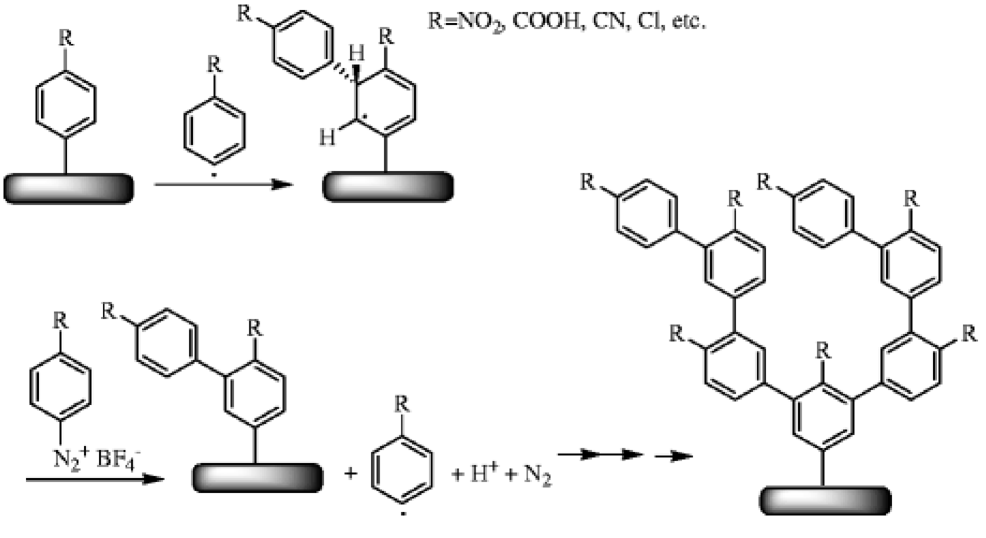

Figure 1.4 Multilayer formation by electrochemical reduction of diazonium salt[31].

Other than electrochemical reduction, covalent bonds between diamond and diazonium salts can also be formed in the presence of 1 % sodium dodecyl sulfate

(SDS). This performs a spontaneous binding in the absence of external bias.[32] A very stable, homogeneous and dense monolayer of 4’-nitro-1,1-biphenyl has been achieved on ultrananocrystalline diamond by using saturated diazonium salt[33]. The reduction of the diazonium salt arises from spontaneous charge transfer from diamond, facilitated by the negative electron affinity of the latter.[34] This spontaneous coupling method is attractive as it does not require electrochemical equipment or doped diamond films.

The principal interest in diazonium-coupled diamond modification is that the diamond-tethered functional groups can be used for the covalent linking of biomolecules, making it a promising platform for biosensing. The most intensively studied diazonium salt derivative is the nitrophenyl salt in which the nitro groups can be electrochemically reduced[35] to primary amines for the linkage of DNA[36] or other biomolecules such as gluocose oxidase[37]. Recently, Zhong *et. al.* demonstrated the Suzuki coupling of aryl molecules onto the aryldiazonium-salt- functionalized diamond surface. This opens up the possibilities for the application of diamond in molecular electronics, as uninterrupted large molecular conjugation can be achieved on diamond (Figure 1.5).

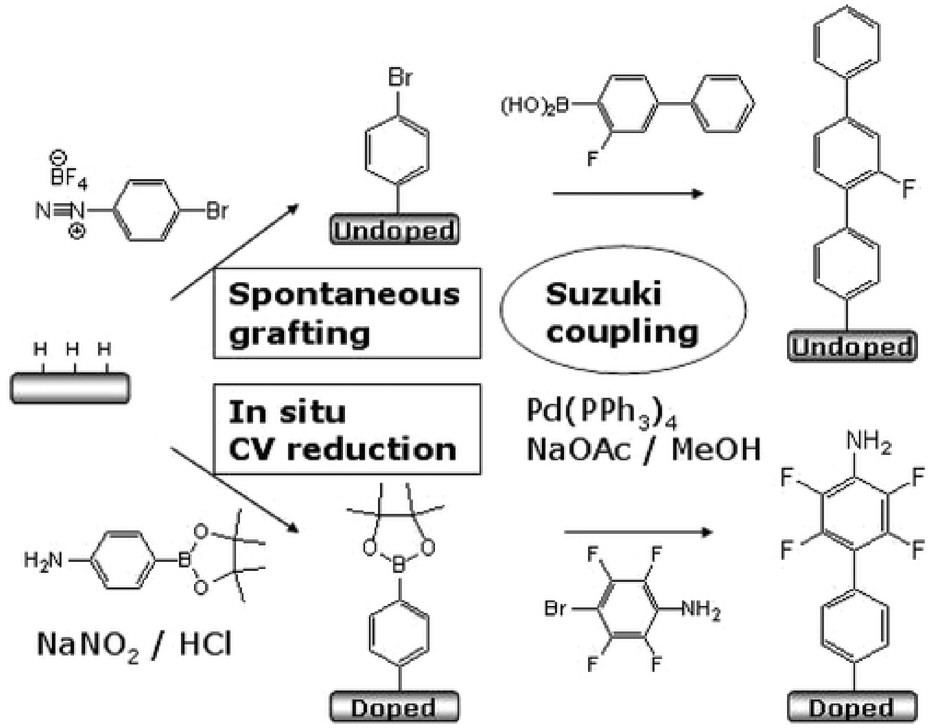

Figure 1.5 Diamond functionalization by aryldiazonium salts, followed by Suzuki Coupling with aryl organics[38].

1.1.4.2 Photochemical Functionalization on Hydrogen-terminated Diamond Surface

When illuminated with 254 nm UV light, hydrogen-terminated diamond will emit electrons from the valence band directly into vacuum.[39] Based on this principle, UV irradiation of hydrogen-terminated diamond covered with liquid films of an appropriate alkene (e.g. 12-amino-dec-1-ene protected woth a trifluoroacetic acid group, perfluorodecene, trifluoroethyl ester of ω-undecenoic acid, etc.) provides a facile approach for the functionalization on diamond. This scheme was first proposed by Hamers *et. al.*[40] and is now intensively used by different groups for diamond surface functionalization. The photochemical functionalization is initiated by photoejected electrons produced either (i) by excitation of surface states lying just below the Fermi energy up to the conduction band followed by ejection of an electron into liquid phase, or (ii) by direct ejection of electrons from the valence band to liquid phase via internal photoemission (Figure 1.6). The photoejected electrons will form liquid-phase radical anions, which can react directly with a hydrogen-terminated diamond surface by abstracting hydrogen atoms from the surface, thereby creating reactive surface sites with positive holes for reaction with alkene functionality to form strong covalent bonds. While the photochemical functionalization allows the introduction of several functional groups on a diamond surface, the reaction time required is rather long (more than 10 h) and most organic molecules absorb at the used UV wavelength.

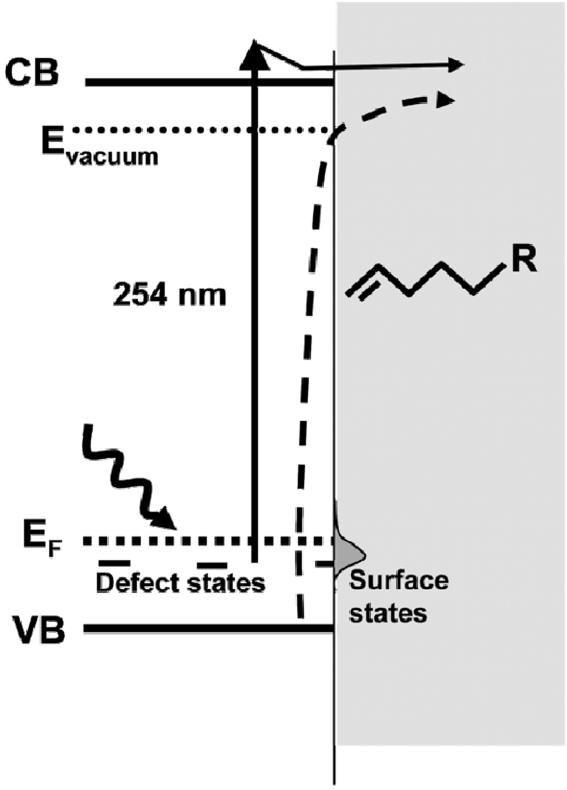

Figure 1.6 Proposed mechanism for photoejection of electrons into liquid phase: excitation from occupied defects and/or surface states to the conduction band followed by diffusion and emission (solid arrow); direct photoemission from valence band to the vacuum level (dashed arrow)[41].

1.2 Biosensor

Various terminologies are used to define biosensors depending on the field of the application. A common cited definition is: “a biosensor is a chemical sensing device in which a biologically derived recognition entity is coupled to a transducer, to allow the quantitative development of some complex biochemical parameter”, and also: “a biosensor is an analytical device incorporating a deliberate and intimate combination of a specific biological element (that creates a recognition event) and a physical element (that transduces the recognition event)”[42]. As demonstrated in Figure 1.7, a biosensor consists of a bioelement and a transducer (sensor element). The bioelement may be an enzyme, antibody, nucleic acid, living cells, tissues, etc. and possesses a biological recognition system. The transducer part of the biosensor serves to transfer the signal from the output domain of the biological recognition system to the (normally electrical) signal. Some of the examples of bioelements and transducers in biosensors are shown in Figure 1.8. Different combination of these two elements will construct biosensors working on different sensing mechanisms.

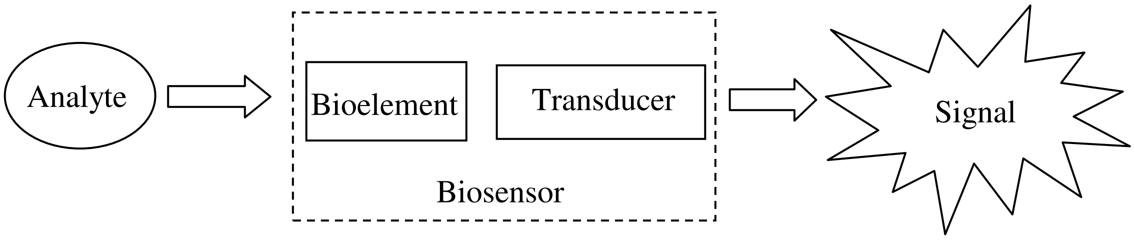

Figure 1.7 Schematic representation of a biosensor.

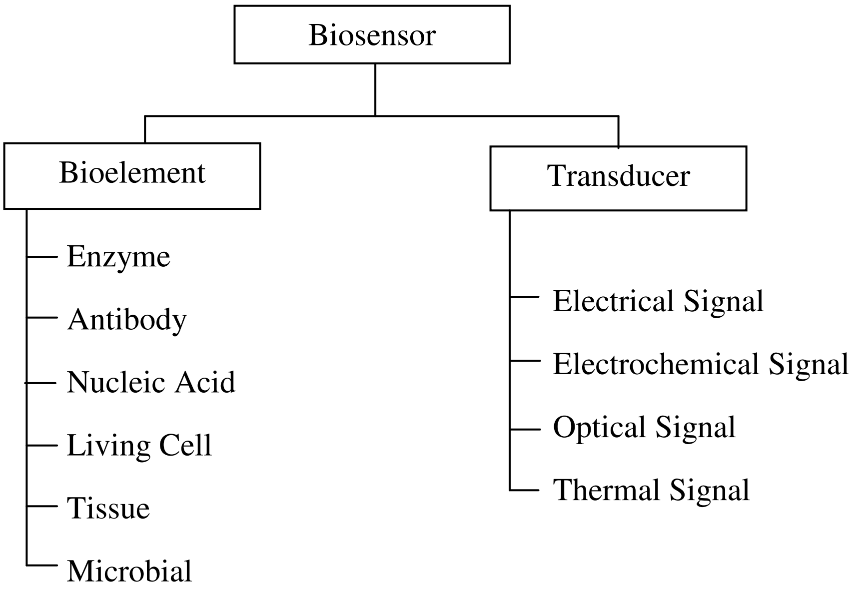

Figure 1.8 Examples of elements in biosensors.

The initial stage for biosensor construction involves the immobilization of bioelement or biological receptors to the transducer. The first biosensor immobilization was done by Clark *et. al.* in 1962 for the enzyme-based biosensor for glucose in which glucose oxidase was entrapped between two membranes[43]. Since then, various immobilization methods have been developed for biosensor construction, such as membrane entrapment[44], polymeric matrix entrapment[45], bilayer lipid membrane entrapment[46], covalent linkage of bioreceptors[47], bulk modification of entire electrode[48], etc. Regardless of what immobilization method is used, the bioreceptor must remain active after the immobilization process.

1.2.1 Electrochemical Biosensors

An electrochemical biosensor is a biosensor with an electrochemical transducer, which is an electronic conducting or semiconducting electrode. The underlying principle for an electrochemical biosensor is that many chemical reactions produce or consume ions or electrons which, in turn, cause some change in the electrical properties of the solution which can be sensed and used as measuring parameters. Electrochemical biosensors can be classified into three main categories based on the measured electrical parameters: conductometric, amperometric and potentiometric.

An conductometric-based electrochemical biosensor measures the electrical conductance/resistance of the solution. When electrochemical reactions produce ions or electrons, the overall conductivity or resistivity of the solution changes and these are monitored by the conductometric biosensor[49]. Generally, conductance measurements have relatively low sensitivity. Amperometric based biosensors measure the current resulting from the electrochemical oxidation or reduction of an electroactive species. It is done by applying a constant potential at the working electrode and the resulting current is directly correlated to the bulk concentration of the electroactive species. Potentiometric based electrochemical biosensors measure the potential difference between two electrodes which are separated by a permeable and selective membrane to prevent current flowing between them.

Over the years, different novel materials have been used for the construction of electrochemical biosensors, such as gold nanoparticles[50], boron-doped diamond[51], and carbon nanotubes[52]. These materials open up the field to incorporate advanced nanomaterials with biological entities in the construction of biosensors. Research in this field is mainly focusing on the development of novel sensing strategies and the improvement of specificity, sensitivity and response time.

1.2.2 Diamond as a Biosensor

Though diamond is proven to possess excellent electrochemical properties, the realization of diamond biosensora is hindered by its chemically inert surface. The first breakthrough came in 2002 when two research groups published two important reports in the development of diamond biosensors. Hamers' group[53] demonstrated that an amine-terminated hydrocarbon chain could be covalently attached to the surface of nanocrystalline diamond by using a photochemical process. A highly stable DNA biosensor was constructed on a diamond platform by covalent bonding between DNA and the hydrocarbon chain. The hydrocarbon chain on diamond exhibited extraordinary stability as compared to silicon and gold surfaces, owing to the strong covalent C-C bond. The second paper published in the same year by Garrido *et. al.*[51] reported the construction of an enzyme biosensor on a diamond platform. The same immobilization chemistry as Hamers' group was used to attach an enzyme to the diamond surface. It should be noted that the enzyme retained its functionality and diamond was able to electrochemically detect the redox reactions of immobilized catalase enzymes. Since then this immobilization chemistry is being extensively applied in developing diamond biosensors.

1.3 Biocompatibility

The word biocompatibility has drawn numerous discussions about its definition since the word was first mentioned by Homsy *et. al.* in 1970[54]. Until now, there are four definitions for biocompatibility. According to the American Society for Testing and Materials (ASTM), biocompatibility is the comparison of the tissue response produced through the close association of the implanted candidate material to its implant site within the host animal to that tissue response recognized and established as suitable with control materials. A more precise version for the definition of biocompatibility is introduced by Willams as the ability of a biomaterial to perform its desired function with respect to a medical therapy, without eliciting any undesirable local or systemic effects in the recipient or beneficiary of that therapy, but generating the most appropriate beneficial cellular or tissue response in that specific situation, and optimizing the clinically relevant performance of that therapy[55].

1.3.1 Biocompatibility of Diamond

Diamond has been claimed to be a biocompatible material and its biocompatibility is subjected to extensive studies both *in vitro* and *in vivo*. Due to a combination of superior properties such as hardness[56], fracture toughness[57], low friction coefficient[58], high chemical resistance[59] and a variety of possible coating substrates[60], diamond hold promise in applications in the biomedical field. The protein adsorption, cell adhesion and implantation results were first systematically studied by Tang *et. al.*[61] and results show that diamond is as biocompatible as titanium and stainless steel, which are used frequently in implantable devices. Nordslettern *et. al.*[62] showed that diamond particles are inert in serum-free monocyte culture and that the cell morphology did not change after the ingestion of diamond. Nanocrystalline diamond has also been evaluated as a coating on implant surfaces to improve the durability of orthopaedic prostheses. One reason for the choice of nanocrystalline diamond is related to its nanocrystalline morphology which mimics bone surface roughness. Results showed that improved human osteoblast proliferation and the stimulation of differentiated markers can be obtained on a nanocrystalline diamond surface, which is useful for bone regeneration purposes[63].

References

---

[1] Moore, G. *IEDM Tech. Digest* **1975**, 11.

[2] Cornelius, D.; Barend, v. *Getting new technologies together*, New York: Walter de Gruyter **1998**, 206.

[3] Myhrvold, N. *Moore's law Corollary: Pixel Power*, New York Times, **2006**.

[4] Moore, G. *Electronics Magazine* **1965**, 4.

[5] Dubash, M. *Moore's Law is dead, says Gordon Moore*, Techworld. **2006.**

[6] http://www.kurzweilai.net/meme/frame.html?main=/articles/art0618.html

[7] Kaiser, W.; Bond, W. L. *Phys. Rev.* **1959**, 115, 857.

[8] Field, J. E. *Science of Hard Materials*, England, Adam Hilger Ltd **1986**, 181.

[9] *Moha Scale of Mineral Hardness*, American Federation of Mineralogical Societies.

[10] Wei, L. *Phys. Rev.* **1993**, 70, 3674.

[11] Walker J. *Reports on Progress in Physcis* **1979**, 43, 1605.

[12] John, P. *Diamond and Related Materials* **2002**, 11, 861.

[13] van der Weide, J.; Zhang, Z.; Baumann, P. K.; Wensel, M. G.; Berholc, J.; Nemanich, R. J. *Phys. Rev. B* **1994**, 50, 5803.

[14] Roberts, R. A.; Walker, W. C. *Phys. Rev.* **1967**, 161, 730.

[15] Mamin, R. F.; Inushima, T. *Phys. Rev. B* **2001**, 63, 033201.

[16] http://www.minsocam.org/MSA/collectors_corner/arc/color.htm.

[17] *HPHT Synthesis*, International Diamond Laboratories.

[18] Koizumi, S; Nebel, C. E.; Nesladek, M. *Physics and Applications of CVD Diamond*, Wiley VCH, **2008,** 50.

[19] Celii, F. G.; Butler, J. E. *Ann. Rev. Phys. Chem.* **1991**, 42, 643.

[20] Raty, J.; Galli, G. *Nat. Mater.* **2003**, 2, 792.

[21] Bhattacharyya, S.; Auciello, O.; Birrell, J.; Carlisle, J. A.; Curtis, L. A.; Goyette, A. N.; Gruen, D. M.; Krauss, A. R.; Schlueter, J.; Sumant, A.; Zapol, P. *Appl. Phys. Lett.* **2001**, 79, 1441.

[22] Yoshiyuki, S.; Malgorzata, A.; Witek, P. S.; Greg, M. S. *Chem. Mater.* **2003**, 15, 879.

---

[23] Chen, Q.; Gruen, D. M.; krauss, A. R.; Corrigan, T. D.; Witek, M.; Swain, G. M. *J. Electrochem. Soc.* **2001**, 148, E44.

[24] Carlisle, J. A. *Nat. Mater.* **2004**, 3, 668.

[25] Swain, G. M.; Anderson, A. B.; Angus, J. C. *MRS Bull.* **1998**, 23, 56.

[26] Hupert, M.; Muck, A.; Wang, J.; Stotter, J.; Cvackova, Z.; Haymond, S.; Show, Y.; Swain, G. M. *Diamond and Related Materials* **2003**, 12, 1940.

[27] Granger, M. C.; Witek, M.; Xu, J.; Wang, J.; Hupert, M.; Hanks, A.; Koppang, M.; Butler, J. E.; Lucazeau, G.; Mermoux, M.; Strojek, J. W.; Swain, G. M. *Anal. Chem.* **2000**, 72, 3793.

[28] Lee, C-S; Baker S. E.; Marcus, M. S.; Yang W.; Eriksson, M. A.; Hamers R. J. *Nano Lett.* **2004**, 4, 1713.

,[29] Delamare, M.; Hitmi, R.; Pinson, J.; Savéant, J. M. *J. Am. Chem. Soc.* **1992**, 114, 5883.

[30] Szunerits, S.; Boukherroub, R. *J. Solid State Electrochem.* **2008**, 12, 1205.

[31] Liu, Y-C; McCreery, R. L. *Anal. Chem.* **1997**, 69, 2091.

[32] Yang, W.; Baker, S. E.; Butler, J. E.; Lee, C-S; Russell, J. N.; Shang L.; Sun, B.; Hamers, R. J. *Chem. Mater.* **2005**, 17, 938.

[33] Lud, S. Q.; Steenackers, M.; Jordan, R.; Bruno, P.; Gruen, D. M.; Feulner, P.; Garrido, J. A.; Stutzmann, M. *J. Am. Chem. Soc.* **2006**, 128, 16884.

[34] Pinson, J.; Podvorica F. *Chem. Soc. Rev.* **2005**, 34, 429.

[35] Allongue, P.; Delamar, M.; Desbat, B.; Fagebaume, O.; Hitmi, R.; Pinson, J.; Serveant, J. M. *J. Am. Chem. Soc.* **1997**, 119, 201.

[36] Rezek, B.; Shin, D.; Nebel, C. E. *Langmuir* **2007**, 23, 7626.

[37] Wang, J.; Carlisle, J. A. *Diam. Rel. Mater.* **2006**, 15, 279.

[38] Zhong, Y. L.; Loh, K. P.; Midya, A.; Chen, Z-K. *Chem. Mater.* **2008**, 20, 3137.

[39] Rouse, A. A.; Bernhard, J. B.; Sosa, E. D.; Golden, D. E. *Appl. Phys. Lett.* **1999**, 75, 3417.

[40] Strother, T.; Knickerbocker, T.; Russell, J. N.; Butler, J.; Smith, L. M.; Hamers, R. J. *Langmuir* **2002**, 18, 968.

[41] Nichols, B. M.; Butler, J. E.; Russell, J. N.; Hamers, R. J. *J. Phys. Chem. B* **2005**, 109, 20938.

[42] www.cse.unt.edu/~smohanty/research/JournalPapers/2006/MohantyIEEEPotentials2006**Biosensors**.pdf

[43] Clark Jr, L. C.; Lyons, C. *Ann. NY Acad. Sci.* **1962**, 102, 29.

---

[44] Ferri, T.; Poscia, A.; Santucci, R. *Bioeletrochem. Bioenergetics.* **1998**, 45, 221.

[45] Rajagopalan, R.; Aoki, A.; Heller, A. *J. Phys. Chem.* **1996**, 100, 3719.

[46] Ang, P. K.; Loh, K. P.; Thorsten, W.; Milos, N.; Emile, V. H. *Advanced Functional Materials* **2009**, 19, 109.

[47] Zhong Y. L.; Chong, K. F.; Paul, M. W.; Chen, Z-K.; Loh, K. P. *Langmuir* **2007**, 23, 5824.

[48] Gorton, L. *Electroanalysis* **1995**, 7, 23.

[49] Cullen, D. C.; Sethi, R. S.; Lowe, C. R. *Anal. Chim. Acta* **1990**, 231, 33.

[50] Yánez-Sedeno, P.; Pingarrón, J. M. *Analytical and Bioanalytical Chemistry* **2005**, 382, 884.

[51] Härtl, A; Schmich, E.; Garrido, J. A.; Hernando, J.; Catharino, S. C. R.; Walter, S.; Feulner, P.; Kromka, A.; Steinmüller, D.; Stutzmann, M. *Nat. Mater.* **2004**, 3, 736.

[52] Wang, J. *Electroanalysis* **2004**, 17, 7.

[53] Yang, W.; Auciello, O.; Butler, J. E.; Cai, W.; Carlisle, J. A.; Gerbi, J. E.; Gruen, D. M.; Knickerbocker, T.; Lasseter, T. L.; Russell, J. N. Jr.; Smith, L, M.; Hamers, R. J. *Nat. Mater.* **2002**, 1, 253.

[54] Homsy, C. A.; Ansevin, K. D.; Obannon, W.; Thompson, S.A.; Hodge, R.; Estrella, M. E. *J. Macromol. Sci-Chem.* **1970**, A4, 615.

[55] Williams, D. F. *Biomaterials* **2008** , 29, 2941.

[56] Spitsyn, B. V.; Bouilow, L. L.; Derjaguin, B. V. *J. Cryst. Growth* **1981**, 52, 219.

[57] O'Hera, M. E.; McHargue, C. J.; Clausing, R. E.; Oliver, W. C.; Parrish, R. H. *Mater. Res. Soc. Extended Abstr.* **1989**, 19, 131.

[58] Drory, M. D.; Gardinier, C. F.; Speck, J. S. *J. Am. Ceram. Soc.* **1991**, 74, 3148.

[59] Hayward, I. P.; Singer, I. L. *Proc. 2nd Intl. Conf. New Diamond Sci. Technol.* **1986**, 785.

[60] Spear, K. E. *J. Am. Ceram. Soc.* **1989**, 72, 171.

[61] Tang, L.; Tsai, C.; Gerberich, W. W.; Kruckeberg, L.; Kania, D. R. *Biomaterials* **1995**, 16, 483.

[62] Nordsletten, L.; Hogasen, A. K. M.; Konttinen, Y. T.; Santavirta, S.; Aspenberg, P.; Aasen, A. O. *Biomaterials* **1996**, 17, 1521.

[63] Amaral, M.; Dias, A. G.; Gomes, P. S.; Lopes, M. A.; Silva, R. F.; Santos, J. D.; Fernandes, M. H. *J. of Biomed. Mater. Res. A* **2007**, 87, 91.

Chapter 2. Experimental

2.1 Introduction

In the present work, various characterization techniques have been employed to provide the best possible elucidation for the surface, as well as the biological and electrochemical properties on a carbon platform. This chapter briefly describes the experimental techniques used in this work.

2.2 Surface Analysis

2.2.1 X-Ray Photoelectron Spectroscopy (XPS)

X-ray photoelectron spectroscopy is one the most widely used techniques in the area of surface analysis as it can measure the elemental composition, empirical formula, chemical state and electronic state of the elements that exists within a material[1]. XPS uses highly focused monochromatic soft x-rays to irradiate the sample surface under ultrahigh vacuum conditions. The commonly used x-ray sources for XPS are Al Kα (1486.6 eV) and Mg Kα (1253.6 eV) as these photons are relatively “clean” with few satellites peaks, resulting in relatively narrow line widths. Am x-ray photon is absorbed by an atom on or near the surface, leading to the photoionization and the emission of a core inner shell electron to the vacuum[2], as illustrated in Figure 2.1. The kinetic energy of the emitted electron can be measured by using an electron energy analyzer. The binding energy (E_B) is calculated as

$$E_B = h\nu - E_{kin} - \Phi \qquad \text{(Equation 2.1)}$$

where Φ is the work function of the spectrometer, E_B is the binding energy with respect to the Fermi level, and E_{kin} is the kinetic energy of the emitted electron. Each photoexcited atom will exhibit a characteristic binding energy of the core-level electron, and this varies with different chemical environments (oxidation state, lattice site and molecular environment, etc.) of the atom by creating a chemical shift of up to a few eV. This provides very useful information for the investigation of surface modification.

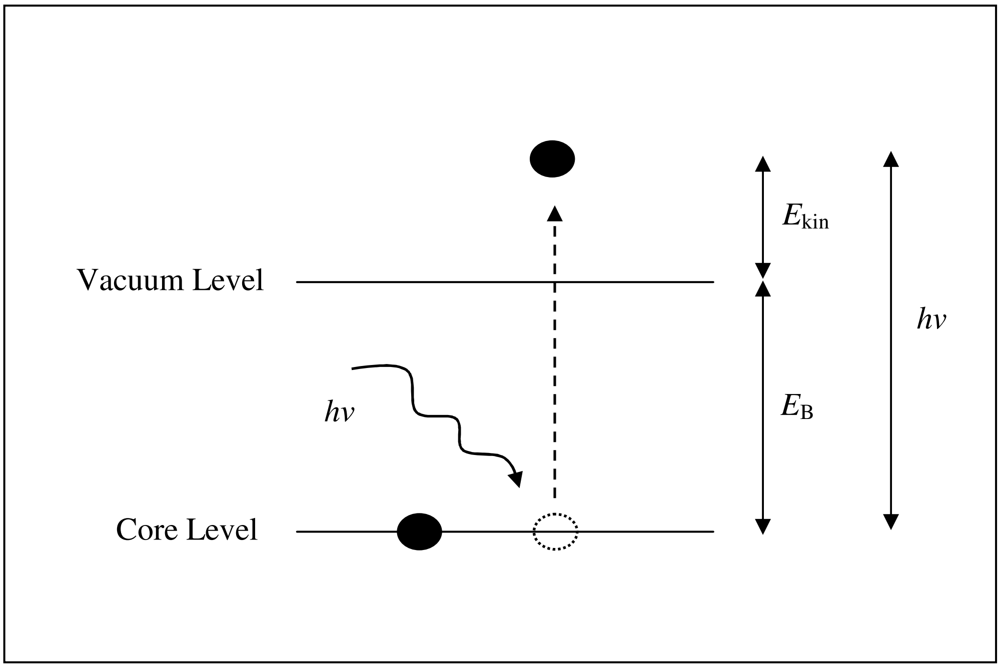

Figure 2.1 Schematic diagram showing photoionization and electron emission by incident x-ray.

2.2.2 Scanning Electron Microscopy (SEM)

In order to gain better understanding of surface morphology, maximum resolution on the surface image must be obtained. However, the maximum resolution mainly depends on the wavelength of the radiation selected for the image. For the normal light optical microscopes the maximum resolution is limited by the visible light wavelength of between 400 nm to 700 nm and a degree of magnification beyond 1000 is difficult.

To achieve higher magnification, electrons are used as these provide smaller wavelengths. In Scanning Electron Microscopy (SEM), images of the samples are obtained by scanning the surface with a high energy beam of electrons in a raster scan pattern. An electron beam is thermionically emitted from an electron gun fitted with a tungsten filament cathode. Tungsten is normally used in thermionic electron guns as it has the highest melting point and lowest vapour pressure of all metals, thereby allowing it to be heated for electron emission and because of its low cost. The electron beam, which typically has an energy ranging from a few hundred eV to 40 keV, is focused by one or two condenser lenses to a spot about 0.4 nm to 5 nm in diameter. The beam passes through a pairs of scanning coils in the objective lens, which deflect the beam in a raster fashion over a rectangular area on the sample surface. When the primary electron beam interacts with the sample, the electrons lose energy by repeated random scattering and absorption within a teardrop-shaped volume of the specimen known as the interactive volume, which extends from less than 100 nm to around 5 μm into the surface. Depending on the sample, the interaction can generate secondary electrons from the primary electrons, backscattered electrons, x-rays, light, heat and even transmitted electrons that pass through the sample. The interaction and generated signals can be schematically illustrated as Figure 2.2. The generated signals will be detected by a scintillator-photomultiplier device and a digital image will be generated. The resolution of an SEM is within ~2 nm and a magnification up to 200000 times can be obtained.

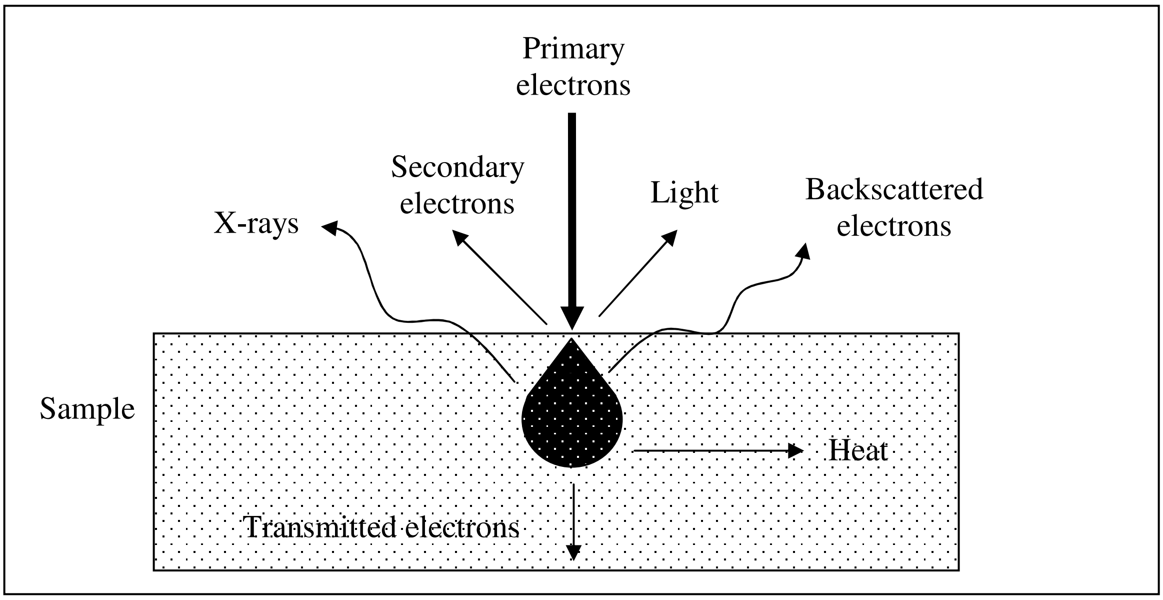

Figure 2.2 The interaction of primary electrons with a sample and the generated signals.

2.2.3 Atomic Force Microscopy (AFM)

The atomic force microscope (AFM) is one of the high resolution scanning probe microscopy methods that can provide resolution at the nanometer scale. Since the first invention of AFM by Binnig *et. al.* in 1986[3], it has been developed to be the foremost tool for imaging the surface topography, measuring and manipulating matter at the nanoscale. The basic AFM working unit consists of a cantilever with a sharp tip, laser, photodiode, detector and feedback electronics and piezoelectric scanner. It is schematically illustrated in Figure 2.3. Conventionally, the sample rests on a piezoelectric scanner during the scanning process. It can be moved in the z direction for maintaining a constant force, and the x and y directions for image scanning. The cantilever with a sharp tip plays a vital role in the AFM system for the scanning of the sample surface. The cantilever is typically silicon or silicon nitride with a tip radius of curvature of the order of nanometers. When the tip is moved into the proximity of a sample surface, forces between the tip and the sample lead to a deflection of the cantilever according to Hooke's Law. Some of the forces that are measured by AFM include mechanical contact force, van der Waals forces, magnetic forces, Casimir forces, solvation forces, etc. The cantilever deflection is measured by using a laser spot reflected from the top surface of the cantilever into an array of photodiodes into which the detector is connected. If the tip is scanned at a constant height, there is possibility that the tip collides with the surface causing damage to the tip. Hence, in most cases a feedback mechanism is installed to maintain a constant force between the tip and the sample by continuous adjustment of the tip-to-sample distance.

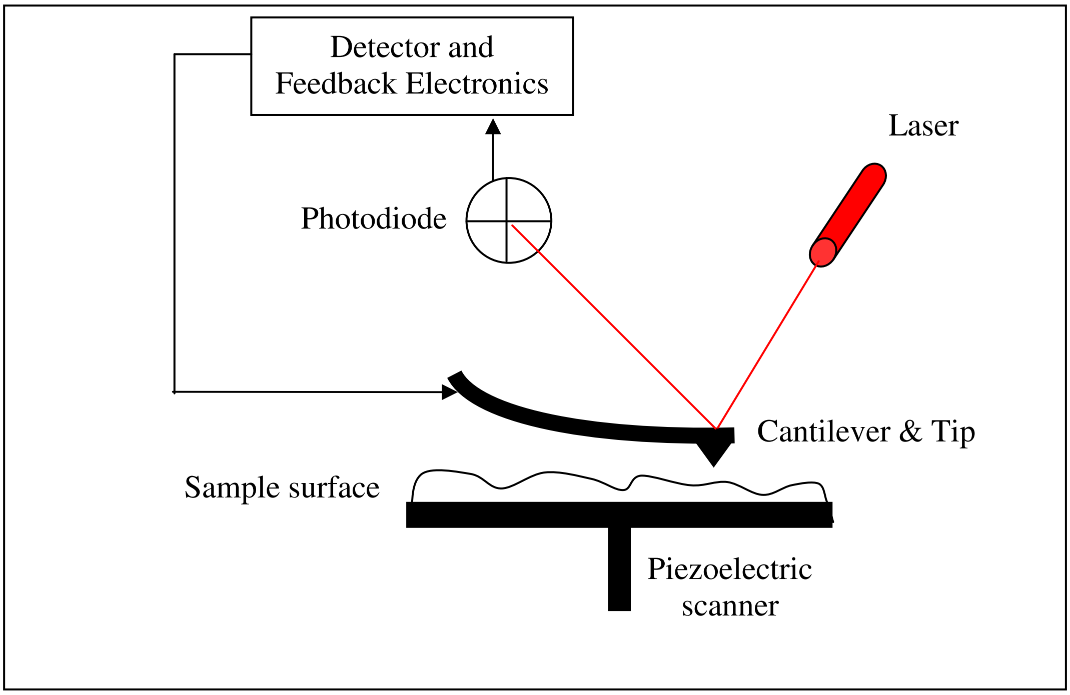

Figure 2.3 Schematic diagram of AFM working principle.

In general, the imaging mode of AFM can be operated in static modes and dynamic modes. In static mode, the static tip deflection is used as a feedback signal. Because the measurement of the static signal is prone to noise and drift, low stiffness cantilevers are used to boost the deflection signal. However, the attractive forces can be quite strong at close proximity to the sample surface, causing the tip to "snap-in" to the surface. Hence, the force between the tip and the surface is kept constant during scanning in contact mode by maintaining a constant cantilever deflection. In dynamic mode, the cantilever is externally oscillated at or close to its fundamental resonance frequency and this oscillation amplitude, phase and resonance frequency are modified by the tip-sample interaction force; these changes in oscillation with respect to the external reference oscillation provide information about the sample surface characteristics. The modulation in dynamic mode can be by frequency modulation or amplitude modulation. In frequency modulation, changes in the oscillation frequency provide information about tip-sample interactions. Normally, stiff cantilevers are used in this modulation mode and the frequency can be measured at high sensitivity. In amplitude modulation, changes in the oscillation amplitude or phase provide the feedback signal for imaging. Unlike frequency modulation, changes in the oscillation phase or amplitude are used to probe the tip-sample interaction in amplitude modulation mode.

Besides imaging of surface topography, another major application of AFM is force spectroscopy. This is the measurement of the applied cantilever force as a function of its distance from the surface. In this method, the AFM tip is extended towards the sample surface and retracted from the surface and the static deflection of the cantilever is monitored as a function of piezoelectric displacement. Forces of the order of a few pico-Newtons can be measured with a vertical distance resolution of better than 0.1 nm. Adhesion forces between individual ligand-receptor pairs can be studied by using AFM in force mode[4].

2.2.4 Contact Angle Measurement

The contact angle is the angle at which a liquid/vapor interface meets the solid surface. It is specific for any given system and is determined by the interactions across the three interfaces, ie. gas, liquid and solid. It is often tested by resting a small liquid droplet on a flat horizontal solid sample surface and the contact angle of the water droplet is measured by goniometer (Figure 2.4). Consider a strongly hydrophilic surface, the liquid droplet is very strongly attracted to the surface and the droplet will completely spread out on the solid surface causing the contact angle to be nearly 0°. On many hydrophilic surfaces, the water droplet will exhibit contact angle of 0° to 90°. Contrary to hydrophilic surface, water droplets will show higher contact angle values on hydrophobic surfaces or even as high as 180° on superhydrophobic surfaces, without actually wetting to any significant extent. Contact angle measurement is widely used in surface science to determine the hydrophobicity of the sample surface.

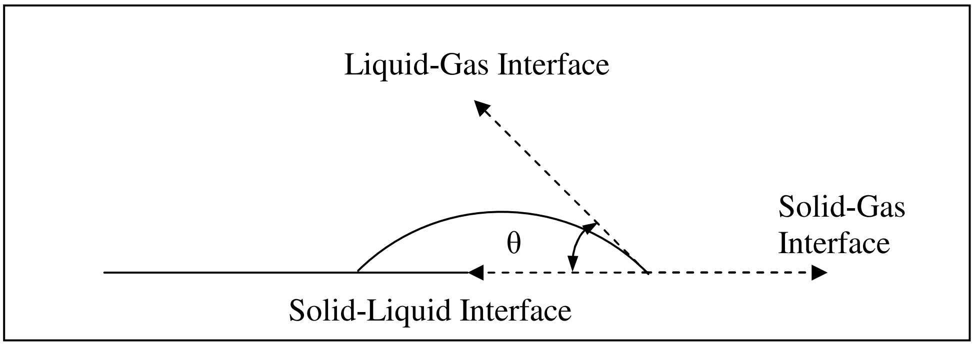

Figure 2.4 Contact angle, θ of a liquid droplet on a solid surface.

2.2.4 Toluidine Blue O (TBO) Stain Measurement

The surface density of a carboxyl group can be quantitatively measured by using a staining dye method. This is a convenient method as it does not involve sophisticated instruments and only a spectrophotometer is needed. Toluidine blue O

(TBO), (also known as tolonium chloride) was originally used in histology for cells and tissues staining. Its unique structure (Figure 2.5) allows it to form ionic complexes with carboxyl groups producing a red colour (633 nm). This renders it to be modified as the dye for surface carboxyl groups[5]. The colour intensity is measured and the corresponding surface-carboxyl-group concentration is then determined by comparing with the known standard calibration plot.

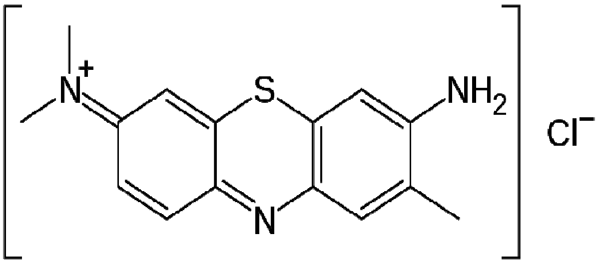

Figure 2.5 Toluidine blue O chemical structure.

2.3 Biological Analysis

2.3.1 Hoechst Stain Assay

In biological studies involve cell culture methodology, cell number quantitation is one of the important analysis methods. As every cell contains a large pool of DNA in the nucleus, DNA quantitation can be an indirect method for cell number quantitation. The DNA assays selected for quantitation must (a) allow quantitative and reproducible extraction of DNA, (b) preserve the double-stranded structure of DNA since the fluorescence enchancement is greatly reduced upon binding of this fluorochrome to single-stranded DNA[6], (c) dissociate or modify the conformation of chromosomal proteins so that the accessibility of DNA-binding sites is not limited[7], (d) inhibit endogenous DNAase activity and (e) prevent excessive alteration of the intrinsic fluorescence of the dye. Th Hoechst stain has proven to be an excellent reagent to meet the above-mentioned criteria[8]. Hoechst 33258 stain 2(2-(4-hydroxyphenyl)-6-benzimidazole-6-(1-methyl-4-piperazyl)-benzimidazole trihydrochloride (Figure 2.6) is a cell-permeable DNA stain for DNA labeling in fluorescence microscopy and cell assay. It is excited by ultraviolet light at around 350 nm and emits blue/cyan fluorescence light around 460 nm. Hence, the staining of the cell DNA will be an indicator for the cell number quantitation. As Hoechst stain binds to DNA and will disrupt DNA replication during cell division, it is potentially mutagenic and carcinogenic and care should be taken during handling and disposal.

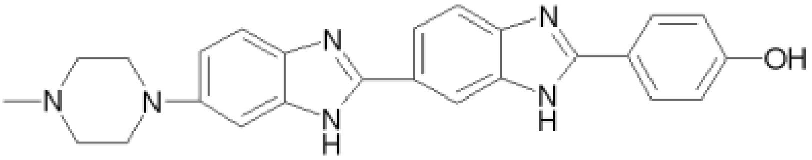

Figure 2.6 Hoechst 33258 stain 2(2-(4-hydroxyphenyl)-6-benzimidazole-6-(1-methyl-4-piperazyl)-benzimidazole trihydrochloride chemical structure.

2.3.2 MTT Assay

MTT (3-(4,5-dimethylthiazol-2-yl)-2,5-diphenyltetrazolium bormide, a tetrazole) is a standard colorimetric assay for the measurement of cell viability. MTT is originally yellow in color and it will be reduced to purple-colored formazan by the mitochondrial reductase activity in living cells[9]. It provides cell viability information as the mitochondrial reductase activity is greatly reduced in living cell and the amount of formazan generated is directly proportional to the living cells population. The structural conversion of MTT to formazan is schematically illustrated in Figure 2.7. Since purple formazan is insoluble, a solubilization solution such as detergent sodium dodecyl sulfate (SDS) will be added to dissolve formazan into the solution. The absorbance of this colored solution can be quantified by measuring at 595 nm wavelength by a spectrophotometer. It is widely used to determine the cytotoxicity of potential medicinal agents. The main advantage of this colorimetric assay is the speed of measurement, as multiwell scanning spectrophotometers or ELISA readers can be used to process large numbers of samples and no removal or washing steps are required.

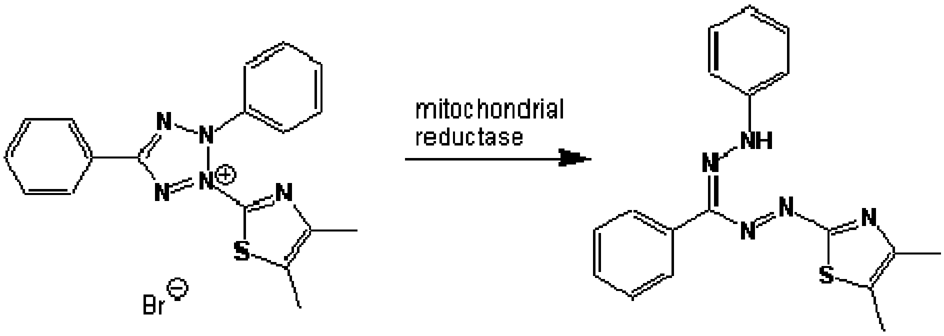

MTT (Yellow color) Formazan (Purple color)

Figure 2.7 Structural conversion of MTT to formazan by mitonchrondrial activity in living cells.

2.3.3 Live/Dead Viability/Cytotoxicity Kit

The Live/Dead Viability/Cytotoxicity Assay kit provides a two-color fluorescence cell viability assay that is based on the simultaneous determination of live and dead cells with two probes that measure recognized parameters of cell viability – intracellular esterase activity and plasma membrane integrity. It is a useful kit for the simultaneous imaging of the live and dead cells under the fluorescence microscope. Calcein AM and ethidium homodimer (EthD-1) are used as the staining reagent in this kit[10]. Live cells are distinguished by the presence of ubiquitous intracellular esterase activity and it can be determined by the enzymatic conversion of nonfluorescent cell-permeant calcein AM to the intensely fluorescent calcein. The polyanionic dye calcein is well retained within live cells, producing an intense green fluorescence in live cells which can be visualized with excitation at 495 nm and emission at 515 nm. EthD-1 enters cells with damaged membranes and undergoes an intense enhancement of fluorescence upon binding to nucleic acids, thereby producing bright red fluorescence in dead cells, which can be visualized with excitation at 495 nm and emission at 635 nm. This red-fluorescent EthD-1 is excluded by the intact plasma membrane of live cells. The determination of cell viability depends on these physical and biochemical properties of cells. Cytotoxic events that do not affect these cell properties may not be accurately assessed using this method. Background fluorescence levels are inherently low with this assay as these dyes are virtually non-fluorescent outside cells membrane.

2.4 Electrochemical Analysis

A three-electrode electrochemical setup is commonly used in electrochemical systems. It consists of a reference electrode, a working electrode and a counter electrode. The three electrodes are immersed in the test solution, and electrolyte is normally added to ensure sufficient conductivity for electrochemical analysis. The test solution can be in a static or dynamic condition, depending on the type of electrochemical analysis. Common materials for the working electrode include glassy carbon, platinum, gold and conducting inert materials that do not react with the test solution. The working electrode is fabricated to have a controlled surface area and well-defined shape as these two criteria greatly affect the electrochemical analysis. In electrochemical systems, the process of charge transport across the interface between the working electrode and the solution is studied. Hence, the working electrode plays a vital role throughout the process. The electron transfer between the working electrode, the test solution and the electrochemical potentiostat is completed by the counter electrode, which is normally made of platinum. A reference electrode is added in order to ensure that the measured potential is quoted with respect to a standard value. It is normally made up of a silver-silver chloride electrode for aqueous solutions. There are numerous types of electrochemical analyses which provide different information based on electron/charge transfer.

2.4.1 Cyclic Voltammetry (CV)

Cyclic voltammetry (CV) is a type of potentiodynamic electrochemical measurement in which the working electrode potential is ramped linearly versus time to a set potential and then the electrode potential ramp is inverted. This inversion or cycle can be repeated multiple times depending on the experimental setting. The potential waveform in CV is shown in Figure 2.8. The ramping rate is known as the scan rate (V/s). The current at the working electrode is measured and plotted versus the applied voltage and a cylic voltammogram will be obtained. In the forward scan, the current will increase as the potential reaches the electrochemical potential of the analyte in the solution, but then decrease as the concentration of the analyte is depleted close to the electrode surface. If the redox analyte is electrochemically reversible, it will be oxidized (if it is reduced in the forward scan) or reduced (if it is oxidized in the forward scan) back in the backward scan. In order for the oxidation/reduction peak to be observed, the redox analyte must be redox active within the electrochemical window of the working electrode and the electrolyte solution. The oxidation peak will usually have a similar shape to the reduction peak.

However, there is a potential gap between absolute potential between the oxidation and reduction peak. This potential gap is attributed to the analyte diffusion rates and the intrinsic activation barrier of transferring electrons from an electrode to the analyte. For an ideal reversible redox analyte, the relationship between the oxidation (E_{ox}) and reduction (E_{red}) potential can be described by both the Butler-Volmer equation and Cottrell equation, and it is simplified as Equation 2.2[11]. n is the number of electrons involved in the redox process. The ideal reversible redox electrochemical system will obey Equation 2.2 and show a peak separation of 59 mV in a cyclic voltammogram. Thermodynamic information can be extracted from the cyclic voltammogram.

$$| E_{ox} - E_{red} | = 59 \text{ mV} / n \qquad \text{(Equation 2.2)}$$

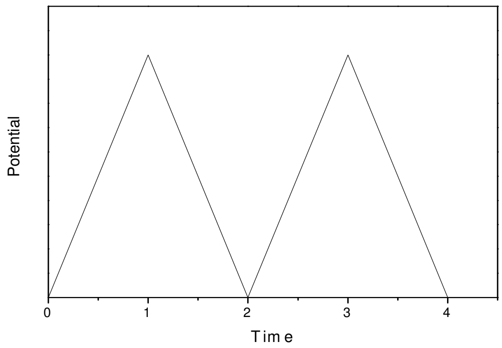

Figure 2.8 Potential waveform versus time for cyclic voltammetry.

2.4.2 Chronoamperometric

Chronoamperometry is an electrochemical technique in which the applied potential of the working electrode is constant for a period of time and the resulting current from faradaic processes at the working electrode is monitored as a function of time. A potential step can be applied to measure the background current at different potentials. The potential waveform for chronoamperometry is shown in Figure 2.9.

The background current remains constant in the electrolyte solution for the applied potential until an electrochemically active species is added to the solution, where upon the background current will increase. In order for the electrochemically active species to be detected in chronoamperometry, the applied potential must be higher than the electrochemical potential of the species. Chronoamperometry is a useful technique for electrochemical biosensor testing in which a trace amount of an analyte can be detected instantaneously. The signal-to-noise ratio must be higher than 3 in order for the chronoamperometry result to be reliable. However, limited information about the identity of the redox species can be obtained from this electrochemical method.

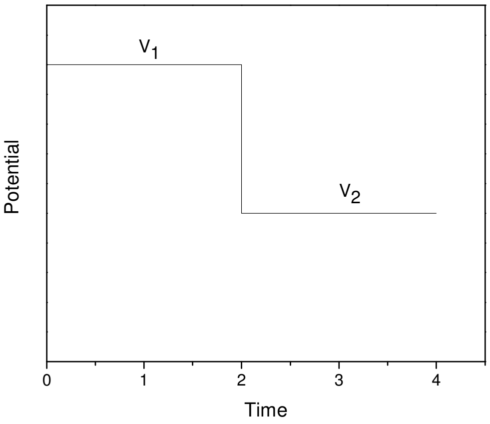

Figure 2.9 Potential waveform versus time for chronoamperometry.

2.4.3 Stripping Voltammetry

Stripping voltammetry is one type of electrochemical method in which the preconcentration of analyte from the solution is attached onto the surface of a working electrode by applying a potential. The electrodeposited analyte is then redissolved from the electrode by scanning the potential towards the positive or negative direction and the corresponding current is measured. The conventional electrode for stripping voltammetry is mercury as it will form an amalgam with any preconcentrated heavy metal ions. The analyte signal is intensely increased compared to other voltammetry methods as the analyte is preconcentrated at the working electrode surface before the scanning process. There are two types of stripping voltammetry, namely anodic stripping voltammetry (ASV) and cathodic stripping voltammetry (CSV). In ASV, a negative potential is applied to the working electrode during the preconcentration process and the potential is ramped in the positive direction during the stripping process. On the other hand, a positive potential is applied to the working electrode for CSV during the preconcentration process and the potential is scanned towards the negative direction during the stripping process. The process of ASV and its potential waveform is schematically illustrated in Figure 2.10. Stripping voltammetry is normally initiated with a cleaning step, whereby the electrode potential is held at a higher value than the electrochemical potential of the analyte for a period to time in order to fully remove it from the electrode. The working solution is stirred continuously throughout the stripping analysis except for during the rest period when a static condition is required.

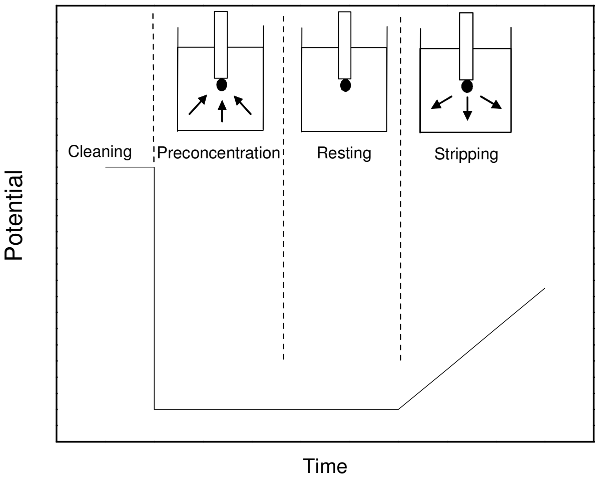

Figure 2.10 Process of ASV and its potential waveform versus time.

2.4.3 Electrochemical Impedance Spectroscopy (EIS)

Electrochemical impedance spectroscopy (EIS) is an electrochemical method which applies very small amplitude signals to the system and measures its impedance over a range of frequencies. A small alternating current signal, usually a voltage between 5 to 50 mV, is applied to a system over a range of frequencies of 0.001 Hz to 100,000 Hz. The response to this potential is an AC current signal containing excitation frequency and harmonics. This current signal is analyzed as a sum of sinusoidal functions. An EIS instrument records both the real and imaginary components of the impedance response. Data obtained from EIS is expressed graphically in a Bode plot or a Nyquist plot.

The understanding of impedance is crucial in the context of EIS. The different electrochemical systems in the solution can be represented by an equivalent circuit model. However, using real circuit elements to represent the system is very complex and the resistance in the circuit cannot be merely explained by Ohm's Law. Hence, impedance is used in place of resistance. Similar to resistance, impedance is a measurement of the ability of a circuit to resist the flow of electrical current. Table 2.1 compares a resistor and a capacitor and the equation for their current versus voltage and impedance relationship. The impedance of a resistor is independent of frequency and has only a real component. As there is no imaginary impedance, the current passing through a resistor is always in phase with the voltage. On the other hand, the impedance of a capacitor is dependent on frequency and consists of real and imaginary components as described by parameter j. This technique has grown tremendously in stature over the past few years and is now being widely used in a wide variety of scientific fields, such as fuel cell testing and biomolecular interaction. EIS also reveals information about the reaction mechanisms of an electrochemical process, as different reaction steps will dominate at certain frequencies and the frequency response shown by EIS can help identify the rate-limiting step.

Component	Current vs. Voltage	Impedance
Resistor	$E = IR$	$Z = R$
Capacitor	$I = C\, \mathrm{d}E/\mathrm{d}t$	$Z = 1/j\omega C$

Table 2.1 Comparison between a resistor and a capacitor.

References

---

[1] Moulder J. F.; Stickle, W. F.; Sobol, P. E.; Bomber, K. D. *Handbook of X-ray Photoelectron Spectroscopy*, Physical Electronics Division, Perkin-Elmer Corporation, Minnesota, 1991.

[2] Nordling, C.; Sokolowski, E.; Siegbahn, K. *Phys. Rev.* **1957**, 105, 1676.

[3] Binnig, G.; Quate, C. F.; Gerber, C. *Phys. Rev. Lett.* **1986**, 56, 930.

[4] Florin, E-L.; Moy, V. T.; Gaub, H. E. *Science* **1994**, 264, 415.

[5] Sano, S.; Kato, K.; Ikada, Y. *Biomaterials* **1993**, 14, 817.

[6] Brunk, C. F.; Jones, K. C.; james T. W. *Anal. Biochem.* **1979**, 92, 497.

[7] Labarcam, C.; Paigen, K. *Anal. Biochem.* **1980**, 102, 344.

[8] Downs, T. R.; Wilfinger W. W. *Anal. Biochem.* **1983**, 131, 538.

[9] Mosmann, T. *J. Immunol. Methods* **1983**, 65, 55.

[10] Papadopoulos, N. G.; Dedoussis, G. V. Z.; Spanokos, G.; Gritzapis, A. D.; Baxevanis, C. N.; Papamichail, M. *J. Immunol. Methods* **1994**, 177, 101.

[11] Bard, A. J.; Faulkner, L. R. *Electrochemical Methods: Fundamental and Applications (2nd ed.)* Wiley, United States of America, **2000**, 240.

Chapter 3. Cell Adhesion Properties on Photochemically Functionalized Diamond

The biocompatibility of diamond was investigated with a view towards correlating surface chemistry and topography with cellular adhesion and growth. The adhesion properties of normal human dermal fibroblast (NHDF) cells on microcrystalline and ultrananocrystalline diamond surfaces were measured using atomic force microscopy. Cell adhesion forces increase by several times on the hydrogenated diamond surfaces after UV irradiation of the surfaces in air, or after functionalization with undecylenic acid. A direct correlation between initial cell adhesion forces and the subsequent cell growth was observed. Cell adhesion forces were observed to be strongest on UV-treated ultrananocrystalline diamond, and cell growth experiments showed that ultrananocrystalline diamond was intrinsically more biocompatible than microcrystalline diamond surfaces. The surface carboxylic acid groups on a functionalized diamond surface provide tethering sites for laminin to support the growth of neuron cells. Finally, using capillary injection, a surface gradient of polyethylene glycol could be assembled on top of the diamond surface for the construction of a cell gradient.

3.1 Introduction

Diamond has been claimed to be an excellent biocompatible material, although the basis of this statement has not been thoroughly qualified in the context of its surface chemistry and topography. The surface properties of diamond can be made hydrophobic or hydrophilic with hydrogen or oxygen termination[1], respectively, which have implications for cellular adhesion. Photochemical coupling of organic molecules onto a hydrogen-terminated diamond surface was pioneered by Hamers[2], and biorecognition events based on impedimetric sensing have been achieved on these platforms[3]. In terms of cell growth, the ordered growth of neurons has been demonstrated by Specht and coworkers[4] on protein-coated diamond using micro-contact printing. Neuronal cell excitability on functionalized diamond surfaces have been shown by Ariano and coworkers.[5] However, the cellular adhesion properties of as-grown diamond surfaces or functionalized diamond surface have not been studied in detail.

Cellular adhesion is of fundamental importance in many biological processes as the adhered cells will sense, interpret, integrate and respond to the extracellular signals. Chemical and physical signals from the substrate such as surface energy, topography, electrostatic charge and wettability play a vital role in stimulating cell adhesion and influencing cell growth behavior. The physiochemical effects of different functional groups on cellular attachment have been extensively studied[6,7]. On the other hand, surface topography is also an important biomimic stimulator for cell growth because the *in vivo* growth of cells occurs on biological interfaces[8,9] that usually have nanotopographical features[9].

In order to develop diamond as a signal transduction platform for the optical or electrical monitoring of cellular activities, strong cellular adhesion on the surfaces of diamond must be achieved, because the cell and its adhesive components will be subjected to external perturbation in continuous flow systems. An AFM operated in force mode has been used in probing the interaction forces between cell-surface[10], cell-cell[11], biotin-streptavidin[12], antibody-antigen[13], and complementary strands of DNA oligomers[14]. Nebel and coworkers recently applied AFM to study the forces needed to remove bonded DNA from single crystal diamond[14]. The adhesion forces of NHDF cells on a diamond surface with different surface chemistry and topography were investigated. Photochemical functionalization of the diamond using simple UV irradiation in air, or via alkene acids groups[15], were evaluated comparatively in terms of biocompatibility. To assess the role of surface energy and topography on cell growth, the surface conditions and topography of diamond were correlated with the cell adhesion forces, cell attachment and cell viability. In addition, the carboxylic acid groups present on a functionalized diamond surface was coupled to an active protein layer in order to support neuronal cell growth. Finally, by controlling the gradient of polyethylene glycol on the surface, a cell gradient has also been successfully generated on a diamond surface. Such cellular gradients could potentially provide an experimental platform for combinatorial discovery and analysis.

3.2 Experimental Section

3.2.1 Chemicals

All the chemicals used in this experiment were purchased from Sigma Aldrich unless otherwise stated and were used as received. A polyethylene glycol (PEG) derivative (relative molecular weight = 5197) possessing an amine end-group, referred to as m-PEG-NH_2, was purchased from NOF Corporation.

3.2.2 Sample Preparation

Sub-micron grain-size, 5 µm thick microcrystalline diamond was obtained from Adamant electrodes. Ultrananocrystalline diamond of about 1-2 µm thickness on silicon was supplied by rho-BeSt coating. Diamond samples were cleaned and chemically oxidized with hot 'Piranha' solution (30% H_2O_2 : 97% H_2SO_4 = 1 : 3) for 1 hour, followed by rinsing with ultrapure water. The samples were then rinsed with tetrahydrofuran followed by hexane. Cleaned diamond samples were hydrogen-terminated by hydrogen plasma treatment at 800 W in a microwave plasma CVD system under 300 sccm hydrogen gas flow for 15 min. All freshly prepared hydrogen-terminated diamond samples (denoted as H-terminated hereafter) were used immediately for surface treatment and cell culture.

3.2.3 UV Oxygenation

Hydrogen-plasma treated diamond samples was exposed to UV irradiation (18 W, 254 nm) in air for 18 hours (hereafter denoted as UV-treated diamond) in air.

3.2.4 UV Photochemical Grafting

UV photochemical grafting of the carboxylic acid functional group was achieved by covering the H-terminated diamond samples with a thin layer of undecylenic acid (UA), and introducing the sample into a chamber maintained in positive nitrogen pressure. Samples were exposed to the UV irradiation (18 W, 254 nm) for 18 hours through an UV transparent quartz window. After UV functionalization, the samples (hereafter known as UA-functionalized diamond) were rinsed with ultrapure water, tetrahydrofuran and finally with hexane. All prepared samples were used within 24 hours.

3.2.5 X-ray Photoelectron Spectroscopy

X-ray photoelectron spectroscopy (XPS) was preformed with VG ESCALAB MkII spectrometer using an unmonochromatized Mg Kα X-ray source (1253.6 eV). The pass energy of the hemispherical analyzer was set at 50 eV for wide scan and 20 eV for narrow scan.

3.2.6 Morphology and Topography

Surface morphology of microcrystalline and ultrananocrystalline diamond were observed by a JEOL 6701 FESEM (Field Emission Scanning Electron Microscope) and the surface topography were investigated by an Atomic Force Microscope XE-100 from PSIA.

3.2.7 Wettability Behavior

Contact-angle measurements were performed with a Rame-Hart Contact Angle Goniometer. 3 μL of ultrapure water was placed on the prepared samples and three measurements were taken for each sample.

3.2.8 Surface Carboxylic Acid Group Measurement

The UA-functionalized diamond samples (1 cm^2) were soaked in 5×10^{-4} M toluidine blue O (TBO) solution, and adjusted to pH 10 with NaOH. Formation of ionic complexes between the surface carboxylic acid groups and the cationic dye was allowed to proceed for 5 hours at room temperature, followed by rinsing the samples with NaOH solution to remove the uncomplexed TBO molecules. Desorption of the dye was performed in 50 wt % acetic acid solution and its amount was calculated from its optical density at 633 nm, using a calibrated plot.

3.2.9 Cell Culture

Two cell lines were used in this work, namely Normal Human Dermal Fibroblast (NHDF) cells (PromoCell GmbH, Germany) and Pheochromocytoma (PC12) cells. NHDF cells were routinely cultured at 37°C and 5% CO_2 atmosphere with complete Fibroblast Growth Medium (PromoCell GmbH, Germany) containing insulin (5 μg/mL), basic fibroblast factor (1 ng/mL), penicillin (1000 IU/mL) and streptomycin (1000 μg/mL). PC12 cells were routinely cultured on collagen-coated flasks with RPMI1640 medium supplemented with fetal calf serum (10%), fetal horse serum (5%), penicillin (1000 IU/mL) and streptomycin (1000 IU/mL). NHDF cells or

PC12 cells were seeded at 5×10^4 cells/mL onto 24-well tissue culture plates, containing 1 cm^2 of sample surfaces in each well. For cell seeding onto the PEG-modified gradient surface, an initial cell density of 1.5×10^5 cells/mL was used and a sample with dimension of 2 cm × 2 cm was used. Cells were allowed to attach for 24 h and the loosely attached cells were removed by rinsing with PBS for 3 times.

A fibroblast cell is an anchorage-dependent cell line which is very useful in biocompatibility studies as it will contact with biomaterials upon implantation. Furthermore, it does not require stringent culture conditions and will proliferate readily into the confluence state on a biocompatible material. A PC12 cell is a tumorigenic cell line which will differentiate into sympathetic neurons upon exposure to the nerve growth factor (NGF). It is a very useful cell line for neurotransmitter study as sizeable amounts of neurotransmitter such as dopamine and norepinephrine can be stored in this cell line. However, it requires an Extracellular Matrix (ECM) such as collagen or laminin coating for attachment and differentiation. This requirement is used in this work to assay the coupling efficiency of protein on a functionalized diamond surface.

3.2.10 Attachment of Cells to an AFM Cantilever

Concanavalin A (Con A)-functionalized cantilevers (spring constant of 0.01 N/m, Veeco) were prepared by cleaning tips in acetone for five minutes and then UV irradiating for fifteen minutes followed by incubation in biotinamidocaproyl-labeled bovine serum albumin (0.5 mg/mL in 100 mM $NaHCO_3$) overnight at 37°C. They were then incubated in streptavidin solution (0.5 mg/mL in PBS) for 10 minutes at room temperature after thorough rinsing with PBS. Following the removal of unbound streptavidin, the cantilevers were incubated in biotinylated Con A (1 mg/mL in PBS) for one hour. The Con A-coated cantilever was finally rinsed with PBS for three times before the AFM force measurements.

3.2.11 AFM Force Measurements

Force curves of cell surface interactions were obtained on a MultiMode^{TM} Picoforce^{TM} AFM (Veeco) at room temperature in a fluid cell with medium using the functionalized cantilevers. The spring constant of the cantilever was obtained using the thermal tune module prior to attaching a cell. A small amount of cell suspension obtained by trypsinization was added on to the diamond surface being studied. The Con A-functionalized cantilever was positioned on top of a single NHDF cell and lowered gently. The contact was maintained for a few seconds to allow the NHDF cell to attach to the cantilever. The cantilever with the attached cell was then used to obtain force curves. Each force curve represents a single cycle of approach and retraction of the cell-cantilever system with respect to the surface. All force curves were obtained under similar interaction parameters (contact force of 3 nN, contact time of 200 ms and retraction velocity of 2 $\mu m\ s^{-1}$) and a total of 150 force measurements were done for each sample.

3.2.12 Hoechst Stain Assay

The level of NHDF cell attachment was estimated from the total DNA content measured with Hoechst stain H33258[15]. Cell-attached samples were incubated in 0.02% sodium dodecyl sulfate (SDS)/ saline sodium citrate (SSC) for 1 hour to allow cell membrane lysis, and they were subsequently stained with H33258 (1 ug/mL in SSC) for 15 mins to allow the binding of H33258 with DNA. Finally, fluorescence intensity was assessed using an excitation wavelength of 355 nm and a detection wavelength of 460 nm. The total DNA content was calculated from the standard curve of known DNA concentrations.

3.2.13 MTT-ESTA Assay

The NHDF cell viability was determined by established MTT-ESTA assay[16]. First, the cell-attached samples were incubated in 3-[4,5-dimethylthiazol-2-yl]-2,5-di-phenyl-tetrazolium bromide (MTT) (0.3 mg/mL in PBS) for 2 h. Following cell lysis by SDS, the purple stain was eluted with acidified isopropanol and the optical density was measured at 595 nm. The degree of optical density reflects the total cell viability.

3.2.14 Statistical Analysis

All results are tested with Student’s t-test to identify the significant difference between results. All the results are presented as mean ± standard deviation.

3.2.15 Live/Dead Cytotoxicity® Kit

By using the Live/Dead Cytotoxicity Kit® from Molecular Probes, viable and non-viable cells can be recognized simultaneously without digesting the cells from the sample surface. Both viable cells (fluorescein filter) and non-viable cells (rhodamine filter) were visualized by fluorescent microscope (Olympus BX60) according to the standard protocol from Molecular Probe.

3.2.16 Protein Immobilization

The carboxylic acid group on the UA-functionalized diamond was activated to form an NHS-ester intermediate on the diamond surface by incubating with a solution containing EDC (0.4 M) and NHS (0.1 M) for 1 hour. After rinsing with PBS, it was incubated with laminin solution (0.1 mg/mL in PBS) for 1 hour. To eliminate the unspecific binding of protein, the sample was vortexed in Tween-20 solution (0.5% in PBS) for 30 minutes. After final rinsing with PBS, the sample was used immediately for neuron cell growth experiment.

3.2.17 Gradient Formation

A polyethylene glycol (PEG) surface gradient was achieved by controlling the diffusion of PEG in the polymer gel[17]. The surface carboxylic acid group on diamond was activated similarly to the protein immobilization step, and after thorough rinsing with PBS solution, the NHS-ester modified surface was coated with a layer of 3% agarose gel. A small syringe containing m-PEG-NH_2 (4 mg/mL) solution was pierced into the center of the gel. The syringe was connected to a syringe pump to deliver the PEG solution into the gel at a constant rate of 10 μL/hr for a period of 8h. After peeling the gel from surface, the PEG-modified surface was rinsed with PBS followed by Tris (50 mM) to saturate the unreacted carboxylic acid group. The PEG-modified surface was used immediately after preparation for cell attachment experiment.

3.3 Results and Discussions

3.3.1 Surface Characterization

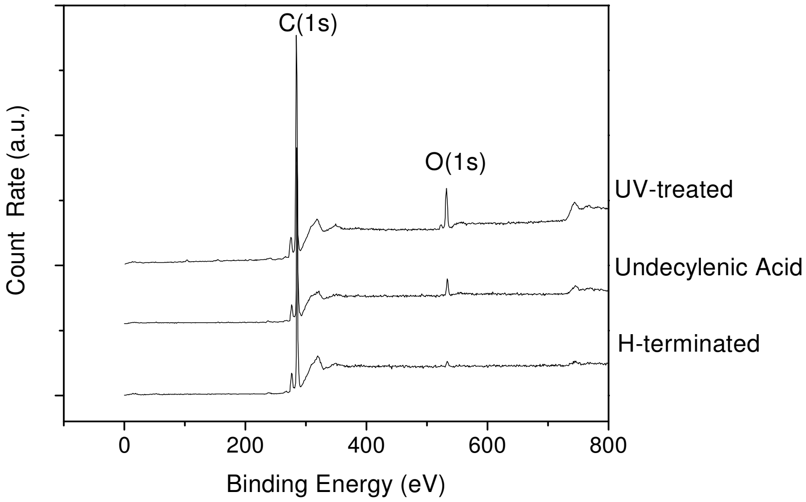

Figure 3.1 XPS wide-scan spectra of H-terminated, undecylenic acid-functionalized and UV-treated diamond.

In Figure 3.1, an XPS wide-scan spectra confirms that the H-terminated diamond surface consisted only of carbon and insignificant amount of oxygen. In contrast, both the UV-treated and UA-functionalized diamonds show appreciable O1s peak intensities at 533 eV, in addition to C1s peak at 285 eV. The C1s narrow scans as shown in Figure 3.2 confirmed the presence of various functional groups by their respective chemical shifts. H-terminated diamond shows only the bulk diamond peak at 284.5 eV, with a narrow full-width-at-half-maximum (FWHM). For UV-treated diamond, the FWHM is much wider, with a broad shoulder extending to 287.5 eV, which can be attributed to the presence of oxygen functionalities related to hydroxyl (OH) or carbonyl (C=O) groups. This proves that the UV irradiation of diamond in air resulted in the oxygenation of the hydrogenated diamond surface, possibly via attack by ozone or hydroxyl radicals generated from moisture. For UA-functionalized diamond, a chemically shifted peak at 289.6 eV due to the presence of carboxylic groups (COOH) can be observed.

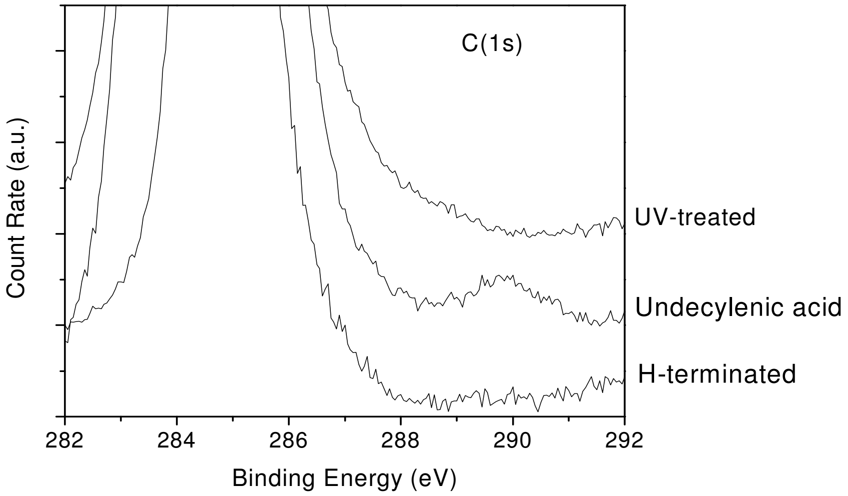

Figure 3.2 XPS C(1s) spectra of H-terminated, undecylenic acid-functionalized and UV-treated microcrystalline diamond.

The diamond surfaces became more hydrophilic after irradiation with UV or functionalization by UA, as evidenced by the wetting angle studies shown in Table 1. UV-treated diamond surfaces were more hydrophilic than the UA-functionalized diamonds, which can be attributed to the higher oxygen content on the UV-treated surfaces. The TBO method was employed to determine the amount of carboxylic acid groups on the UA-functionalized diamond surfaces, as shown in Table 1. The ultrananocrystalline diamond surface provides a higher surface area for the grafting of UA molecules compared to that of microcrystalline diamond. The surface morphology of microcrystalline diamond is shown in Figure 3.3a, where a sub-micron grain size of between 100-300 nm can be seen. Figure 3.3b shows that the ultrananocrystalline diamond has finer grain size in the range of 5-10 nm. Figure 3.4 shows the three-dimensional surface topography map using AFM. It can be seen that the ultrananocrystalline diamond has finer grain size and smaller surface corrugation, which potentially can allow a larger surface contact area with the cells.

Diamond Sample		**Wetting angle θ (°)**	**COOH density (molecules/cm^2)**
H-terminated	**Micro**	90.9 (± 1.0)	-
	Ultranano	88.7 (± 0.9)	-
UV-treated	**Micro**	69.3 (± 1.5)	-
	Ultranano	66.5 (± 1.5)	-
Undecylenic acid	**Micro**	71.0 (± 0.9)	4.8 (± 0.5) $\times 10^{14}$
	Ultranano	77.7 (± 1.1)	6.7 (± 0.5) $\times 10^{14}$

Table 1. Wetting angle of water on different diamond samples and density of the surface carboxylic acid groups determined by the TBO method.

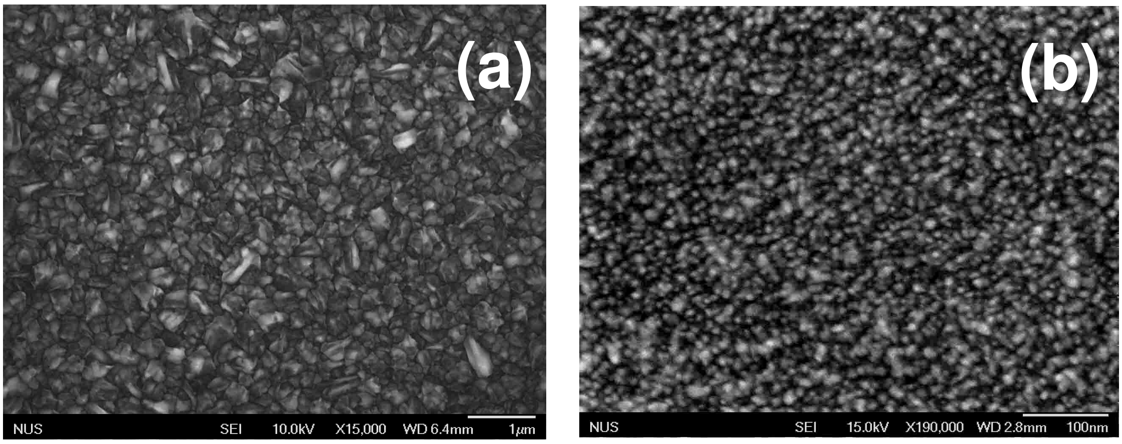

Figure 3.3 SEM micrographs showing the morphology of (a) microcrystalline diamond and (b) ultrananocrystalline diamond.

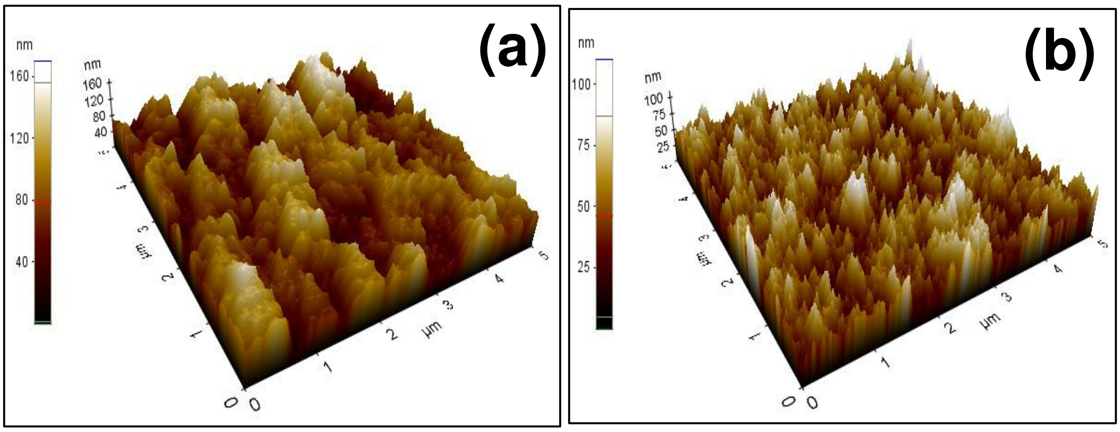

Figure 3.4 AFM images showing the topography of (a) microcrystalline diamond and (b) ultrananocrystalline diamond.

3.3.2 Cell Adhesion Forces

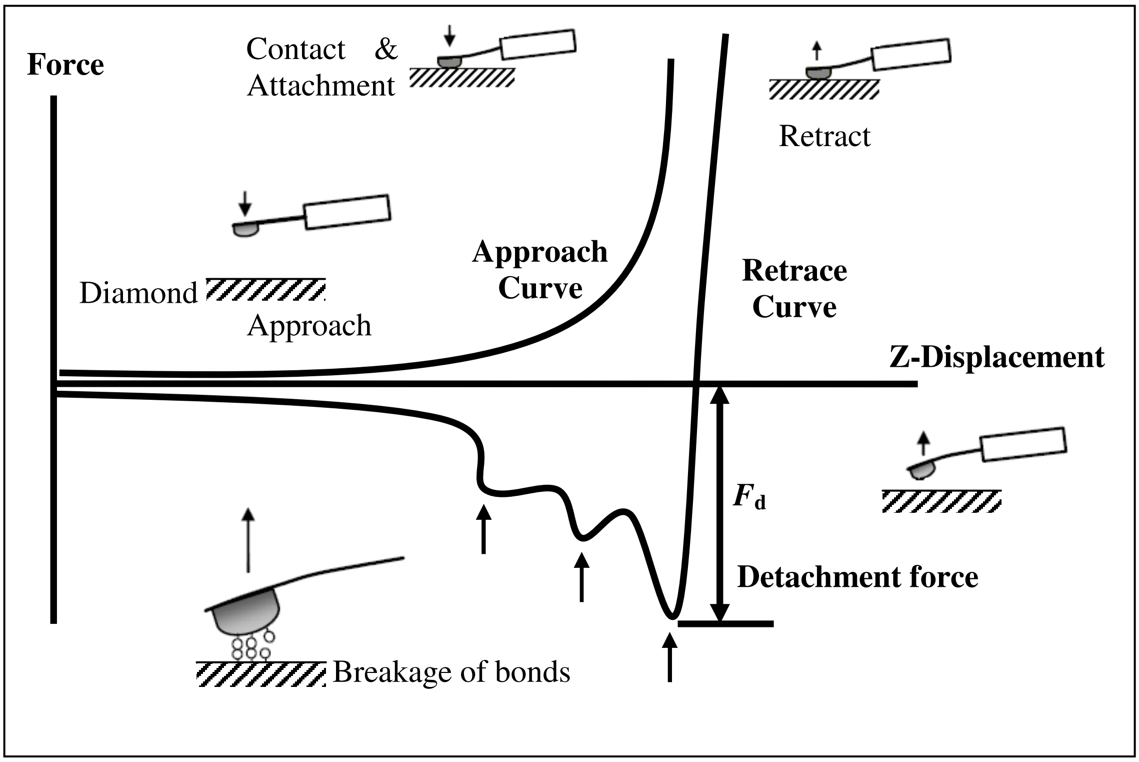

Figure 3.5 Schematic diagram showing typical approach-and-retraction force curve.

Atomic Force Microscopy (AFM) in force mode was used to quantify the initial cell adhesion forces on different diamond surfaces. This is schematically illustrated in Figure 3.5. A single NHDF cell was first attached to a Con A-functionalized cantilever and the cell-cantilever system was lowered onto the sample surface until a predefined contact force (3 nN) was established between the cell and the surface. After a contact time of 200 ms, the cantilever was retracted from the surface at a constant velocity of 2 μm s^{-1} until they were completely separated. On the retraction process, the cantilever was pulled downwards if there were adhesive interactions established between cell and sample surface. Any adhesive interactions formed between cell and the surface ruptured during the retraction process. The sequential rupture of one or more bonds was observed as sharp jumps in the retraction curve and each of these sharp jumps (indicated by arrows under force curve) is considered as a de-adhesion event. The maximal de-adhesion force is represented by the maximum (negative) peak in the retraction curve (F_d, Figure 3.5), which provides a quantitative measurement of cell adhesion force to the surface. The number of de-adhesion events per curve provides an indication of the total number of bond breakages.

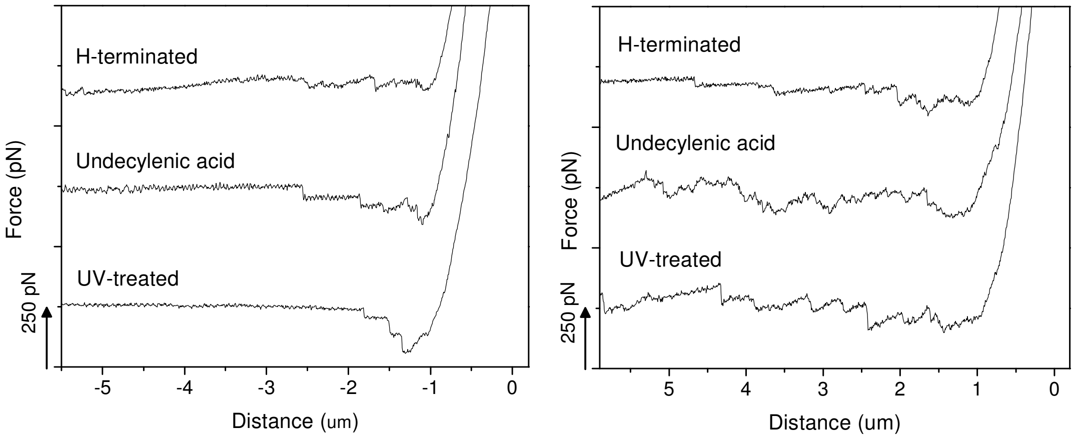

(a)

(b)

Figure 3.6 Force curves between a NHDF cell and (a) microcrystalline and (b) ultrananocrystalline diamond with different modifications.

Figure 3.6 presents the representative force curves between single NHDF cell and the diamond surfaces with different surface treatment. The “sawtooth” profile in the force curves indicate that multiple bond-rupturing processes are involved in the retraction. It is noteworthy that additional de-adhesion forces are needed for complete cellular detachment on UV-treated diamond and UA-functionalized diamond compared with H-terminated diamond. For ultrananocrystalline diamond, the cell underwent multiple de-adhesion events which stretched for a few micrometers before the final separation from the surface (Figure 3.6b). In the case of microcrystalline diamond surfaces, the cell underwent a smaller number of de-adhesion events and became detached from the surface at a shorter distance (Figure 3.6a).

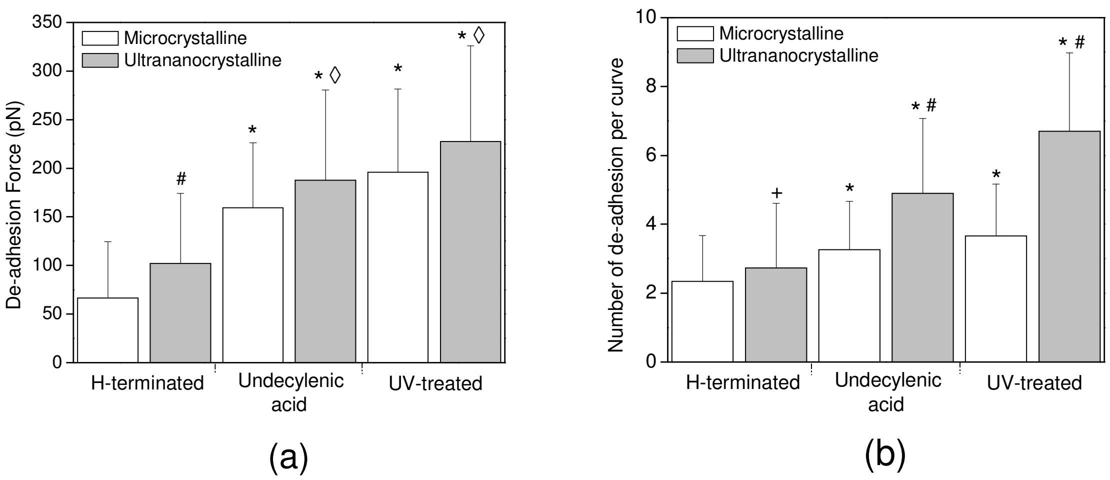

(a) (b)

Figure 3.7 (a) De-adhesion forces and (b) number of de-adhesion events per curve between the NHDF cell and different diamond samples. (In the calculation of the de-adhesion event, peak transition higher than 40 pN with reference to the noise level was calculated as 1 de-adhesion event). Data are presented as mean ± standard deviation of 150 experiments. Differences within samples were tested with Student's t-test: $*P < 0.001$ compared with the respective H-terminated samples (microcrystalline or ultrananocrystalline); $\#P < 0.001$, $\lozenge P < 0.01$, $+P < 0.05$ compared with the microcrystalline diamond samples under same surface treatment (H-termination, undecylenic acid functionalization or UV treatment).

150 force curves for each sample were analyzed in order to arrive at a statistical average. The average value of maximum de-adhesion forces and the number of de-adhesion events per curve are summarized in Figure 3.7. For both microcrystalline and ultrananocrystalline diamond samples the maximum de-adhesion forces were strongest on UV-treated surfaces, followed by UA-functionalized, and these forces were weakest on freshly prepared H-terminated surfaces (Figure 3.7a). On both types of diamond surfaces, UA-functionalization increased the maximum cell de-adhesion forces by about 2-fold and surface treatment with UV irradiation increased the maximum cell de-adhesion forces by about 2.5-fold, compared to the freshly prepared H-terminated surface. Under similar experimental conditions, the maximum de-adhesion forces for all ultrananocrystalline diamond samples were observed to be higher than microcrystalline diamond samples by about 30 pN. Ultrananocrystalline

diamond samples also had a higher number of de-adhesion events per curve compared to the microcrystalline diamond samples (Figure 3.7b). Cell adhesion was observed to be strongest on the UV-treated ultrananocrystalline diamond (227.60 ± 98.68 pN), on average about 8 bonds were formed during the adhesion event. In contrast, cell adhesion was weakest on H-terminated microcrystalline diamond (66.53 ± 58.01 pN), and on average about 2 bonds were formed during the adhesion event. The maximum detachment force can be benchmarked against the forces measured on a fibronectin-coated diamond surface. In this case the adhesion force is mediated by specific binding between the cell-membrane protein and fibronectin, and it was determined to be about 551 pN. Therefore, the cell-adhesion force mediated by non-specific interaction on UV-treated ultrananocrystalline diamond is about 50% of the specific adhesion forces between fibronectin and the same cell.

Cell adhesion on all diamond samples is mediated by the electrostatic interactions or the hydrogen-bond formation between cell-membrane proteins and diamond surfaces. The low de-adhesion forces on H-terminated diamond can be attributed to the hydrophobic characteristics of the surface. Surfaces which have been UV- or UA-treated have a high density of carbonyl or carboxylic acid groups which afford strong electrostatic interactions as well as hydrogen bonding with the cell membrane proteins. The topography of ultrananocrystalline diamond in this case provides higher surface area for the functional groups to interact with cell membrane, albeit non-specifically.

3.3.3 Cell Growth

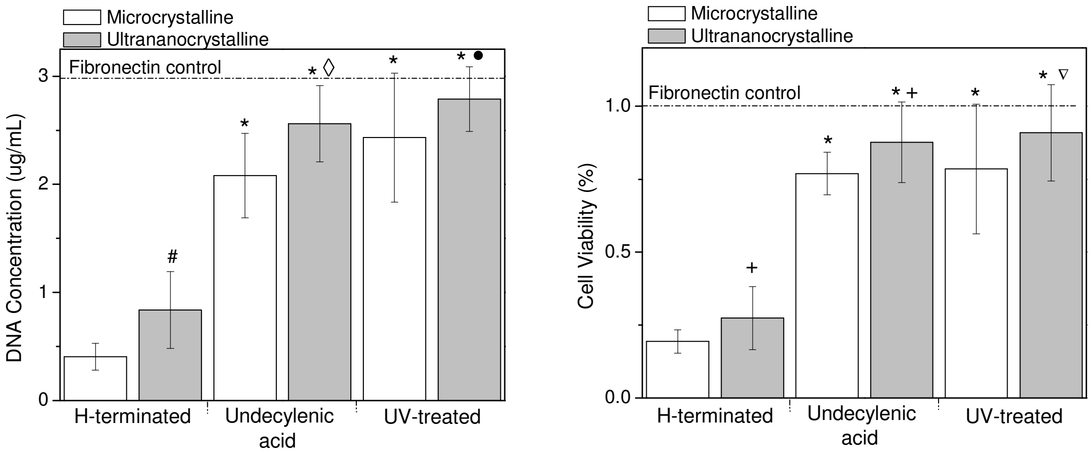

(a) (b)

Figure 3.8 The level of NHDF cell attachment on different diamond samples was estimated from (a) total DNA concentration of cells; (b) cell viability. Data are presented as means ± standard deviation of 12 samples. Differences within samples were tested with Student's t-test: $*P < 0.001$ compared with the respective H-terminated samples (microcrystalline or ultrananocrystalline); $\#P < 0.001$, $\Diamond P < 0.01$, $+P < 0.05$ compared with the microcrystalline diamond samples under same surface treatment (H-termination, undecylenic acid functionalization); $\bullet P > 0.05$ shows there is no significant difference between microcrystalline and ultrananocrystalline diamond samples with UV treatment.

To correlate the initial cell-adhesion forces to the subsequent cell growth, cell culture experiments were carried out on microcrystalline and ultrananocrystalline diamond samples which have been subjected to the same series of surface modifications. NHDF cells were allowed to attach onto the diamond samples and grow for 24 hours, with a fibronectin-coated cover-slip as control. After washing with PBS to remove the loosely attached cells, the NHDF cells were quantified by DNA assay and MTT-ESTA assay and the results are summarized as Figure 3.8.

As shown in Figure 3.8a, the highest cell density could be found on the UV-treated surface, followed by UA-functionalized surface. The lowest cell number was found on the freshly prepared H-terminated surface. For microcrystalline diamond samples, UA functionalization and UV treatment increased the cell density by about

5-fold and 6-fold, respectively, compared to the freshly prepared H-terminated surface. However, the surface treatment using either UV irradiation or UA on ultrananocrystalline diamond increased the cell density by only 3-fold because the original H-terminated ultrananocrystalline diamond surface already had a cell density of 2-fold higher than the H-terminated microcrystalline diamond surface. Therefore intrinsically, ultrananocrystalline diamond is more biocompatible than other diamond surfaces.

Figure 3.8b shows the cell viability studies where the percentages (with respect to a fibronectin-coated surface) of live cells were assayed on different diamond samples. 75% or more cell viability could be observed on UV-treated or UA-functionalized diamond surfaces, whereas only 30% cell viability was observed on H-terminated diamond. Detailed cell morphology can be seen in representative optical micrographs, as shown in Figure 3.9. After surface treatment with UA or UV, NHDF cells spread and developed a spindle-like morphology on the diamond surfaces. This is very similar to the cell morphology on the fibronectin-coated cover-slip, implying good cell attachment and healthy cell growth. However, NHDF cells exhibited a round morphology on the H-terminated diamond surface, an indication of poor cell attachment due to the hydrophobic surface. A Live/Dead Cytotoxicity® Kit from Molecular Probes was used to investigate the cytotoxicity effect of H-terminated treated diamond surfaces after surface treatment. Representative fluorescence micrographs are shown in Figure 3.10, where green fluorescence could be observed from live cells with intact membranes, dead cells with damaged membranes were expected to show red fluorescence. It is clear that all of the cells attached to the diamond surfaces have intact membranes, and that UV-treated diamond showed the highest viable cell count.

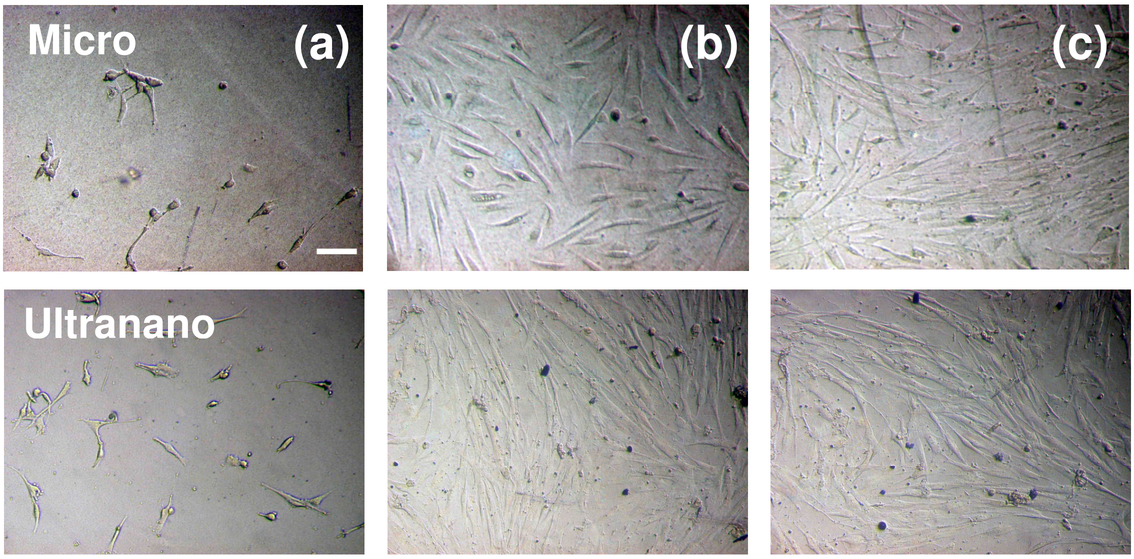

Figure 3.9 Representative optical micrographs (scale bar 150 μm) of NHDF cells after 24h culture on (a) H-terminated, (b) undecylenic acid-functionalized and (c) UV-treated diamond surfaces (top row: microcrystalline; bottom row: ultrananocrystalline).

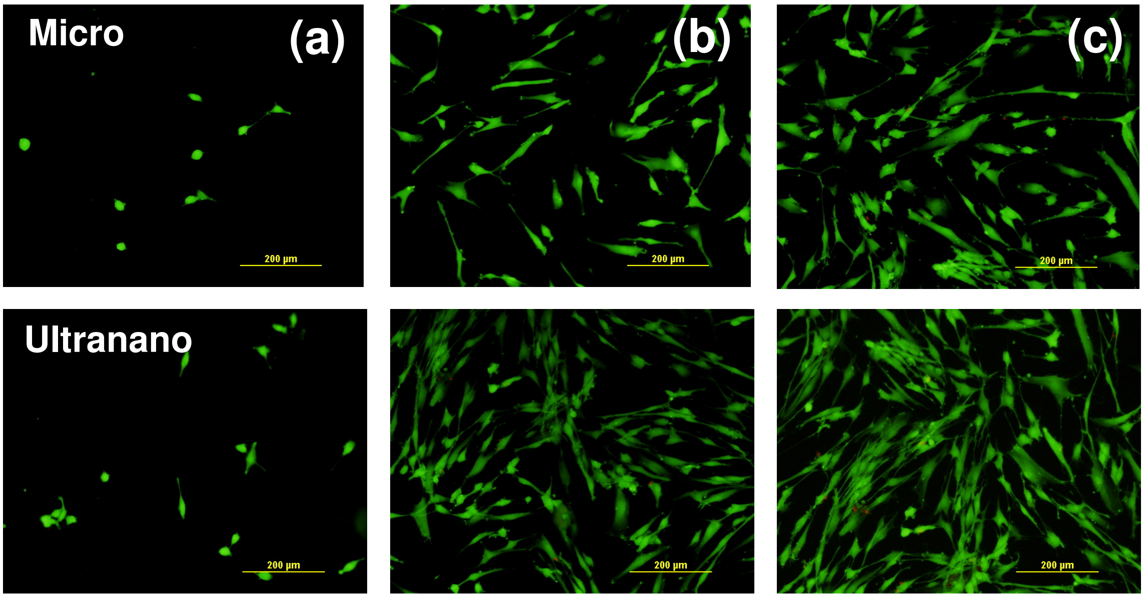

Figure 3.10 Fluorescence micrographs showing NHDF cell attachment on (a) H-terminated, (b) UA-functioanlized and (c) UV-treated diamond surfaces (top row: microcrystalline; bottom row: ultrananocrystalline). The green fluorescence indicates that the cells have intact cell membranes and none of the surfaces are cytotoxic.

3.3.4 Protein Immobilization

In order to explore the possibility of using a diamond surface as a platform for future neuronal cell studies, a protein layer was covalently bonded to the diamond surface to support the neuronal cell growth. The surface carboxylic acid group of the UA-functionalized diamond was activated by 1-ethyl-3-[3-dimethylaminopropyl]carbodiimide hydrochloride / *N*-hydroxysuccinimide (EDC/NHS) to form a stable NHS-ester intermediate. The latter reacts readily with the amine group from the protein to form an amide bond. The protein-coated platform favored the attachment of PC12 cells (Figure 3.11a) because these cells showed affinity only on surfaces coated with the extracellular matrix protein coating. To eliminate the possibility of non-specific binding of protein on to diamond surface, the surface was rinsed copiously with Tween-20. A control experiment involving the incubation of H-terminated diamond with laminin showed no sign of PC12 cell attachment. After attachment of PC12 cells onto the laminin-UA-diamond surface, their ability to differentiate into sympathetic neuron cells was tested by adding nerve growth factor (NGF). It was shown that the PC12 cells were active and able to differentiate into neuron cells on the laminin-UA-diamond surface because numerous neurites extended from the cell body after nerve growth factor (NGF) was added (Figure 3.11b & 3.11c). The ability of functionalized diamond to support the neuronal cell growth will enable it to be a useful platform for neurobiology and neurochemistry studies.

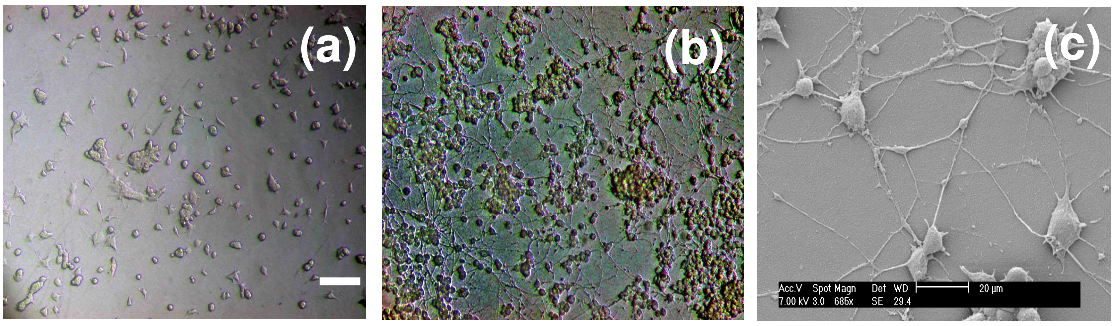

Figure 3.11 Morphologies of PC12 cells on laminin-UA-functionalized diamond surface after (a) 12h culture in the absence of NGF; (b) 72h culture in the presence of NGF. (Scale bar 150 µm) and (c) SEM showing neurite extensions from PC12 cells after 72h culture in the presence of NGF.

3.3.5 Cell Gradient Formation

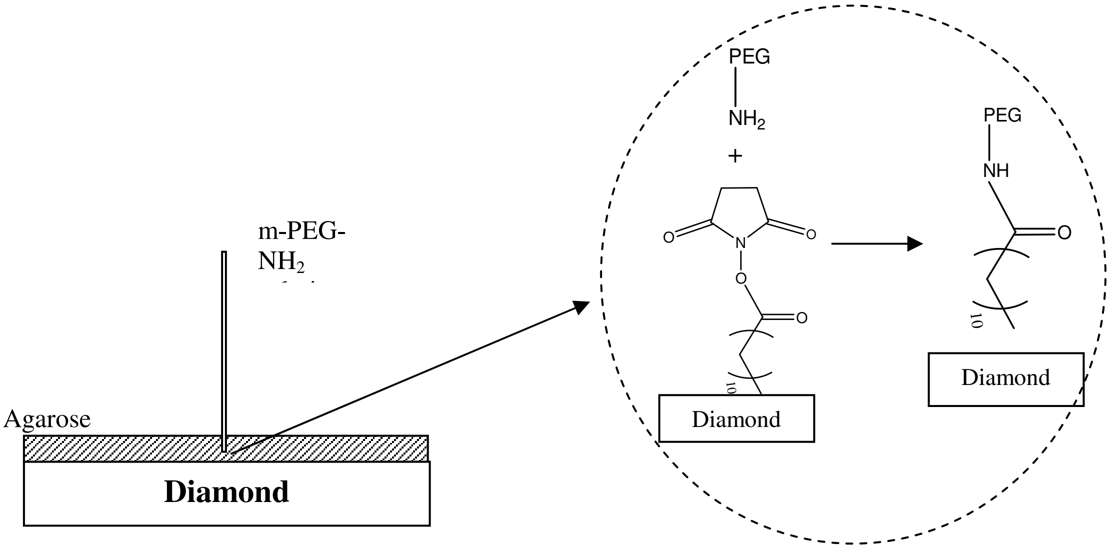

Figure 3.12 Schematic diagram showing the construction of PEG surface gradient by gel diffusion method.

The surface carboxylic acid group of UA-functionalized diamond was activated as described above to form a stable NHS-ester intermediate. This intermediate reacted readily with the amine group from m-PEG-NH_2. A syringe containing m-PEG-NH_2 served as a point source to deliver active PEG through the agarose gel, creating a diffusion gradient of PEG within the gel, as shown by the schematic diagram in Figure 3.12. The region directly beneath the point source had a higher concentration of PEG and this concentration decreased with distance from the point source. PEG is well known for its ability to reduce nonspecific adsorption of proteins and cells. The surface gradient of PEG coverage on diamond was subsequently used for cell gradient formation. NHDF cells at 1.5 × 10^5 cells/mL were seeded on to the PEG-gradient diamond surface and allowed to attach for 24 h. A series of optical micrographs in Figure 3.13 show the attachment of NHDF cells at different positions along the PEG gradient. Due to the greater cell inhibition at the regions of higher PEG concentration, a cell gradient was established following the diffusion profile of PEG and the cell density was higher at the position farther away from the point source. Therefore, the controlled diffusion of PEG on UA-functionalized diamond allows us to establish a cell gradient on diamond, which can serve as an experimental platform for investigating combinatorial cellular chemistry.

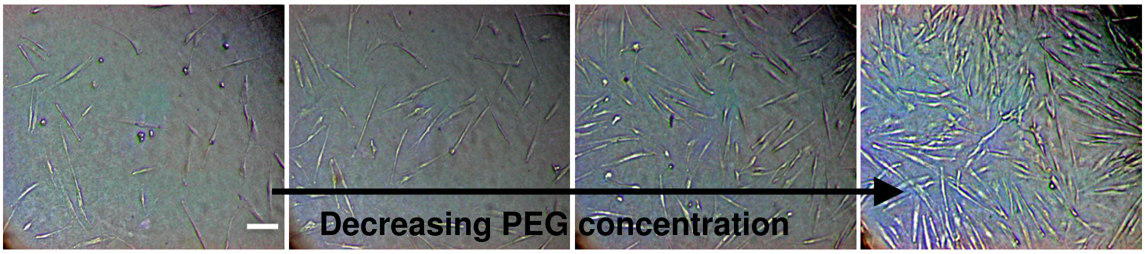

Figure 3.13 Micrographs showing attachment of NHDF cells on a surface gradient of PEG, from left to right at 0 mm, 4 mm, 8 mm and 12 mm from PEG point source, respectively (scale bar 150 µm).

3.4 Conclusions

The adhesion characteristics of NHDF cells on diamond surfaces with different surface topography and chemistry have been analyzed quantitatively using biochemical assays and atomic force microscopy. UV irradiation of diamond surfaces in air was found to be effective for surface oxygenation and such oxygenated surfaces are hydrophilic and provide a better platform for initial cell adhesion and subsequent cell growth compared to a H-terminated surface. Photochemical coupling of undecylenic acid (UA) onto diamond surfaces also imparts equivalent biocompatible properties, although our study shows that UV-irradiation provides a more convenient and effective route for promoting cell attachment and cell growth. The maximum detachment force (227 pN) of a NHDF cell from UV-treated ultrananocrystalline diamond was measured to be about 50% of that of the specific binding force (551 pN) between fibronectin and the cell membrane, and about 3.5 times larger than the detachment force on hydrogenated diamond (66 pN). Therefore, the term "biocompatibility" of diamond surfaces refers to oxygenated diamond surfaces. It was also verified that ultrananocrystalline diamond exhibits better performance than microcrystalline diamond in terms of cell attachment and cell growth. UA-treated diamond surfaces, however, are amenable to further functionalization with biomolecules. By utilizing the surface carboxylic acid group of UA-functionalized diamond, an active protein layer supporting neuronal cells growth can be constructed on the diamond surface. Finally, the formation of a cell gradient was achieved by establishing a diffusion gradient of polyethylene glycol on UA-functionalized diamond.

References

---

[1] Kawarada, H. *Surf. Sci. Rep.*, **1996**, 26, 205.

[2] Yang, W.; Auciello, O.; Butler, J. E.; Cai, W.; Carlisle, J. A.; Gerbi, J. E.; Gruen, D. M.; Knickerbocker, T.; Lasseter, T. L.; Russell, J. N. Jr.; Smith, L. M; Hamers, R. J. *Nat. Mat.*, **2002**, 1, 253.

[3] Wenmackers, S. ; Christiaens, P. ; Daenen, M. ; Haenen, K.; Nesladek, M.; van deVen, M.; Vermeeren, V.; Michiels, L.; Ameloot, M.; Wagner, P. *Phys. Stat. Sol. A*, **2005**, 202, 2212.

[4] Specht, C. G.; WIllians, O.A.; Jackman, R. B.; Schoepfer, *Biomaterials*, **2004**, 25, 4073.

[5] Ariano, P; Baldelli, P.; Carbone, E.; Gilardino, A.; Lo Giudice, A.; Lovisolo, D.; Manfredotti, C.; Novara, M.; Sternschulte, H.; Vittone, E. *Diamond and Related Materials*, **2005**, 14, 669.

[6] Lee, H. B.; Lee, J. H.; Jung, H. W.; Kang, I. *Biomaterials*, **1994**, 5, 9.

[7] Whitesides, G. M.; López, G. P.; Albers, M. W.; Schreiber, S. L.; Carroll, R.; Peralta, E. *J. Am. Chem. Soc.*, **1993**, 115, 5877.

[8] Teixeira, A. I.; Abrams, G. A.; Bertics, P. J.; Murphy, C. J.; Nealey, P. F. *J.Cell Sci.,***2003**, 116, 1881.

[9] Shirato, I.; Tomino. Y.; Koide, H.; Sakai, T. *Cell Tissue Res.* **1991**, 266, 1.

[10] Hyonchol, K. ; Arakawa, H. ; Osada, T. ; Ikai, A. *Colloids and Surface B: Biointerfaces*, **2002**, 25, 33.

[11] Benoit, M. ; Gabriel, D. ; Gerisch, G. ; Gaub, H. E. *Nat. Cell. Biology*, **2000**, 2, 313.

[12] Florin, E,-L; Moy, V. T. ; Gaub, H. E. *Science* **1994**, 264, 415

[13] Dammer, U.; Hegner, M.; Anselmetti, D.; Wagner, P.; Dreier, M.; Huber, W.; Güntherodt, H.-J. *Biophys. J.*, **1996**, 70, 2437.

[14] Rezek, B.; Shin, D.; Nakamura, T.; Nebel, C. E. J. Am. Chem. Soc. **2006**, 128, 3884.

[15] Zhong, Y. L.; Chong, K. F.; May, Paul; Chen, Z. K.; Loh, K. P. *Langmuir*, **2007**, 23, 5824.

[16] Ealey, P. A.; Yaterman, M. E.; Holt, S. J.; Marshall, N. J. *J. Mol. Endocrinol.*, **1988**, 1, 1.

[17] Liedberg, B.; Tengvall, P. *Langmuir*, **1995**, 11, 3821

Chapter 4. Whole-Cell Environmental Biosensor on Diamond

A whole-cell environmental biosensor was a fabricated on a diamond electrode surface. Unicellular microalgae *Chlorella vulgaris* was entrapped in a bovine serum albumin (BSA) membrane and immobilized directly onto the surface of a diamond electrode for heavy-metal detection. We found that the unique surface properties of diamond reduce the electrode-fouling problem commonly encountered with metal electrodes and impart higher detection sensitivity as well as long-term stability (storage up to 14 days and 20 repetitive scan times). The detection limits of the diamond biosensor at 0.1 ppb for cadmium ions and zinc ions conform to the drinking water standard set by the US.

4.1 Introduction

The past decade witnessed the rapid dwindling of fresh water sources in developing countries due to contamination by various toxic compounds such as heavy metals and pesticides, as well as problems caused by deforestation and climate changes. Accompanying these changes, there are ongoing efforts to develop water monitoring systems that are portable and which can show rapid, sensitive response to a wide range of toxins. Biosensors have received much attention in water-monitoring systems owing to their high sensitivity, low cost and easy adaptation for on-line monitoring[1,2]. Whole cell micro-organisms appear to be attractive candidates as they host a large number of enzymes and bioreceptors which can be very sensitive to toxic compounds. The green alga *Chlorella vulgaris* has been used in constructing optical[3,4], electrochemical[5] and conductometric[6] biosensors for environment monitoring. *C. vulgaris* is an ideal choice for a biosensing element because it is ubiquitous and grows year-round in all climatic conditions. Its wide availability in nature, simple cell structure and ability to acclimatize to low nutrient levels make it an excellent choice as a biological sensing material. Phosphatase enzyme is one of the enzymes which can be found abundantly in the *C. vulgaris* cell wall. Under alkaline conditions, phosphatase enzyme activity, known also as alkaline phosphatase activity (APA), will be inhibited by toxins such as heavy-metal ions. APA dephosphorylates the substrate *p*-nitrophenyl phosphate into *p*-nitrophenol and phosphate ions. Chouteau *et. al.* developed a conductometric biosensor based on the inhibition of APA in the presence of heavy-metal ions[6]. Marks *et. al.* developed an electrochemical biosensor based on *C. vulgaris* immobilized on a platinum electrode, and the APA was monitored by the oxidation current of enzymatically generated pnitrophenol[5]. However, we found that long term usage of this biosensor is precluded by the problem of electrode fouling.

To develop long-term stability, diamond was evaluated as the candidate platform sensing material in this work. Diamond possesses outstanding electrochemical characteristics, such as a wide potential window[7,8,9], low background current[10,11], weak adsorption for organic molecules[12,13] and high stability of response.[14,15]. Therefore, diamond electrodes are a suitable material for several purposes: synthesis of chemicals, electroanalysis[9], energy conversion and destruction of organic/inorganic pollutants[16]. Moreover, the versatility of these materials has also been extended to develop sensors and biosensors[9,17]. However, the growth conditions for alga cells on diamond, as well as the condition for stable and leach-free entrapment of these cells on diamond, are unknown. Therefore, we investigate the immobilization of alga cells on diamond, and investigate the parameters that allow sensitive detection of heavy metals. Comparative studies on sensitivity and resistance to electrode fouling, as well as heavy-metal detection, were also carried out for diamond and platinum electrodes.

4.2 Experimental Section

4.2.1 Chemicals

All the chemicals used in this experiment were purchased from Sigma Aldrich unless otherwise stated and were used as received.

4.2.2 Diamond Electrode Preparation

The boron-doped diamond electrode was grown on a 35 mm diameter niobium disk using conventional CH_4/H_2/diborane chemistry, with a 2.45 GHz commercial microwave chemical vapor deposition (CVD) system. Diamond samples were cleaned and chemically oxidized with hot 'Piranha' solution (30% H_2O_2 : 97% H_2SO_4 = 1 : 3) for 1 hour, followed by rinsing with ultrapure water. The samples were then rinsed with tetrahydrofuran followed by hexane. Cleaned diamond samples were hydrogen-terminated by hydrogen plasma treatment at 800 W in a microwave plasma CVD system under 300 sccm hydrogen gas flow for 15 min.

4.2.3 Algae Culture Condition

The algae *C. vulgaris* strain was purchased from the Culture Collection of Algae and Protozoa (CCAP) at Cumbria, UK. The algae was cultured in the inorganic defined medium and sub-cultured every three weeks. In order to induce maximal enzyme alkaline phosphatase activity (APA), the algae were centrifuged and suspended in a phosphate-free medium for 25 days before being immobilized on the diamond electrode surface[18].

4.2.4 Diamond Biosensor Preparation

The algae were immobilized on the diamond electrode surface by using bovine serum albumin (BSA) and glutaraldehdye as the crosslinker[19]. 100 µL of starved algae solution and 10 % (w/v) BSA were mixed and deposited onto the diamond electrode surface. Finally, the electrode was placed in the saturated glutaraldehyde vapor for 20 minutes and dried at room temperature for 30 minutes. The electrode surface area was 0.0962 cm^2.

4.2.5 Fluorescence Observation

A fluorescence micrograph of the algae/BSA membrane after immobilization on the diamond electrode was observed with a fluorescence microscope (Olympus BX60) equipped with a rhodamine B filter (excitation: 540 nm; emission: 625 nm).

4.2.6 Electrochemical Instrumentation

All electrochemical experiments in this work were accomplished using Autolab/PGSTAT30, Eco Chemie B.V. with a platinum wire and a saturated Ag/AgCl electrode as a counter and a reference electrode, respectively.

4.2.7 Cyclic Voltammetry and Chronoamperometric

The electrochemical behavior of the algae-BSA-membrane-coated diamond electrode was investigated by cyclic voltammetry in the presence of 0.5 mM ferrocene carboxylic acid solubilized in 0.1 M tris-HCl containing 1 mM $MgCl_2$. For chronoamperometry, the algae-coated diamond electrode was immersed in 0.1 M tris-HCl (with 1 mM $MgCl_2$ as enzyme activator) solution. The electrode was potentiostated at 1.2 V and the susbstrate *p*-nitrophenyl phosphate was added into the solution with constant stirring (100 rpm). The resulting current from the oxidation of enzymatically generated *p*-nitrophenol was recorded.

4.2.8 Heavy-Metal Testing

Two heavy metals, namely cadmium and zinc ions (with nitrate as anion), were used in this work.

4.3 Results and Discussions

4.3.1 Membrane Permeability

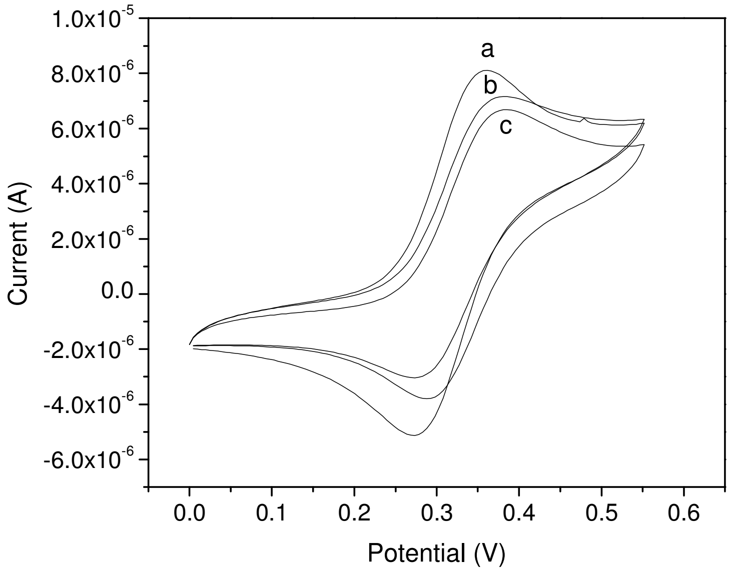

Figure 4.1 Cyclic voltammograms of diamond in a ferrocene carboxylic acid solution (a) before algae-BSA coating and (b) after algae-BSA coating (c) after soaking (b) overnight in buffer solution. The small current decrease after BSA coating and overnight soaking shows good permeability and stability.

The permeability of an algae-BSA membrane on a diamond electrode was investigated by cyclic voltammetry in a buffer solution containing ferrocene carboxylic acid. The steric hindrance generated by this membrane was monitored by the one-electron oxidation of ferrocene by the diamond electrode. Cyclic voltammograms recorded at the diamond electrode prior to and after the algae-BSA-membrane coating are shown in Figure 4.1. The algae-BSA-membrane coating imposed only a slight degree of steric hindrance to the heterogeneous electron transfer of ferrocene carboxylic acid with the underlying diamond electrode, as can be judged by the small current decrease in the reversible peaks, i.e. the anodic peak is decreased from 8.1 μA to 6.9 μA after the coating. The small current decrease demonstrates the good permeability of the BSA membrane and indicates that it is a good candidate in this biosensor design. The stability of the membrane was confirmed by soaking the algae-BSA-coated diamond electrode in the buffer solution overnight, and the result shows (Figure 4.1c) that the current density remained unchanged with no visible change in the membrane appearance.

4.3.2 Algae Viability

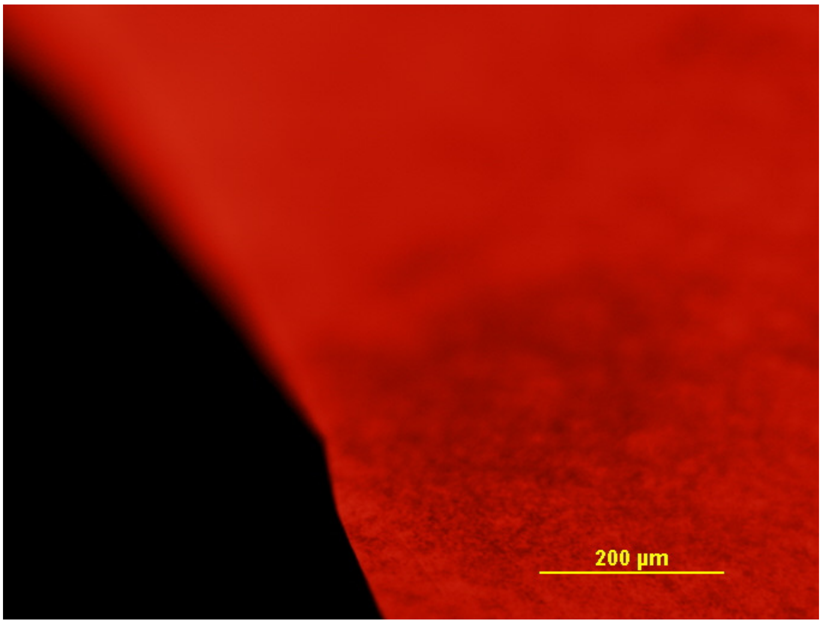

Figure 4.2 Fluorescence image of algae/BSA membrane. Photosystem II (PS II) fluorescence emission indicates the algae remain viable after BSA entrapment.

Fluorescence observation of the algae/BSA membrane was done with filter at 540 nm for excitation and 625 nm for emission. This excitation wavelength lies close to the Soret band maximum absorption of chlorophyll b in algae[20] whereas the emission wavelength corresponds to the Photosystem II (PS II) fluorescence emission peak in algae[21]. From Figure 4.2, red fluorescence can be seen from the algae/BSA membrane, indicating that most of the green algae remain in the viable state.

4.3.3 Alkaline Phosphatase Activity Detection

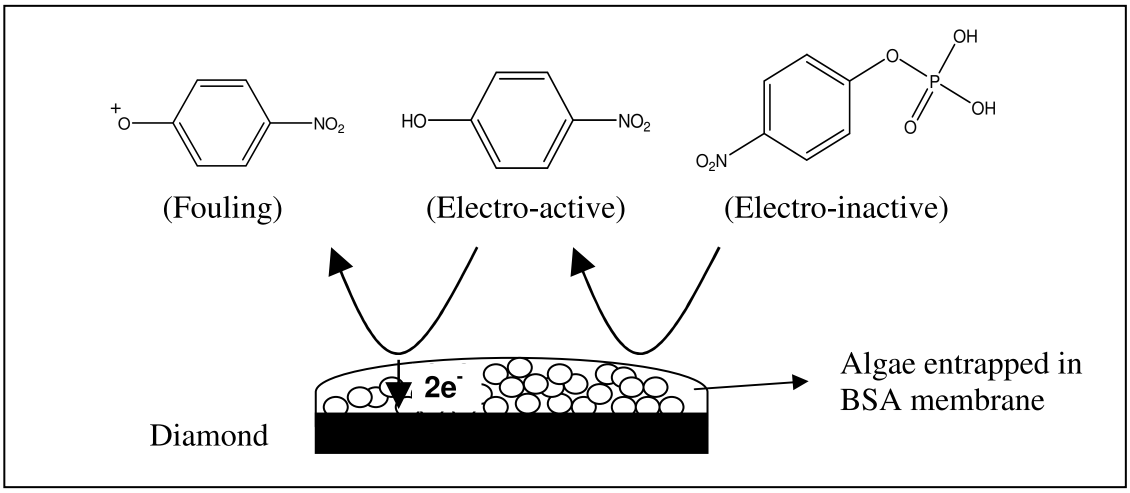

Figure 4.3 Detection principle for a diamond biosensor. The electro-inactive substrate *p*-nitrophenyl phosphate will be dephosphorylated by enzyme alkaline phosphatase at the algae membrane to produce electro-active *p*-nitrophenol, and it will be subsequently oxidized at the diamond electrode. The oxidation of *p*-nitrophenol will create electrode fouling problem at other metal electrodes.

The principle of this diamond biosensor is based on the dephosphorylation properties of the enzyme alkaline phosphatase which can be found abundantly in the algae membrane, as schematically depicted in Figure 4.3. The added *p*-nitrophenyl phosphate, which is electro-inactive, will act as the substrate for this enzymatic action and the product *p*-nitrophenol, which is electro-active will be generated. Thus, chronoamperometry experiment monitors the oxidation current of *p*-nitrophenol.

The density of the immobilized cells has to be controlled to optimize the amount of enzyme loading on the electrode. On the other hand, overloading the diamond platform with cells will passivate the electrical response of the diamond and block the diffusion of analytes to the diamond surface. The oxidation current response of different algae-concentration loading in the presence of excess substrate (0.5 mM) is shown in Figure 4.4a. It shows clearly that the optimum cell density can be obtained at 5 x 10^7 cells/mL, where the highest oxidation current is obtained. The optimum pH for this diamond biosensor is also investigated and shown in Figure 4.4b. It was found that the optimum pH for the enzyme alkaline phosphatase activity is at pH 9 as it gives the highest current response in the presence of excess substrate.

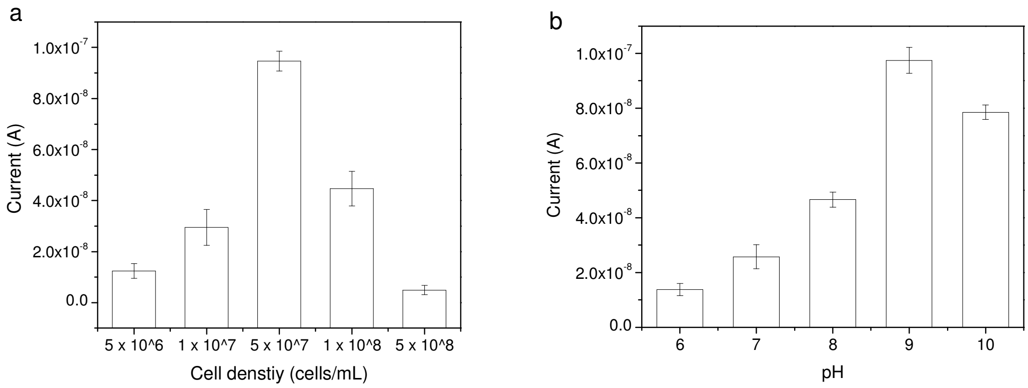

Figure 4.4 Current response of (a) different algae concentrations immobilized on a diamond surface (b) diamond biosensors in different pH solution in the excess of substrate concentration (0.5mM). The optimum condition for diamond biosensor can be obtained at 5 x 10^7 cells/mL and pH 9.

Having identified the optimum conditions for the experiment (5 × 10^7 cells/mL; pH 9), the analytical performance of the diamond biosensor was investigated. Figure 4.5 shows the calibration curves for substrate *p*-nitrophenyl phosphate when diamond and platinum were used as electrode materials. The sensitivity was 8.03 mA M^{-1} cm^{-2} and 4.03 mA M^{-1} cm^{-2} for diamond and platinum electrodes, respectively. Algae immobilized on diamond electrodes exhibited higher sensitivity compared to those on the platinum electrodes: each addition of substrate into the solution containing the diamond biosensor generated an oxidation current which was about two times higher than the platinum biosensor before all of the enzymatic sites were saturated. It can be noted that for the diamond biosensor, the oxidation current reached saturation at a lower substrate concentration (0.125 mM) compared to the platinum biosensor (0.2 mM).

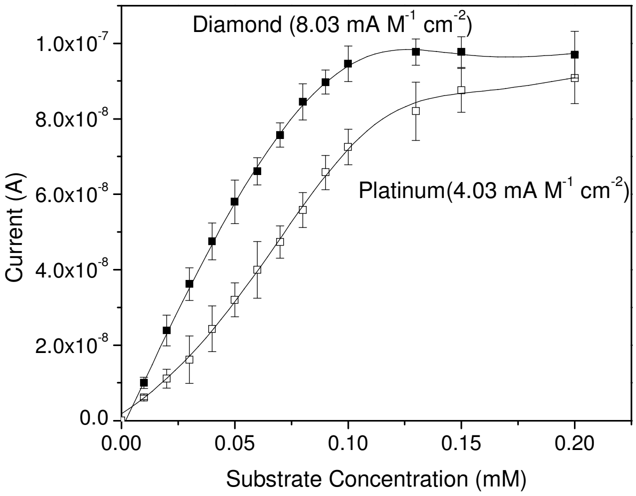

Figure 4.5 Substrate calibration curve for algae immobilized on diamond and platinum surface. Algae immobilized on diamond surfaces shows higher sensitivity as compared to platinum surfaces.

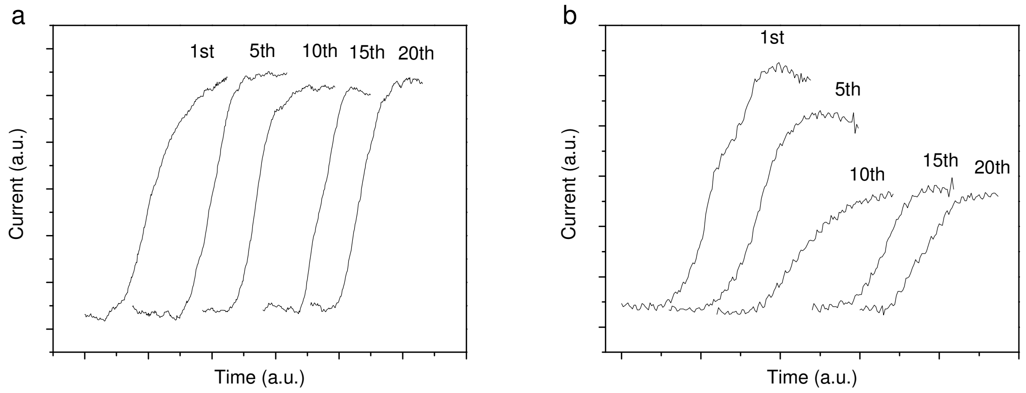

Figure 4.6 Chronoamperometry current response for (a) diamond biosensor and (b) platinum biosensor after different scan times in excess of substrate (0.5 mM). The oxidation current for the diamond biosensor remains stable even after 20 scan times.

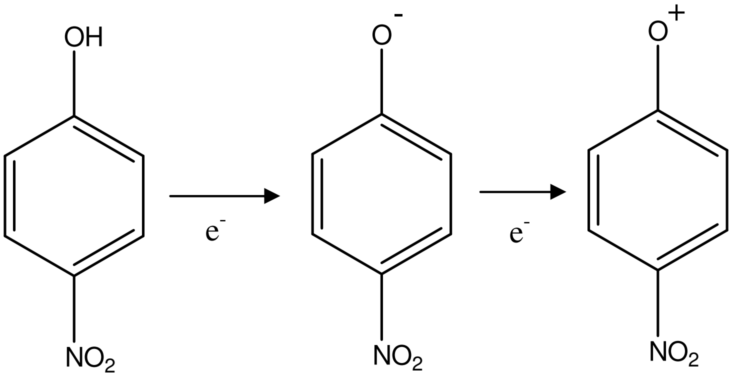

Equation 4.1 Oxidation of *p*-nitrophenol to nitrophenoxy radical and subsequently to nitrophenoxy cation.

The biofouling resistance of the diamond biosensor was further evaluated by monitoring the current response continuously after repetitive usage in the presence of excess substrate (0.5 mM). Figure 4.6 clearly shows that the oxidation current remained stable on the diamond biosensor compared to that on the platinum biosensor after 20 scans. The resistance to fouling on both electrodes after 20 scans is summarized in Figure 4.7. It can be observed that the current only fluctuates within

10% of the initial oxidation current throughout on diamond, compared to a decrease of more than 40% on the Pt electrode. A previous report by Rodrigo[22] shows that continuous oxidation of *p*-nitrophenol will generate *p*-nitrophenoxy radicals will be oxidized subsequently to the nitrophenoxy cation, as shown in Equation 4.1. The nitrophenoxy cation is very reactive and has a tendency to polymerize and foul the electrode surface. The diamond surface is chemically inert and exhibits good fouling resistance, due possibly to the hydrophobic, hydrogen-terminated surface[23] compared to the more hydrophilic metal electrode surfaces. In order to evaluate the long-term stability, the diamond and Pt biosensors were stored in the phosphate-free medium and tested over a period of 14 days in excess substrate (0.5 mM). As shown in Figure 4.8, the diamond biosensor exhibited excellent long-term stability with current fluctuation within 10% of the initial oxidation current, but the platinum biosensor was found to be unstable, the current response dropped to 60% of the initial oxidation current at the end of 14 days.

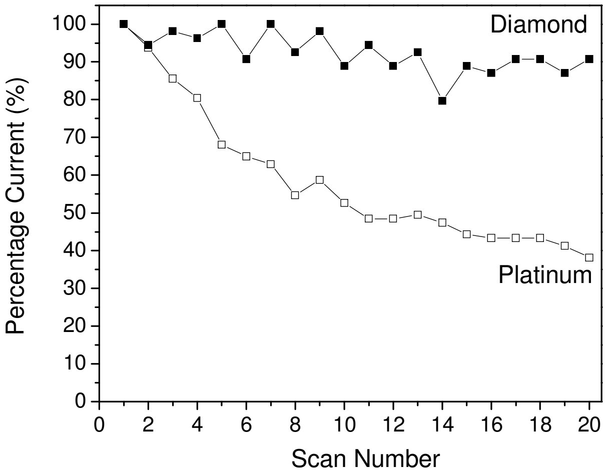

Figure 4.7 Bio-fouling resistance of diamond and platinum after repetitive usage in excess of substrate (0.5 mM). Within 20 scan times, the oxidation current of the diamond biosensor only fluctuated ~ 10% whereas the platinum biosensor showed a current decrease of about 40%.

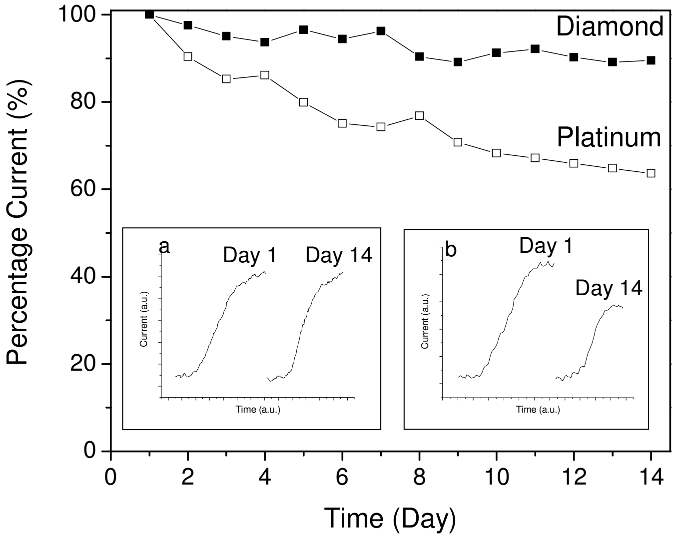

Figure 4.8 Stability test for the diamond biosensor and platinum biosensor for 14 days. Insets show the chronoamperometry current response at day 1 and day 14 for (a) diamond biosensor (b) platinum biosensor. The diamond biosensor remained stable after 14 days of storage and repetitive scans.

4.3.4 Heavy-Metal Detection

The diamond biosensor was subsequently used for the detection of two heavy metals, namely cadmium and zinc. It is known that the enzymatic activity of alkaline phosphatase will be inhibited in the presence of heavy metals. The inhibition of the enzymatic activity will be reduced, decreasing *p*-nitrophenol production and subsequently lead to a lower oxidation current. This principle will be applied here for the diamond biosensor in detecting trace heavy metals.

The diamond biosensor was exposed to the heavy-metal solution for 5 minutes before excess substrate (0.3 mM) was added into the solution. The results were summarized in Figure 4.9. For both heavy metals, it can be noted that the oxidation current decreased linearly with increasing concentration of heavy metals. The activity of the enzyme alkaline phosphatase was inhibited at high concentration of cadmium ions (10 mM) and zinc ions (100 mM). A slight increase in oxidation current was observed for low concentrations of heavy metals (for cadmium < 10 mM; zinc < 100 mM). This is attributed to the slight activation of the enzyme at low concentrations of heavy metals due to cellular stress, where stress promoters are produced to increase the enzyme activity[24]. Detection limits for the diamond biosensor was 0.1 ppb for both cadmium and zinc ions, which is well above the contamination level for heavy metals set by the US for drinking water (5 ppb for cadmium and 5 ppm for zinc). Though an antibody-based biosensor made by Blake *et. al.*[25] showed a better detection limit for cadmium ions (30 ppt), this result presents a better detection limit as compared to other types of *Chlorella vulgaris*-entrapped biosensors, such as a *Chlorella vulgaris* optical biosensor[26] (10 ppb detection limit for cadmium) and a *Chlorella vulgaris* conductometric biosensor[27] (10 ppb detection limit for cadmium).

The resistance to *p*-nitrophenol oxidation fouling shown by the diamond electrode enables it to be used as a sensitive, long-term and stable water-monitoring biosensor. In order to implement it as an on-site monitoring system, improvement has to be done as we observed that the re-activation of the enzyme was not possible after heavy-metal exposure.

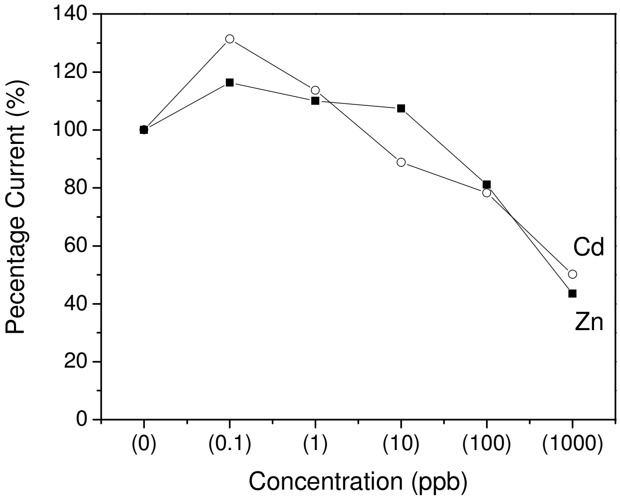

Figure 4.9 Heavy-metal detection on the diamond biosensor. The oxidation current decreases linearly with increasing concentration of heavy metals with a detection limit of 0.1 ppb.

4.4 Conclusions

This chapter demonstrated the suitability of diamond to be used as the signal transduction platform for algae cells owing to its excellent property of resisting electrode fouling by *p*-nitrophenol oxidation. The conditions for optimizing algae cell density on the BSA-membrane-diamond platform have been identified. Comparative studies on a Pt electrode showed that diamond is more resistant to electrode fouling, and also shows better long-term stability. The detection limit for cadmium and zinc ions is 0.1 ppb.

References

---

[1] Rogers, K. R. *Biosens. Bioelectron.* **1995**, 10, 533.

[2] Dennison, M. J.; Turner, A. P. F. *Biotechnol. Adv.* **1995**, 13, 1.

[3] Vedrine, C. ; Leclerc, J. C. ; Durrieu, C. ; Tran-Minh, C. *Biosens. Bioelectron.* **2003**, 18, 457.

[4] Rodriguez, M. Jr.; Sanders, C. A.; Greenbaum, E. *Biosens. Bioelectron.* **2002**, 17, 843.

[5] Ionescu, R. E. ; Abu-Rabeah, K.; Cosnier, S.; Durrieu, C. ; Chovelon, J. M. ; Marks, R. S. *Electroanalysis* **2006**, 18, 1041.

[6] Chouteau, C.; Dzyadevych, S.; Chovelon, J. M. ; Durrieu, C. *Biosens. Bioelectron.* **2004**, 19, 1089.

[7] Strojek, J. W.; Granger, M. C.; Dallas, T.; Holtz, M. W.; Swain, G. M. *Anal. Chem.* **1996**, 68, 2031.

[8] Xu, J.; Swain, G. M. *Anal. Chem.* **1998**, 70, 1502.

[9] Chailapakul, O.; Siangproh, W.; Tryk, D. A. *Sensor Lett.* **2006**, 99.

[10] Yano, Y.; Tryk, D. A.; Hashimoto, K.; Fujishima, A. *J. Electrochem. Soc.* **1998**, 145, 1870.

[11] Kraft, A. *Int. J. Electrochem. Sci.* **2007**, 2, 355.

[12] Vinokur, N.; Miller, B.; Avyigal, Y.; Kalisk, R. *J. Electrochem. Soc.* **1996**, 143, L238.

[13] Alfaro, M. A.; Ferro, S.; Martinez-Huitle, C. A.; Vong, Y. M. *J.Braz. Chem.Soc.***2006**, 17, 227.

[14] Rao, T. N.; Yagi, Y.; Miwa, T.; Tryk, D. A.; Fujishima, A. *Anal. Chem.* **1999**, 71, 2506.

[15] Popa, E.; Notsu, H.; Miwa, T.; Tryk, D. A.; Fujishima, A. *Electrochem. Solid-State Lett.* **1999**, 2, 49.

[16] Martínez-Huitle, C. A.; Ferro, S. *Chem. Soc. Rev.* **2006**, 35, 1324.

[17] Carlisle, J. A. *Nature Materials*, **2004**, 3, 668.

[18] Fitzgerald, G. P.; Nelson, T.C. *J. Phycol.* **1966**, 2, 32.

[19] Babu, P. S. R.; Panda, T. *Enzyme Microb. Technol.* **13**, 8, 676.

[20] Hipkins, M. F.; Baker, N. R. *Photosynthesis Energy Transduction. A Practical Approach.* Irl Press, Oxford, **1986**, 51-101.

---

[21] Govindjee; Amesz, J.; Fork, D. C. *Light Emission by Plants and Bacteria*. Academic Press, Orlando, **1986**, 497-537.

[22] Canizares, P.; Saez, C.; Lobato, J.; Rodrigo, M. A. *Ind.Eng. Chem. Res.* **2004**, 43, 1944.

[23] Tryk, D. A.; Tachibana, H.; Inoue, H.; Fujishima, A. *Diamond and Related Materials* **2007**, 16, 881.

[24] Mazorra, M. T.; Rubio, J. A.; Blasco, J. *Comp. Biochem. Physiol. B* **2002**, 131, 241.

[25] Blake, D. A.; Jones, R. M.; Blake II, R. C.; Pavlov, A. R.; Darwish, I. A.; Yu, H. *Biosens. Bioelectron.* **2001**, 16, 799.

[26] Durrieu, C.; Tran-Minh, C. *Ecotoxicol. Environ. Safe* **2002**, 51, 206.

[27] Chouteau, C.; Dzyadevych, S.; Durrieu, C.; Chovelon, J. M. *Biosens. Bioelectron.* **2005**, 21, 273.

Chapter 5. Stripping Voltammetry of Lead at Bacteria-modified Boron-doped Diamond Electrodes

The wide electrochemical potential window of CVD diamond allows the cathodic detection of Pb^{2+} ions at voltages that lie outside the electrochemical potential window of conventional metal electrodes. The immobilization of bacteria cells, *Acidithiobacilllus ferrooxidans*, on the surface of diamond enhances the detection limit for Pb^{2+} ions by two fold, which is 10 µM. The bacteria-modified diamond electrode provides a linear detection range for Pb^{2+} from 10 µM up to 200 µM and higher sensitivity within the linear range. The unique property of *Acidithiobacilllus ferrooxidans* in fixing metal ions within its membrane provides the preconcentration effect needed in stripping voltammetry.

5.1 Introduction

Boron-doped diamond is an attractive candidate for electroanalysis owing to its wide electrochemical window[1], low background current[2], chemical inertness[3] and high stability.[4] Fujishima *et. al.* demonstrated the use of diamond electrodes in the stripping voltammetry of metal ions[5]. In stripping voltammetry, the electrode is initially held at a fixed potential in order to electrochemically deposit the analyte of interest onto the electrode surface. This is also known as the preconcentration step. The electrode will be then scanned either anodically or cathodically in order to liberate the analyte as an ion from the electrode. This step results in a faradaic current flow which can be used for the direct quantification for the analyte. Traditionally, stripping voltammetry is performed with a hanging mercury drop because a mercury amalgam will be formed upon deposition of metal ions in the preconcentration step. However, the toxicity and disposal problem of mercury has motivated the development of mercury-free electrodes. Comparison between a boron-doped diamond electrode and a mercury electrode shows that diamond provides at least three times improvement in sensitivity[6]. Various methods such as microwave enhanced stripping voltammetry, rotating disk techniques, sonoelectrochemistry and microdisk arrays have been utilized in order to improve the performance of diamond electrodes in stripping voltammetry. Here, we demonstrate the immobilization of bacteria on the diamond surface and the analytical application of this bacteria-diamond coupling electrode in stripping voltammetry. *Acidithiobacillus ferrooxidans* is used in this work because of its ability to tolerate high metal concentrations and fix metal ions[7].

5.2 Experimental Section

5.2.1 Chemicals

All the chemicals used in this experiment were purchased from Sigma Aldrich unless otherwise stated and were used as received.

5.2.2 Diamond Electrode Preparation

The submicron grain size, 5-µm-thick microcrystalline diamond was grown on a silicon (100) substrate at a substrate temperature of 750 °C using hot filament chemical vapor deposition (conditions: 2 sccm CH_4, 200 H_2. 20 Torr for 7 h). Diamond samples were cleaned and chemically oxidized with hot 'Piranha' solution (30% H_2O_2 : 97% H_2SO_4 = 1 : 3) for 1 hour, followed by rinsing with ultrapure water. The samples were then rinsed with tetrahydrofuran followed by hexane. Cleaned diamond samples were hydrogen-terminated by a hydrogen plasma treatment at 800 W in a microwave plasma CVD system.

5.2.3 Bacteria Culture

Bacteria *Acidithiobacillus ferrooxidans* was maintained and routinely subcultured in a modified 9K medium of Silverman and Lundgren[8] (40 g L^{-1} $FeSO_4$, 0.5 g L^{-1} $MgSO_4.7H_2O$, 0.5 g L^{-1} K_2HPO_4, 3 g L^{-1} $(NH_4)_2SO_4$, 0.1 g L^{-1} KCl and pH 1.9 controlled by H_2SO_4). The culture was maintained in a shaking incubator at room temperature.

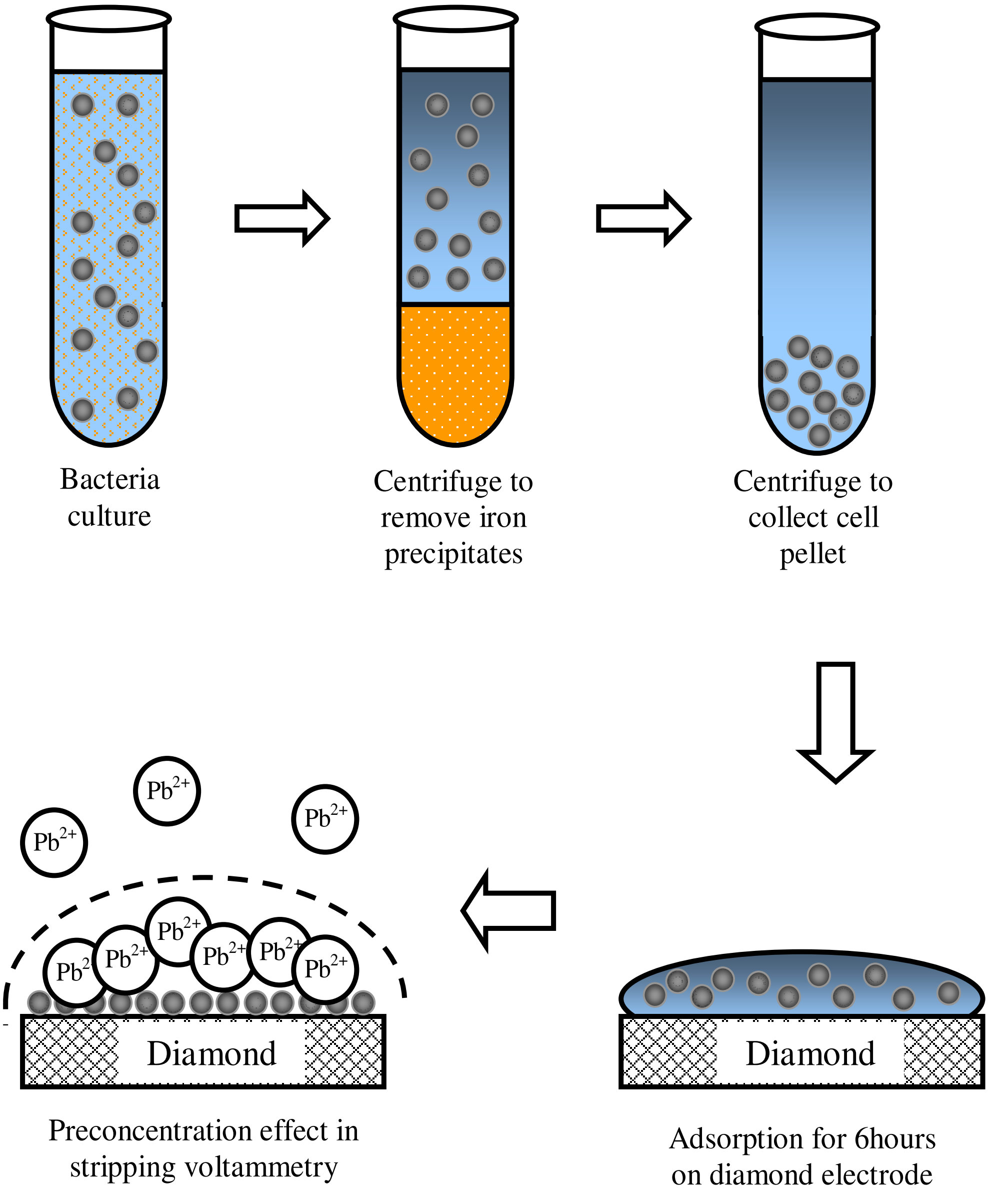

Schematic 5.1 Preparation of bacteria-modified diamond electrode.

5.2.4 Bacteria-modified Diamond Electrode

In order to eliminate the effect of iron in the electrochemical measurement, an iron-free cell suspension was prepared for the bacteria adsorption. The culture was first centrifuged at 1500g to remove the iron precipitates, and the bacteria cells in the supernatant were then harvested by further centrifugation at 12000g. Cells pellet was washed 3 times with dilute H_2SO_4 and finally suspended in the acidic sterilized water (pH 2). The adsorption of bacteria was carried out by immersing the diamond electrode into an iron-free bacteria suspension for a period of 6 hours. This process is schematically illustrated in Schematic 5.1.

5.2.5 Stripping Voltammetry

All electrochemical measurements were carried out in a single-compartment Teflon cell with a three-electrode configuration system: a diamond working electrode, Ag/AgCl reference electrode (3.0 M KCl), and a Pt-wire counter electrode. For all electrochemical experiments, a small area (0.07 cm^2) of the diamond surface was exposed to the solution through a Viton O-ring. The top contact with the diamond sample surface was made through an Au-plated probe. The bacteria-modified diamond electrode was immersed in the Pb^{2+} working solution for a period of 6mins before the stripping voltammetry was started. The cathodic stripping voltammetry was performed with the following parameters: deposition potential 1.65 V, deposition time 60 secs, scan rate 25 mV s^{-1}. The Pb^{2+} working solution was prepared in a 0.1 M HNO_3 solution. The limit of detection was determined by stepwise replacement of the Pb^{2+} working solution with pure HNO_3 solution, with the electrochemical measurement being recorded after each dilution step until the stripping peak decreases to van ishingly small intensity.

5.3 Results and Discussion

5.3.1 Adsorption of *Acidithiobacillus ferrooxidans*

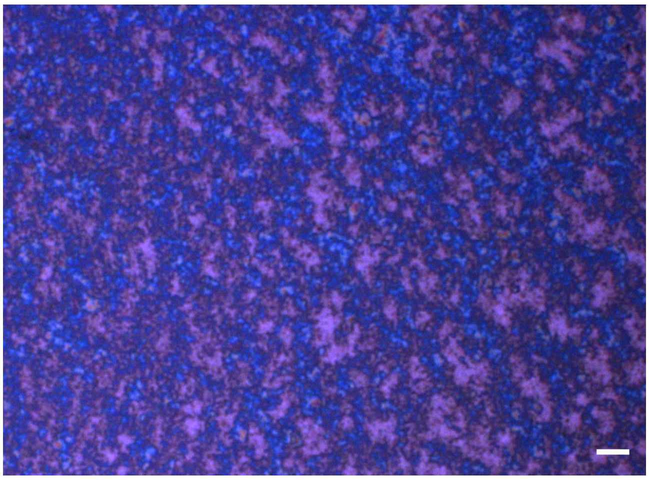

Figure 5.1 Optical micrograph of the diamond electrode after immersing in bacteria suspension for 6 hours. (Scale bar = 100 μm)

Figure 5.1 shows the optical micrograph of diamond electrode after immersing in the iron-free bacteria suspension for 6 hours. It can be seen that the micron-sized *Acidithiobacillus ferrooxidans* has developed a compact biofilm on top of the diamond electrode. According to ZoBell's model of bacterial adhesion, the immobilization process can be divided into 2 stages—an initial stage of reversible adhesion followed by a time-independent irreversible stage.[9,10]. Adhesion of bacteria onto the substrate is mainly attributed to the production of extracellular polysaccharides (EPS) which overcome the electrostatic barrier for cell adhesion. In another study by Gehrke *et. al.*, the authors discovered that the EPS is deficient in the iron-rich suspension[11]. Hence, iron-free bacteria suspension was used in this study for the adsorption process in order to induce large quantities of EPS for cell attachment.

Furthermore, the presence of iron in the suspension might introduce interference to the electrochemical measurement.

5.3.2 Linear Range and Detection Limit

Cathodic stripping voltammetry is used in this work for the Pb^{2+} ion detection. The Pb^{2+} ions are first oxidized and deposited onto the electrode surface as PbO_2. During the cathodic scan, it is reduced back to Pb^{2+} ions in solution. It can be represented by the following chemical equation:

$$2H_2O + Pb^{2+} \leftrightarrow PbO_2 + 4H^+ + 2e^-$$

Figure 5.2 shows the linear sweep voltammograms obtained from the bacteria-modified diamond electrode in a series of Pb^{2+} concentration working solutions after an initial contact period and deposition period. It can be clearly seen that the voltammetry plots exhibit a well-defined stripping peak at ~1.21 V. This stripping peak corresponds to the reduction of surface-bound lead oxides back to lead ions. A linear dependence of the stripping current as a function of Pb^{2+} concentration can be established in the range of 10 µM to 100 µM for both the bacteria-modified diamond electrode and the bare diamond electrode (Figure 5.3). At higher Pb^{2+} concentration (>200 µM), the relationship with stripping current becomes non-linear because not all the electrodeposited lead oxides can be reduced back within the stripping region[12]. It is also interesting to note that the bacteria-modified diamond electrode exhibits higher sensitivity (37.5 nA μM^{-1}) towards Pb^{2+} compared to the bare diamond electrode (22.3 nA μM^{-1}). The detection limit for bacteria-modified diamond electrode is found to be 10µM, 2 times better than the detection limit for the bare diamond electrode (20 µM). An explanation for the enhancement in detection limit and sensitivity is the ability of

Acidithiobacillus ferrooxidans to fix metal ions, resulting in an increase of metal ions around the bacteria cells. This will provide the preconcentration effect which will directly enhance the detection limit.

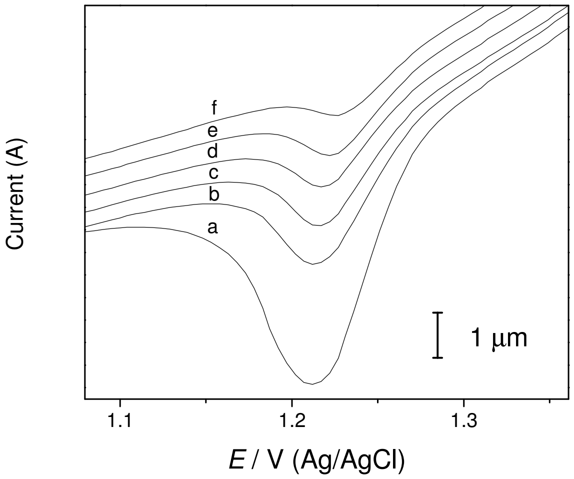

Figure 5.2. Effect of lead concentration on cathodic stripping voltammograms in 0.1 M HNO_3 containing Pb^{2+} of (a) 100 µM, (b) 50 µM, (c) 40 µM, (d) 30 µM, (e) 20 µM, (f) 10 µM.

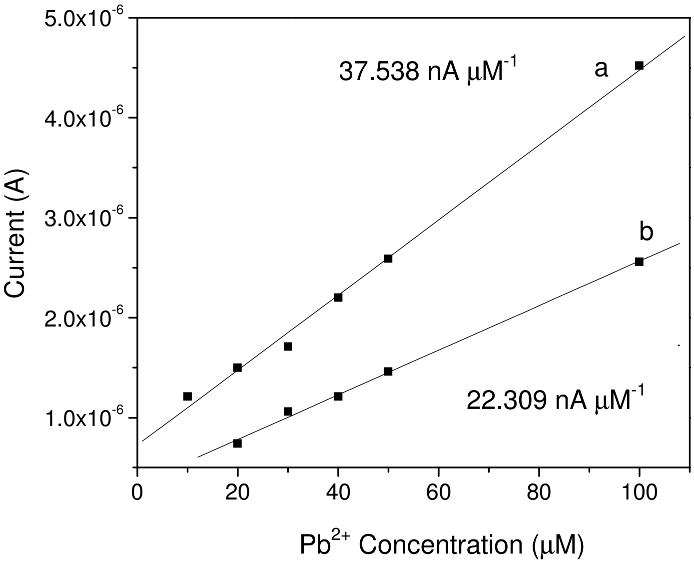

Figure 5.3 Calibration plot for stripping current vs. different lead concentrations for (a) a bacteria-modified diamond electrode and (b) a diamond electrode.

5.3.3 Interference with Copper Ions

The effect of possible interference from other metal ions towards Pb^{2+} detection was also investigated on the bacteria-modified diamond electrode. Linear sweep voltammograms in Figure 5.4 show the effect of different copper concentrations (ranging from 200 µM to 25 µM) on Pb^{2+} (constant concentration at 100 µM) stripping peaks. There are two stripping peaks which can be assigned to the reduction of lead oxides (~ 1.21 V) and copper oxides (~ -0.3 V). The linear sweep voltammograms in Figure 5.5 show the effect of copper (constant concentration at 500 µM) on different concentrations of Pb^{2+} (ranging from 80 µM to 30 µM). It should be noted that the linear relationship of Pb^{2+} stripping currents is not affected by the presence of copper ions. No suppression of the lead stripping peak is observed though the concentration of copper is found to be 15 times higher than the Pb^{2+} concentration. It is reported for glassy carbon electrodes that the presence of 10-times excess of copper ions will completely suppress the lead stripping peak[13]. The role of bacteria in eliminating intermetallic species problems remains unknown here, and one of the possible explanations for this phenomenon is the catalytic effect of copper towards proton reduction. Hydrogen evolution is expected to occur on the deposited copper particles at -0.4 V[14]. In this work, an acidic working solution was used and there will be enhancement of proton discharge during hydrogen evolution on deposited copper particles, and this may have rendered the copper particle surface less accessible for lead deposition.

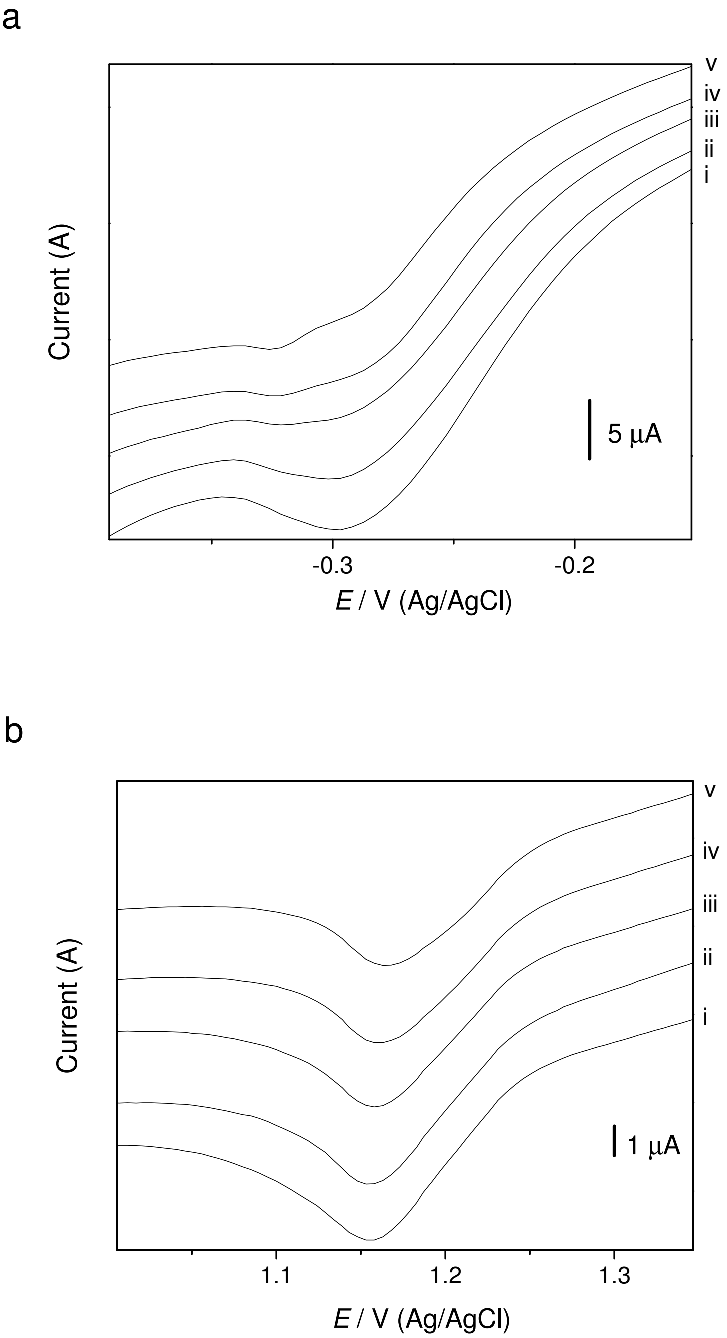

Figure 5.4 Effect of different Cu^{2+} concentrations on the (a) Cu^{2+} and (b) Pb^{2+} stripping peaks recorded in constant concentration of Pb^{2+} working solutions. Different Cu^{2+} concentrations (µM) (i) 200, (ii) 150, (iii) 100, (iv) 50, (v) 25.

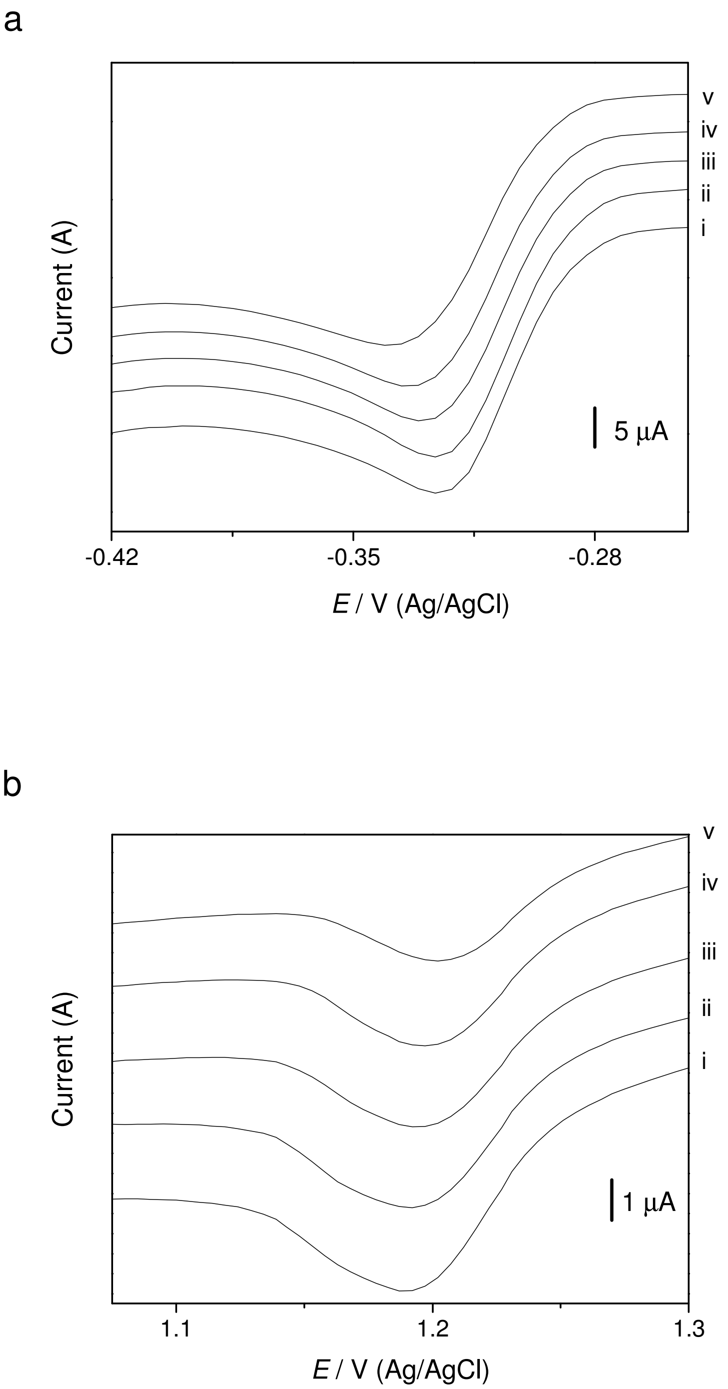

Figure 5.5 Effect of constant Cu^{2+} concentration on the (a) Cu^{2+} and (b) Pb^{2+} stripping peaks recorded in different concentrations of Pb^{2+} working solutions. Different Pb^{2+} concentrations (μM) (i) 80, (ii) 60, (iii) 50, (iv) 40, (v) 30.

5.4 Conclusions

This work demonstrates that the adsorption of bacteria cells, namely *Acidthiobacillus ferrooxidans*, onto diamond electrodes can enhance the performance of the latter in stripping voltammetry. In lead ion detection, the bacteria-modified diamond electrode exhibits a lower detection limit (10 μM) and a higher sensitivity compared to a bare diamond electrode. Under similar experimental parameters, this detection limit (10 μM) is comparable to the reported detection limit (3 μM) of a diamond electrode enhanced by ultrasonically-assisted stripping voltammetry[15]. The capacity of *Acidthiobacillus ferrooxidans* to fix heavy-metal ions on the membrane enables it to act as the preconcentration agent to increase the local concentration of heavy-metal ions around the electrode. The bacteria-modified diamond electrode is also found to be free from the interference of intermetallic species.

References

---

[1] Strojek, J. W.; Granger, M. C.; Dallas, T.; Holtz, M. W.; Swain, G. M. *Anal. Chem.* **1996**, 68, 2031.

[2] Yano, Y.; Tryk, D. A.; Hashimoto, K.; Fujishima, A. *J. Electrochem. Soc.* **1998**, 145, 1870.

[3] Show, Y.; Witek, M. A.; Sonthalia, P.; Swain, G. M. *Chem. Of Mater.* **2003**, 15, 879.

[4] Rao, T. N.; Yagi, Y.; Miwa, T.; Tryk, D. A.; Fujishima, A. *Anal. Chem.* **1999**, 71, 2506.

[5] Manivannan, A.; Tryk. D. A.; Fujishima, A. *Electrochemical and Solid-State Letters* **1999**, 1, 455.

[6] McGaw, A. E.; Swain. M. G. *Anal. Chim. Acta* **2006**, 575, 180.

[7] Boyer, A.; Magnin, J. –P.; Ozil, P. *Biotechnol. Lett.* **1998**, 20, 187.

[8] Silverman, M. P.; Lundgren, D. G. *J. Bacteriol.* **1959**, 78, 326.

[9] ZoBell, C. E. *J. Bacteriol.* **1937**, 33, 86.

[10] ZoBell, C. E. *J. Bacteriol.* **1943**, 46, 39.

[11] Gehrke, T.; Telegdi, J.; Thierry, D.; Sand, W. *Appl. Environ. Microbiol.* **Jul 1998**, 2743.

[12] Awada, M.; Strojek, J. W.; Swain, G. M. *J. Electrochem. Soc.***1995**, 142, 42.

[13] Kabanova, O. L.; Beniaminova, S. M. *J. Anal. Chem. U.S.S.R.* **1970**, 26, 94.

[14] Davis, J.; Moorcroft, M. J.; Wilkins, S. J.; Compton, R. G.; Cardosi, M. F. *Analyst*, **2000**, 125, 7.

[15] Saterlay, A. J.; Agra-Gutierrez, C.; Taylor, M. P. ; Marken, F. ; Compton, R. G. *Electroanalysis*, **1999**, 11, 1083.

Chapter 6. Electrochemical Study of Epitaxial Graphene

Two types of graphene samples were electrochemically studied, namely an as-synthesized graphene sample generated by the segregation of carbon on silicon carbide (henceforth called epitaxial graphene) and a mildly oxidized epitaxial graphene. The electrochemical response was evaluated using $Fe(CN)_6^{3-/4-}$, ferrocenecarboxylic acid, $Ru(NH_3)_6^{2+/3+}$ and $IrCl_6^{2-/3-}$ and the comparison was made based on the apparent heterogeneous electron-transfer rate constant, charge-transfer resistance and activation enthalpy. Both graphene samples demonstrated extremely low background current which is an excellent property for designing a biosensor. The introduction of higher carbon-oxygen functionalities on mildly-oxidized graphene exhibits lower electron transfer with higher activation enthalpy as compared to the as-synthesized graphene. However, mildly-oxidized graphene shows excellent properties in resisting biofouling by β-nicotinamide adenine dinucleotide (NADH) and achieves a detection limit of 10 nM. The electrochemical data presented here can serve as a benchmark for evaluating the electrochemical properties of a graphene sample.

6.1 Introduction

Graphene consists of sp^2-bonded carbon atoms arranged in a dense honeycomb crystal structure. It possesses semimetallic behavior with a small overlap between the valence and the conduction band, known as a zero-gap material[1]. The unique quantum properties of graphene such as the quantum Hall effect, massless Dirac quasiparticles[2] and ballistic transport of electrons, have attracted intense attention from both the experimental and theoretical scientific communities in recent years[3]. The high carrier mobilities[3] of 15000 cm^2/V, ballistic transport, and two-dimensional (2D) nature of graphene make it a promising candidate for various applications in microelectronic devices, such as batteries[4], field effect transistors[5], ultrasensitive sensors[6] and electromechanical resonators[7]. Though there is still a considerable amount of on-going research on the electronic properties and applications of graphene, there are few reports on the electrochemical studies of graphene.

In this work an investigation was carried out on the electrochemical properties of an epitaxial graphene film synthesized by the thermal desorption of silicon on SiC. The as-synthesized epitaxial graphene was further electrochemically oxidized in mild acidic conditions in order to increase the carbon-oxygen functionalities on the graphene surface. four redox systems, namely $Fe(CN)_6^{3-/4-}$, ferrocenecarboxylic acid, $Ru(NH_3)_6^{2+/3+}$ and $IrCl_6^{2-/3-}$ were used to assess the electrochemical behavior of two graphene samples. Finally, β-nicotinamide adenine dinucleotide (NADH) was selected as the biomolecule with which to evaluate the biosensing properties of the graphene samples. The determination of NADH is vital because NADH and its oxidized form (NAD^+) are the coenzymes for a large number of dehydrogenase enzymes and components of biomarker systems[8,9,10]. However, the oxidation of

NADH usually encounters a low sensitivity problem due to its high overpotential (~0.8 V) and biofouling of the electrode surface[11,12,13].

6.2 Experimental Section

6.2.1 Chemicals

All the chemicals used in this experiment were purchased from Sigma Aldrich unless otherwise stated and were used as received. The NADH solution was prepared and used freshly. All the solutions in this work were prepared in deionized water.

6.2.2 Graphene Preparation

Epitaxial graphene was fabricated on the silicon-terminated (0001) face of high purity 6H-SiC by thermal desorption of silicon at high temperature[14].

6.2.3 Electrode Preparation and Pretreatment

Electrical connection to the graphene was made by contacting copper wire to the graphene surface and mounting with silver paste. The electrical connection, backside and edge of the graphene sample were insulated with nail varnish. The as-synthesized graphene underwent mild electrochemical oxidation at 2 V in 0.5 M H_2SO_4 for 60 seconds. Hereafter, we denote the as-synthesized graphene as the "graphene sample" and the graphene sample after mild oxidation as "oxidized graphene".

6.2.4 Electrochemical Measurement

All electrochemical experiments in this work were accomplished by an Autolab/PGSTAT30, Eco Chemie B.V. with a platinum wire and a saturated Ag/AgCl electrode as the counter and reference electrodes, respectively. Cyclic voltammetry was performed at room temperature with different scan rates (step potential of 5 mV) and the measurement was repeated 3 times to obtain reproducible signals. In every case, the last cycle was recorded. The cyclic voltammetry measurements at different temperatures were performed with a cold or hot plate. The electrochemical cell was encapsulated in styrofoam and the temperature inside the cell was controlled within ±0.2°C during the measurement. The amperometric measurement of NADH was done by collecting the current response with time at a constant potential of 0.75 V. A magnetic stirrer (100 rpm) was used to provide convective transport during the amperometric measurement. Electrochemical impedance spectroscopy (EIS) was carried out with an Autolab Frequency Response Analyzer (FRA). The impedance data were collected from 500 kHz to 0.01 Hz at an a.c. amplitude of 10 mV and performed at open-circuit potential (OCP). 1 M KCl was used as the working electrolyte for redox species throughout the electrochemical measurements and 0.1 M phosphate buffer solution was used as the working electrolyte for NADH measurements.

6.3 Results & Discussions

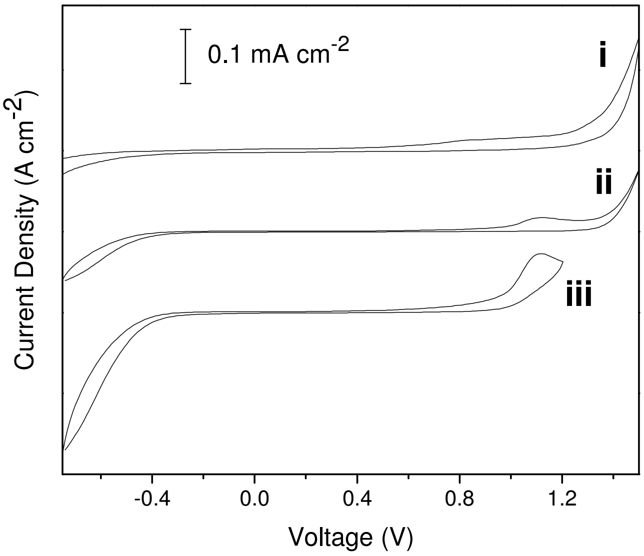

Figure 6.1 Electrochemical window of (i) boron-doped diamond, (ii) graphene, (iii) oxidized graphene in 1M KCl at 0.1mV s^{-1}.

Figure 6.1 shows the representative background cyclic voltammograms for graphene and oxidized graphene electrodes in pure electrolyte 1 M KCl at 100 mV s^{-1}. For the sake of comparison, the reported currents have been normalized to the exposed surface area. The background cyclic voltammetry is very useful to evaluate the graphene electrode surface as the electrochemical response is highly sensitive to the physicochemical properties of the electrode. The graphene electrode possesses a working potential window of 1.7 V with a low and featureless background current in the region between -0.35 V and 1.35 V. There is no evidence for any surface redox processes occuring on the graphene surface between -0.35 V to 0.9 V, indicating that graphene is ideally polarizable in this potential region. On the other hand, oxidized graphene is observed to a have narrower working potential window, i.e. 1.35 V, although it also exhibits a low background current. Both graphene samples show an anodic peak on the forward sweep at 1.1 V which can be attributed to the oxidation of sp^2 carbon and electrochemically-active carbon-oxygen functionalities. It can be seen that oxidized graphene show as higher anodic current at 1.1 V because the oxidation of the graphene surface has increased the carbon-oxygen functionalities. Both graphene samples also show a similarity in the onset potential for hydrogen evolution but the oxidized graphene exhibits a lower onset potential for chlorine evolution. As a comparison, a wide electrochemical window material, i.e. a boron-doped diamond electrode, has been inserted into the graph.

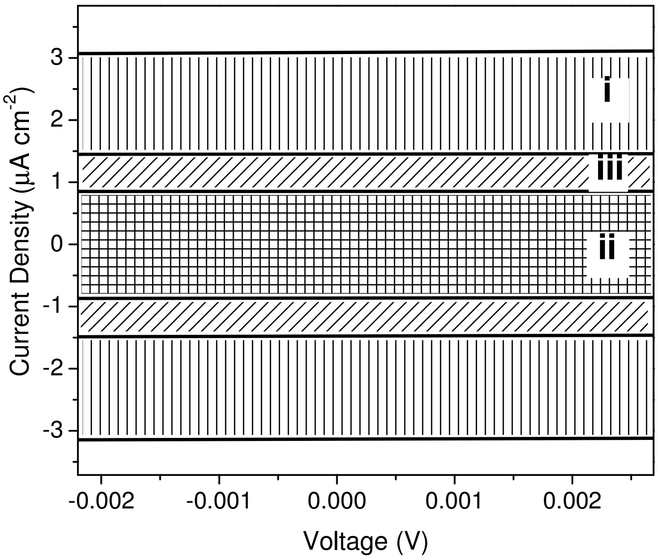

Figure 6.2 Capacitive background current of (i) boron-doped diamond, (ii) graphene, (iii) oxidized graphene in 1M KCl at 0.1 mV s^{-1}.

In order to have a clear view of the capacitive background current, three voltammograms (boron-doped diamond, graphene and oxidized graphene) are displayed together in Figure 6.2. Interestingly, both graphene samples exhibit a low background current compared to boron-doped diamond. At 0 V, the capacitive background current for graphene (0.85 µA cm^{-2}) is about 3.5 times lower than that of the boron-doped diamond (3.08 µA cm^{-2}), while the capacitive background current for oxidized graphene (1.46 µA cm^{-2}) is about 2 times lower. The increment of capacitive background current for oxidized graphene as compared to graphene can be attributed to the increase of carbon-oxygen functionalities on the surface which will lead to charging of the surface. Both graphene samples seem to have stable surface microstructures because no change can be observed after multiple cycle scans.

Figure 6.3 displays the cyclic voltammograms for $Fe(CN)_6^{3-/4-}$, ferrocenecarboxylic acid, $Ru(NH_3)_6^{2+/3+}$ and $IrCl_6^{2-/3-}$, respectively, on both graphene samples. These redox systems were chosen to evaluate the sensitivity of each redox system to the surface microstructure and electronic properties of the two graphene samples[15]. The apparent electron-transfer rate constants $k°_{app}$ (calculated with Nicholson's method[16]) for the redox systems are summarized in Table 6.1. Figure 6.4 shows that the peak current for each redox system varies linearly with the square-root of the scan rate (r^2>0.995), for both graphene and oxidized graphene samples. This indicates that the reactions for these 4 redox systems are controlled by the semi-infinite linear diffusion of the redox species to the graphene and oxidized graphene surface.

$Fe(CN)_6^{3-/4-}$ is chosen as a redox probe because the electrode reaction kinetics for this redox couple are strongly influenced by the fraction of exposed edge plane on sp^2-bonded carbon electrodes and the surface cleanliness[17]. Figure 6.3(a) shows that the $Fe(CN)_6^{3-/4-}$ redox reaction is near-Nernstian (ΔE_p = 73 mV) on a graphene surface. After undergoing mild oxidation on the graphene surface, the current response for oxidized graphene is reduced, accompanied by an increase in ΔE_p. Furthermore, graphene shows 2 times higher $k°_{app}$ for the $Fe(CN)_6^{3-/4-}$ redox system as compared to the oxidized graphene. It is found that the higher surface termination of oxygen on oxidized graphene lowers the electron-transfer rate of $Fe(CN)_6^{3-/4-}$. However, the redox reaction is still reversible on oxidized graphene. This can be explained by the fact that the oxidized graphene only undergoes very mild electrochemical oxidation; hence, a complete coverage of oxygen functionalities on the surface is not achieved.

Redox species	**$k°_{app}$ (cm s^{-1})**	
	Graphene	**Graphene(O)**
$Fe(CN)_6^{3-/4-}$	5.02×10^{-3}	2.51×10^{-3}
Ferrocenecarboxylic acid	2.10×10^{-3}	1.34×10^{-3}
$Ru(NH_3)_6^{2+/3+}$	3.27×10^{-3}	2.91×10^{-3}
$IrCl_6^{2-/3-}$	8.38×10^{-3}	8.38×10^{-3}

Table 6.1 Comparison of apparent electron-transfer rate constant, $k°_{app}$ for graphene and oxidized graphene in different redox systems.

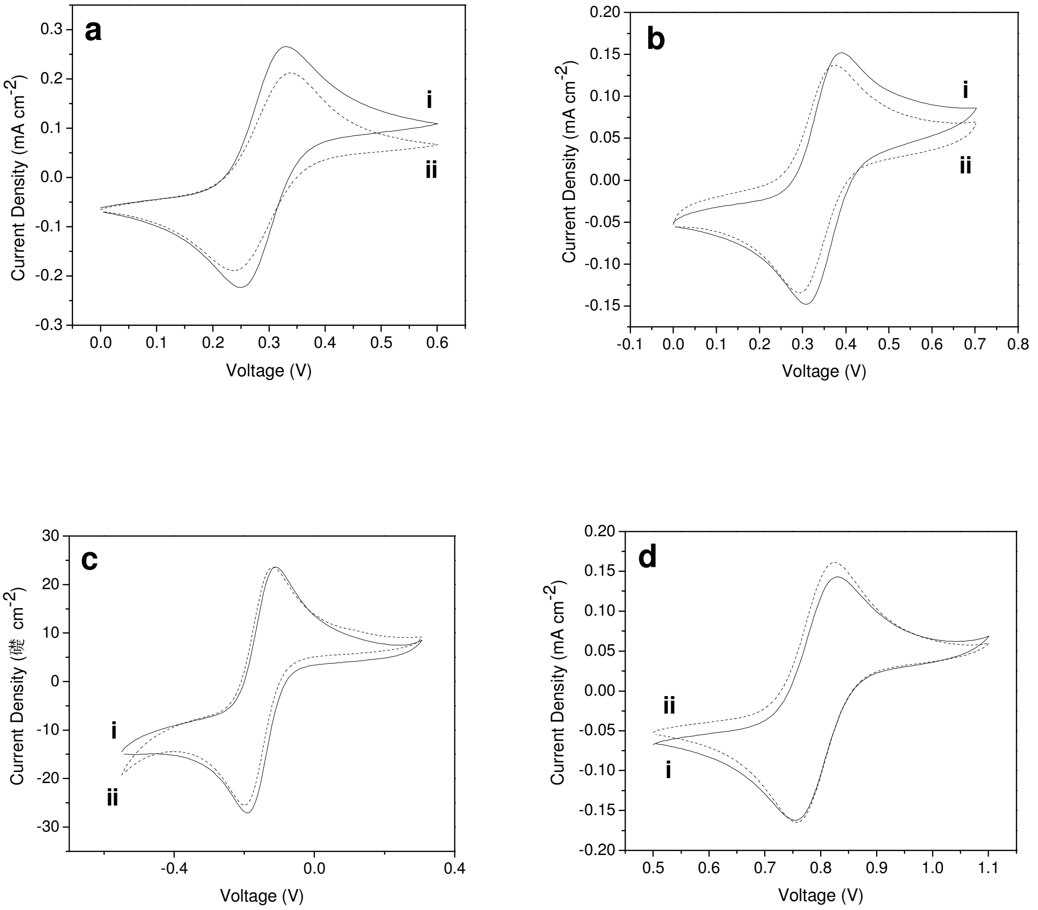

Figure 6.3 Cyclic voltammograms of (i) graphene, (ii) oxidized graphene in 1 mM (a) $Fe(CN)_4^{3-/4-}$, (b)ferrocenecarboxylic acid, (c) $Ru(NH_3)_6^{2+/3+}$, (d) $IrCl_6^{2-/3-}$ redox systems at 100 mV s^{-1}.

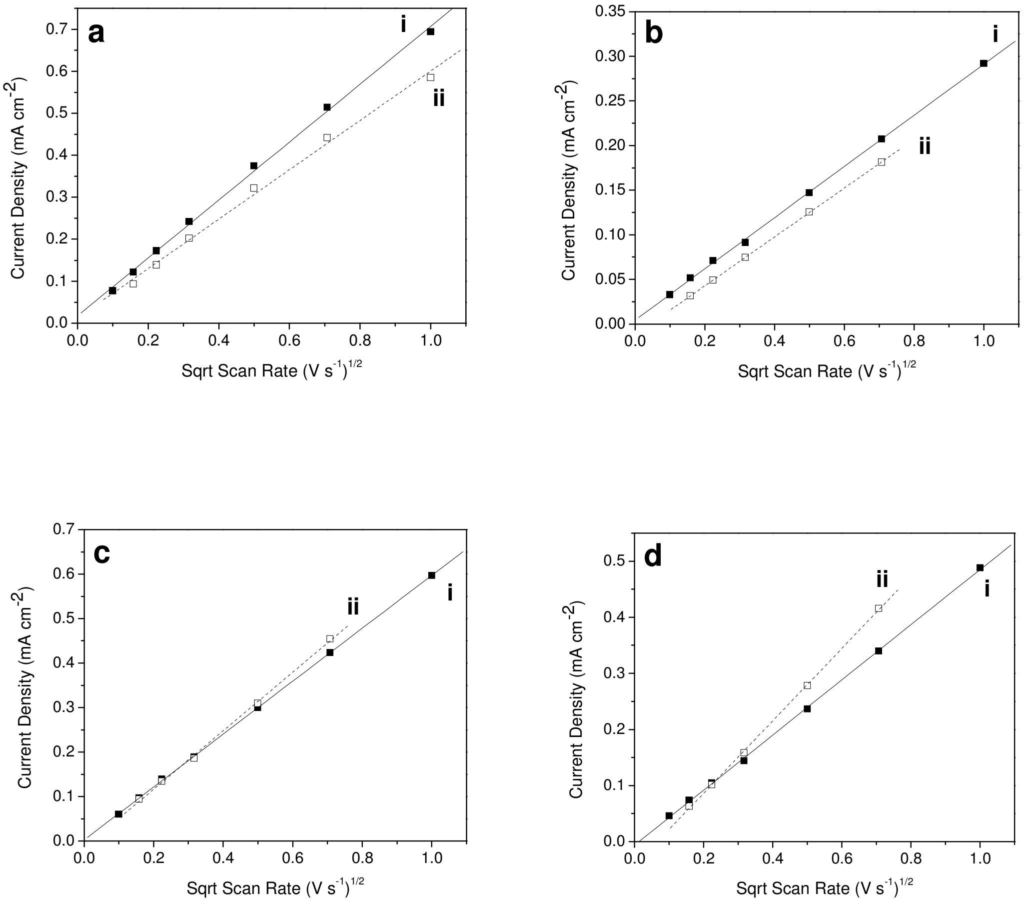

Figure 6.4 Peak current vs. square root scan rate for (i) graphene and (ii)oxidized graphene in 1 mM (a) $Fe(CN)_4^{3-/4-}$, (b)ferrocenecarboxylic acid, (c) $Ru(NH_3)_6^{2+/3+}$, (d) $IrCl_6^{2-/3-}$ redox systems.

Ferrocenecarboxylic acid is chosen as a redox probe because of its sensitivity to the surface functionalities. Figure 6.3(b) shows the cyclic voltammograms of graphene and oxidized graphene in ferrocenecarboxylic acid. The electrochemical behaviors of graphene and oxidized graphene in ferrocenecarboxylic acid are found to be very similar to those of the $Fe(CN)_6^{3-/4-}$ redox system. Both samples exhibit a near-Nernstian redox reaction; current response for graphene is higher than for oxidized graphene; graphene has 2 times higher $k°_{app}$ for the ferrocenecarboxylic acid redox system compared to that for oxidized graphene. The lower value of $k°_{app}$ for oxidized graphene can be explained by the partial coverage of oxygen functional groups on the oxidized graphene surface.

$Ru(NH_3)_6^{2+/3+}$ is chosen as a redox probe as it only involves simple electron transfer on the electrode and the reaction rate is largely determined by the electronic properties of the electrode. The electrode kinetics for $Ru(NH_3)_6^{2+/3+}$ are relatively insensitive to the surface microstructure, surface functionalities or adsorbed layers. Figure 6.4(c) shows that $Ru(NH_3)_6^{2+/3+}$ exhibits a near-Nernstian redox reaction on both graphene and oxidized graphene with the same current response, same ΔE_p and same $k°_{app}$. This is an indication that the mild electrochemical oxidation does not change the electronic properties of graphene and it merely increases the oxygen functionalities on the surface.

A strong analogy can be found for the electrode reaction for both graphene samples on $Ru(NH_3)_6^{2+/3+}$ and $IrCl_6^{2-/3-}$ redox systems. $IrCl_6^{2-/3-}$ also involves simple electron transfer and it is insensitive to the surface microstructure and surface functionalities. The most important factor affecting the rate of reaction is the electronic properties of the electrode. Similar to the electron transfer on $Ru(NH_3)_6^{2+/3+}$, both graphene samples showed same current response, ΔE_p and $k°_{app}$ on $IrCl_6^{2-/3-}$.

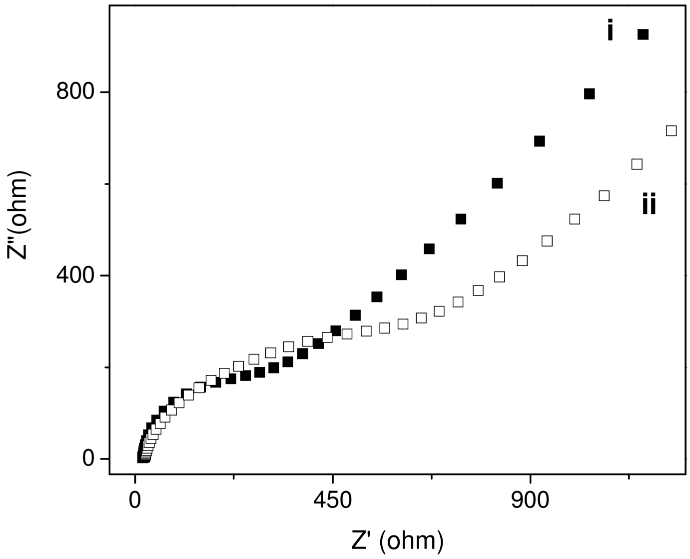

Figure 6.5 Nyquist plot of (i) graphene, (ii) oxidized graphene in 1 mM $Fe(CN)_6^{3-/4-}$ electrolyte.

Figure 6.5 shows that the Nyquist plots of both graphene and oxidized graphene samples show similar behavior at open circuit potential (OCP): a small semicircle followed by a 45° straight line. This implies that the charge-transfer resistance (R_{CT}) across both graphene samples is small and limited only by Warburg diffusion. The impedance data of both graphene samples are fitted into simple Randles equivalent-circuit models as depicted in Figure 6.6 and the R_{CT} values are extracted from the model. Under similar experimental conditions, the R_{CT} for oxidized graphene is almost 2 orders of magnitude higher than the $\mathrm{R_{CT}}$ for graphene. This implies that the mild oxidation process on a graphene surface will impart a charge-transfer barrier for a $Fe(CN)_6^{3-/4-}$ electrolyte, consistent with the higher $k°_{app}$ finding on oxidized graphene.

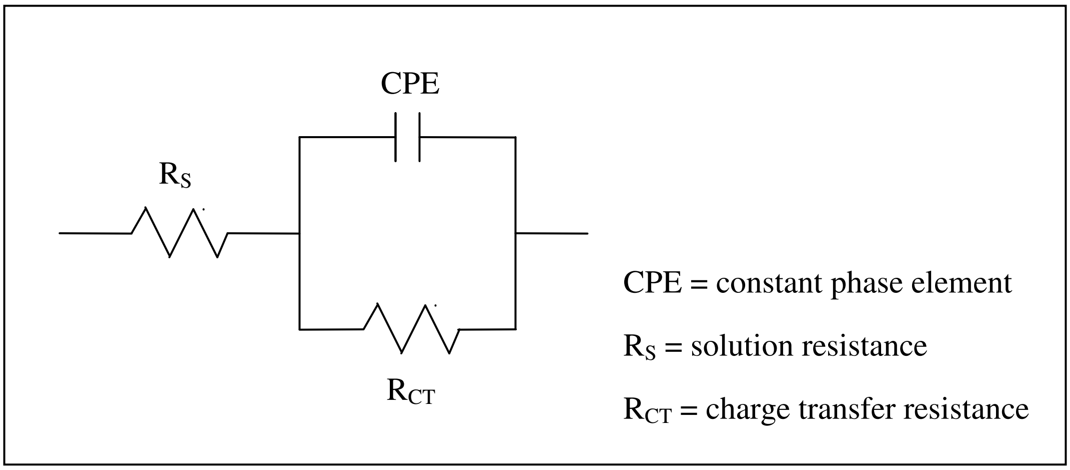

Figure 6.6 Randles equivalent-circuit model for graphene and oxidized graphene electrodes in 1 mM $Fe(CN)_6^{3-/4-}$ electrolyte.

In order to elucidate the thermodynamic processes on the graphene samples, the role of temperature is taken into consideration, ranging from 20°C to 60°C in $Fe(CN)_6^{3-/4-}$ electrolyte. The thermodynamic data are summarized in Figure 6.7. Both the graphene samples exhibited similar behavior, $k°_{app}$ increased with respect to the temperature. For the same temperature, the graphene sample shows a higher $k°_{app}$ value compared to the oxidized graphene sample. The Arrhenius plot in Figure 6.7 provides the relevant information for the extraction of thermodynamic data. Again, the plot shows that the current density for the graphene sample is always higher compared to that of the oxidized graphene sample for the same temperature. According to Equation 6.1, the apparent electrochemical activation enthalpy ($\Delta H^{\circ\neq}$) can be extracted from the slope of the Arrhenius plot. $\Delta H°\neq$ value of 0.729 kcal mol^{-1}, in the case of the graphene sample and of 1.172 kcal mol^{-1} for the oxidized one, have been found, respectively. The results show that a larger current density was recorded where the activation enthalpy is lower. It can be inferred that the mild oxidation process on a graphene surface increases the activation enthalpy of the sample, supporting the results of a lower k°_{app} and a higher R_{CT} on the oxidized graphene sample.

$$-2.303 \times \log i_O = K' + [\Delta H^{\circ\neq}/(RT)] - (\Delta S^{\circ\neq}/R) \qquad \text{(Equation 6.1)}^{18}$$

i_O = current K' = constant $\Delta H^{\circ\neq}$ = electrochemical activation enthalpy

R = gas constant T = temperature $\Delta S^{\circ\neq}$ = electrochemical entropy

In order to develop graphene as a biosensor for the continuous monitoring of biomolecules, electrochemical stability of the electrode towards biomolecules is very crucial. In this work, NADH is selected as the biomolecule for electrochemical stability testing. However, direct oxidation of NADH at bare electrodes occurs at high overpotential (~0.8 V) and is usually accompanied by the problem of electrode fouling from its oxidation product (NAD^+). The electrochemical oxidation of NADH on bare glassy carbon electrodes was anodically shifted and deactivated rapidly due to the irreversible adsorption of NAD^{+}[19]. In order to reduce both the fouling problem and the overpotential problem, an electrochemical pretreatment on a glassy carbon electrode was applied[20,21]. However, such pretreatment was overwhelmed by the increase in detection limit due to the increase in background current. A carbon-nanotube-modified electrode was found to possess anti-fouling properties and a lower detection potential towards NADH oxidation[22,23]. However, it was difficult to obtain a low detection limit using this carbon-nanotube-modified electrode because of its high background current due to its large surface roughness.

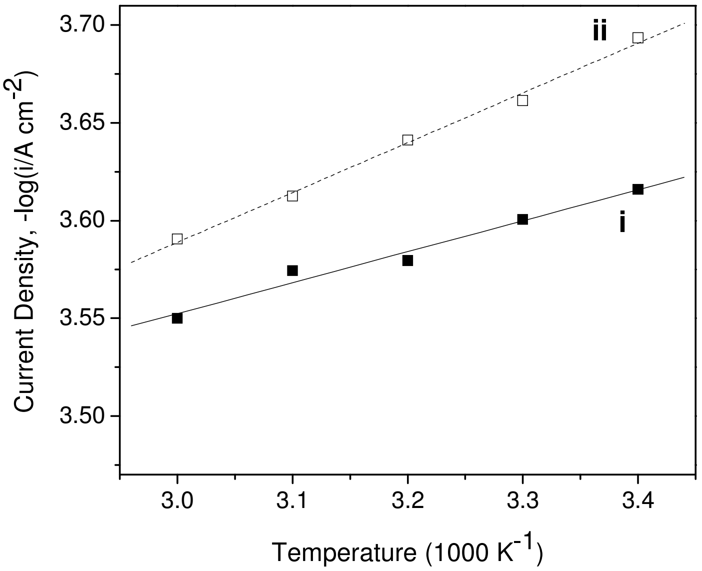

Figure 6.7 Arrhenius plot for $Fe(CN)_6^{3-/4-}$ electrolyte at (i) graphene and (ii) oxidized graphene electrodes.

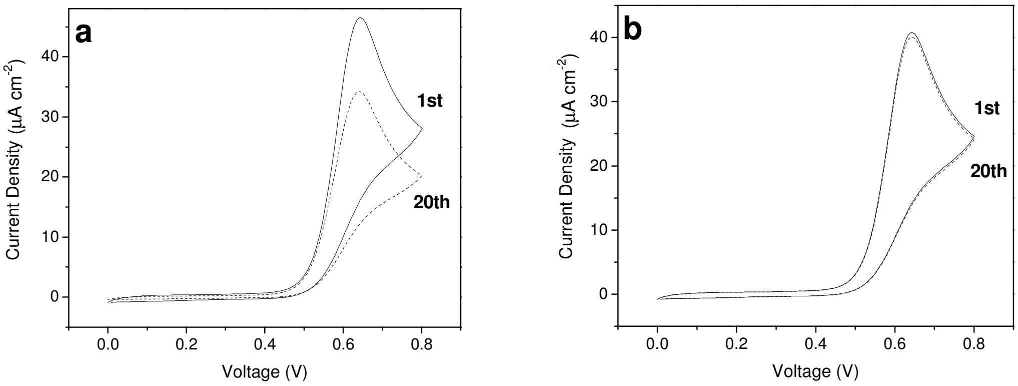

Figure 6.8 Cyclic voltammograms for 5 μM NADH in 0.1 M PBS at (a) graphene and (b) oxidized graphene electrodes at 100 mV s^{-1}. The solid and dotted lines represent the 1st and 20th scans, respectively.

Figure 6.8 shows the cyclic voltammograms for 5 μM NADH on graphene and oxidized graphene electrodes. The solid lines in the cyclic voltammograms represent the 1st cycle while the dotted lines represent the 20th cycle. On the 1st scan, both graphene and oxidized graphene electrodes exhibit a clear NADH oxidation peak at 0.64 V. However, differences between the two electrodes appear after continuous scans for 20 cycles. We can observe a drastic drop in the NADH oxidation-peak current for the graphene electrode while the oxidation-peak current remains stable on the oxidized graphene electrode. The oxidation-peak currents for 20 repetitive cycle scans are summarized in Figure 6.9. It can be seen that the oxidation-peak currents for the graphene electrode decreases monotonically after each cycle, which is an indication of the surface fouling caused by the adsorption of NAD^+. In contrast, stable oxidation-peak currents for the oxidized graphene electrode can be obtained under the same measurement conditions and the peak currents remain unchanged after 20 scan cycles. Hence, we conclude that the mild electrochemical oxidation of a graphene surface increases its resistance towards NAD^+ surface fouling.

The detection limit of NADH on oxidized graphene was determined using amperometry A constant voltage of 0.75 V was applied for complete oxidation of NADH as the oxidation of NADH at graphene occurs at 0.64 V. Figure 6.10 summarizes the calibration curve for NADH oxidation on an oxidized graphene electrode. The current response increases with increasing NADH concentration and the linearity range is from 10 nM to 5 μM with sensitivity of 7.56 nA cm^{-2} nM^{-1}. The detection limit of oxidized graphene for NADH is found to be 10 nM (S/N=3) as shown in Figure 6.11. This result indicates that the oxidized graphene is a useful electrode material for analytical detection of NADH, making it an attractive platform for an enzyme-catalyzed biosensor which involves NADH as a cofactor. The biofouling resistance may be due to the presence of oxygen groups which prevent π-π stacking of the biomolecules.

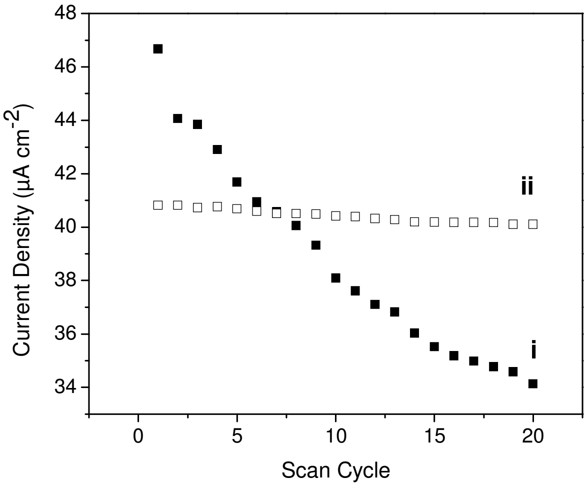

Figure 6.9. Summary of NADH oxidation-peak currents for (i) graphene and (ii) oxidized graphene electrodes obtained from 20 repetitive cyclic voltammetry scans.

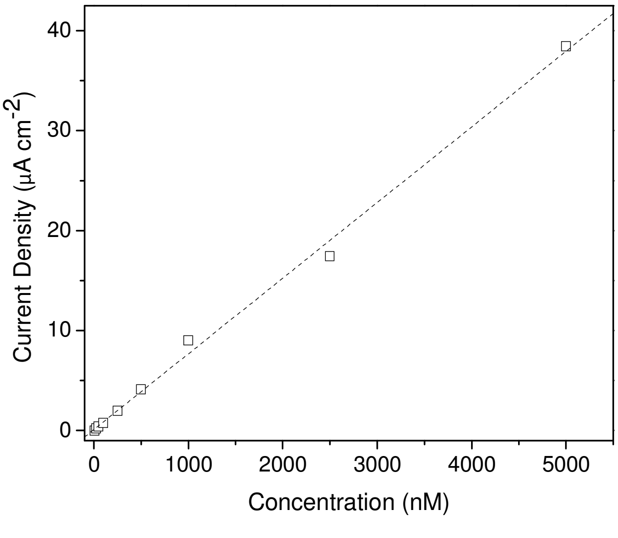

Figure 6.10. Calibration curve of NADH at an oxidized graphene electrode. The concentration range is from 10 nM to 5 μM. The oxidation currents were derived from the amperometric experiment with a constant voltage of 0.75 V.

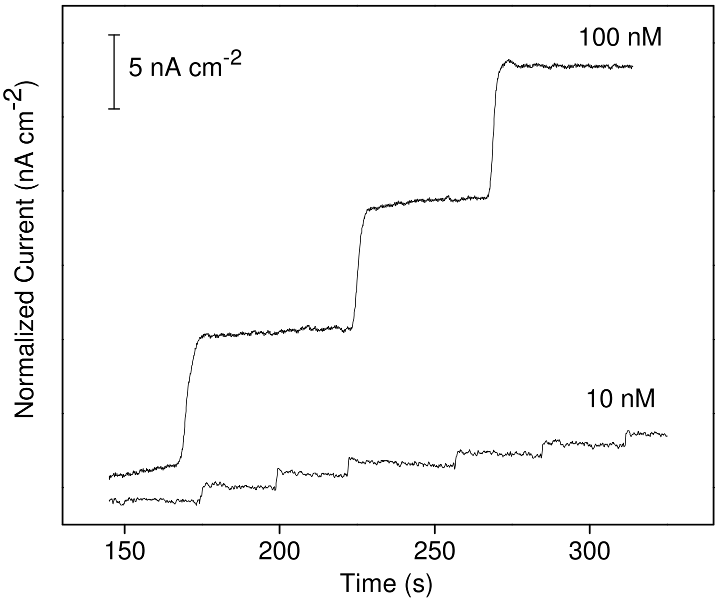

Figure 6.11 Amperometry plots of oxidized graphene electrode towards addition of 100 nM NADH and 10 nM NADH.

6.4 Conclusions

The electrochemical properties of graphene materials were investigated before and after mild electrochemical oxidation. Graphene materials show extremely low background currents which are slightly increased after the oxidation process. Nevertheless, this low background current behavior of graphene materials renders them superb materials for analytical measurement. The electrochemical activities of graphene were tested with 4 different redox systems. It is found that the electron transfer of $Fe(CN)_6^{3-/4-}$ and ferrocenecarboxylic acid redox systems on graphene material is reduced after the graphene oxidation, as these two redox species are sensitive to the presence of surface oxides. However, the electrochemical oxidation on graphene material does not alter its electrochemical activities for $Ru(NH_3)_6^{2+/3+}$ and $IrCl_6^{2-/3}$ redox systems. For the $Fe(CN)_6^{3-/4-}$ redox system, graphene is found to possess a higher charge-transfer resistance and a higher activation enthalpy after mild electrochemical oxidation. Although the oxidation process on graphene decreases its electrochemical activities towards certain redox systems, it shows excellent properties in resisting biofouling problems created by the oxidation of NADH, and a low detection limit (10 nM) for NADH can be achieved.

References

---

[1] Lemme, M. C.; Echtermeyer, T. J.; Baus, M.; Kurz, H. *IEEE Electron Device Letters* **2007**, *28*, 282.

[2] Novoselv, K. S.; Geim, A. K.; Morozov, S. V.; Jiang, D.; Katsnelson, M. I.; Grigorieva, I. V.; Dubonos, S. V.; Firsov, A. A. *Nature* **2005**, *438*, 197.

[3] Novoselv, K. S.; Geim, A. K.; Morozov, S. V.; Jiang, D.; Zhang, Y.; Dubonos, S. V.; Grigorieva, I. V.; Firsov, A. A. *Science* **2004**, *306*, 666.

[4] Cassagneau, T.; Fendler, J. H. *Adv. Mater.* **1998**, *10*, 877.

[5] Gilje, S.; Han, S.; Wang, M.; Wang, K. L.; Kaner, R. B. *Nano Lett.* **2007**, *7*, 3394.

[6] Schedin, F.; Geim. A. K.; Morozov, S. V.; Hill, E. W.; Blake, P.; Katsnelson, M. I.; Novoselov, K. S. *Nat. Mater.* **2007**, *6,* 652.

[7] Bunch, J. S.; van der Zande, A. M.; Verbridge, S. S.; Frank, I. W.; Tanenbaum, D. M.; Parpia, J. M.; Craighead, H. G.; McEuen, P. L. *Science*, **2007**, *315*, 490.

[8] Pariente, F.; Lorenzo, E.; Tobalina, F.; Abruna. H. D. *Anal. Chem.* **1995**, *67*, 3936.

[9] Wu, Q.; Maskus, M.; Pariente, F.; Tobalina, F.; Fernández, V. M.; Lorenzo, E.; Abruna, H. D. *Anal. Chem.*, **1996**, *68*, 3688.

[10] Pariente, F.; Tobalina, F.; Moreno, G.; Hernandez, L.; Lorenzo, E.; Abruna, H. D. *Anal. Chem.,* **1997**, *69*, 4065.

[11] Moiroux, J.; Elving, J. *Anal. Chem.*, **1978**, *50*, 1056.

[12] Jacgfeldt, H. *J. Electroanal. Chem.* **1980**, *110*, 295.

[13] Blaedel, W.; Jenkins, R. *Anal. Chem.* **1975**, *47*, 1337.

[14] Zhou, S.Y.; Gweon, G. –H.; Fedorov, A. V.; First, P. N.; de Heer, W. A.; Lee, D. –H.; Guinea, F.; Castro Neto, A. H.; Lanzara, A. *Nat. Mater.* **2007,** 6, 770.

[15] Wang, S.; Swope. V. M.; Butler, J. E.; Feygelson, T.; Swain, G. M. *Diam. Rel. Mater.* **2009**, 18, 669.

[16] Nicholson, R. S. *Anal. Chem.* **1965**, 37, 1351.

[17] Chen, P.; McCreery, R. L. *Anal. Chem.*, **1996**, *68*, 3958.

[18] Ferro, S.; Battisti, A. D. *Electrochimica Acta* **2002**, 47, 1641.

[19] Moiroux, J.; Elving, P. J. *Anal. Chem.* **1978**, *8*, 1056.

[20] Engstrom, R. C.; Strasser, V. A. *Anal. Chem.* **1984**, *56*, 136.

[21] Hayes, M. A.; Kuhr, W. G. *Anal. Chem.* **1999**, *71*, 1720.

---

[22] Musameh, M.; Wang, J.; Merkoci, A.; Lin, Y. *Electrochem. Commun.* **2002**, *4*, 743.

[23] Valentini, F.; Amine. A.; Orlanducci. S.; Terranova, M. L. ; Palleschi, G. *Anal. Chem.* **2003**, *75*, 5413.

Chapter 7. Conclusions

The cell adhesion characteristics on diamond surfaces with different topographies and surface chemistries have been quantitatively analyzed by using biochemical assays and atomic force microscopy. It was found that UV irradiation of a diamond surface in air is effective to oxidize the diamond surface, and such oxygenated surfaces are hydrophilic and provide a better platform for initial cell adhesion. It was also found that the initial cell adhesion force correlates to the subsequent cell growth. A photochemical process was used to couple carboxylic groups to the diamond surface, providing the equivalent biocompatible properties to an oxidized diamond surface. It was also verified that surface topography will affect cell adhesion and cell growth, as ultrananocrystalline diamond is proven to have a higher initial cell adhesion force and a higher cell growth rate. Surface carboxylic acid groups on diamond are amenable to further functionalization with protein to support neuronal cell growth. They also can be modified to form a surface concentration gradient and subsequently used to support cell gradient formation. A cell gradient on a diamond surface opens up the possibility of diamond to be used in combinatorial chemistry studies.

A whole-cell biosensor was successfully constructed on a diamond platform by using two different biological entities, namely *Chlorella vulgaris* (green algae) and *Acidithiobacillus ferrooxidans*. For the green algae biosensor, *p*-nitrophenol was used as the substrate for alkaline phosphatase activity, the product of which is notorious for biofouling. The application of diamond as a signal transduction platform for algae cells provided long-term stability for the biosensor, and a low detection limit (0.1 ppb) was achieved for cadmium and zinc ions. On the other hand, bacteria-modified diamond provided enhancement in the stripping voltammetry for lead ions. The capacity of *Acidthiobacillus ferrooxidans* to fix heavy-metal ions on its membrane enabled it to act as the preconcentration agent to increase the local concentration of heavy-metal ions around the diamond electrode. Thus, a lower detection limit (10 μM) and a higher sensitivity were achieved on bacteria-modified diamond electrodes.

The electrochemical and kinetic properties of graphene materials were investigated before and after mild electrochemical oxidation. Both graphene materials showed extremely low background currents which were slightly increased after the oxidation process. For certain redox systems, the surface oxide on mild-oxidized graphene shows a higher charge-transfer resistance and a higher activation enthalpy compared to as-synthesized graphene. Nevertheless, the surface oxide provides resistance to NADH biofouling which led to a low detection limit (10 nM) for NADH on mild-oxidized graphene electrodes. This opens up the possibility of graphene to be used as an electrochemical biosensor.